

**Simultaneous Position and Orientation Estimation for Visible Light
Systems with Multiple LEDs and Multiple PDs**

Shengqiang Shen

Doctoral dissertation submitted to obtain the academic degree of
Doctor of Electrical Engineering

Supervisor

Prof. Heidi Steendam, PhD

Department of Telecommunications and Information Processing
Faculty of Engineering and Architecture, Ghent University

May 2021



**Simultaneous Position and Orientation Estimation for Visible Light
Systems with Multiple LEDs and Multiple PDs**

Shengqiang Shen

Doctoral dissertation submitted to obtain the academic degree of
Doctor of Electrical Engineering

Supervisor

Prof. Heidi Steendam, PhD

Department of Telecommunications and Information Processing
Faculty of Engineering and Architecture, Ghent University

May 2021



ISBN 978-94-6355-489-3

NUR 959

Wettelijk depot: D/2021/10.500/37

Members of the Examination Board

Chair

Prof. Filip De Turck, PhD, Ghent University

Other members entitled to vote

Prof. Marc Moeneclaey, PhD, Ghent University

Prof. David Plets, PhD, Ghent University

Prof. Nobby Stevens, PhD, KU Leuven

Prof. Henk Wymeersch, PhD, Chalmers University of Technology, Sweden

Supervisor

Prof. Heidi Steendam, PhD, Ghent University

Acknowledgements

There are many who helped me along the way on this journey. I want to take a moment to thank them.

I am deeply indebted to my supervisor Prof. Dr. Ir. Heidi Steendam. To me, she is the most gracious and strict supervisor. Her insightful feedback and strict pushed me to sharpen my thinking and drove my work to a higher level. At the same time, she is always patient with me even when I keep making the same mistakes of which I'm already ashamed. I feel so lucky to have her as my supervisor.

I would like to express my deepest appreciation to my jury members of my PhD Examination Board for their careful review of my dissertation and their valuable comments.

I would like to thank my colleagues at the TELIN department at Ghent University for creating such a good and pleasant working atmosphere. Special thanks to Davy Moreels for his time and effort in designing and 3D printing the experimental modules and to Jose Miguel Menéndez Sánchez for supporting the experimental apparatus.

I would also like to extend my gratitude to my friends: Lingchen Gu, Zhixin Guo, Shaoguang Huang, Xian Li, Meizhu Li, Taoyong Li, Chi Liu, Chengjin Lyu, Xuening Qin, Yifan Xiao, Zhikang Xiang, Jize Xue, and Ting Zhao, for putting up with my "hearing problem" (I'm still awaiting for your fundraising) and lame jokes. Special thanks to Shaoguang Huang for sharing his secret cooking recipe with me, to Taoyong Li for being the leader of the canteen squad, to Meizhu Li for sharing the location of the chestnut tree, and to Jingyu Luo for providing a lot of strange knowledge. I am also grateful to my former roommates and friends: Junyi Li, Chengxi Liao, Jie Song, Xiepeng Sun, Wenhao Yao, Xudong Zhao, I will always miss the fun times I had playing cards with you.

Last but not least, I would like to thank my parents for always being there for me and encouraging me to follow my heart.

*Ghent, May, 2021.
Shengqiang Shen*

Contents

Acknowledgements	i
List of Figures	vii
List of Tables	xi
List of Abbreviations	xiii
List of Notations	xv
List of Symbols	xvii
Summary	xix
Samenvatting	xxiii
1 Introduction	1
1.1 State-of-the-Art	1
1.2 Problem Statement	5
1.3 Contributions and Publications	7
1.4 Outline	8
2 Fundamentals of Visible Light System	11
2.1 Physical Aspects	11
2.1.1 Properties of LEDs	11
2.1.2 Properties of PDs	14
2.1.3 Channel Model	15
2.1.4 Noise Analysis	17
2.2 (De)Modulation Scheme	18
2.3 System Overview	19
2.3.1 Transmitter	20
2.3.2 Receiver	20
2.3.3 Coordinate Systems	20
2.4 Receiver Structures with Multiple PDs	21
2.4.1 Angular Diversity Receiver	21
2.4.2 Aperture-Combined Receiver	23
2.5 Conclusion	26

3	Estimation Theory and Basics of $SO(3)/SE(3)$	27
3.1	Estimation Problems	27
3.1.1	ML Estimation	28
3.1.2	MAP Estimation	29
3.1.3	HMM Estimation	29
3.1.4	LS Estimation	30
3.1.5	Measures of Error	30
3.2	Basics of $SO(3)/SE(3)$	32
3.2.1	The Groups of $SO(3)$ and $SE(3)$	32
3.2.2	The Gradient of Functions on $SO(3)/SE(3)$	33
3.2.3	Distribution on $SO(3)$	36
3.2.4	The Intrinsic CRB on $SO(3)$	37
3.3	Conclusion	38
4	Simultaneous Position and Orientation Estimation for the Angular Diversity Receiver	41
4.1	Problem Statement	41
4.2	Estimation Algorithms	42
4.2.1	Gauss-Newton Method on Manifolds	43
4.2.2	Interior Point Method on Manifolds	44
4.2.3	Convergence and Complexity Analysis	46
4.2.4	Initial Coarse Estimation	48
4.3	The Theoretical Lower Bound	51
4.4	Numerical Results	51
4.4.1	Performance of the Estimators	53
4.4.2	Asymptotic Tightness	57
4.4.3	Impact of Location of the Receiver	59
4.4.4	Configuration of the Receiver	59
4.5	Conclusion	65
5	Hybrid Position and Orientation Estimation in the Presence of Prior Information on Orientation	67
5.1	Problem Statement	68
5.1.1	Model of Orientation Uncertainty	68
5.1.2	Approximation to the Orientation Uncertainty Model	70
5.2	RSS-Based Hybrid ML/MAP Estimation	71
5.3	The Theoretical Lower Bound	74
5.4	Numerical results	76
5.4.1	Performance of the hybrid ML/MAP Estimator	76
5.4.2	Asymptotic Tightness	82
5.4.3	Impact of Location of the Receiver	85
5.5	Conclusion	85

6 Simultaneous Position and Orientation Estimation for the Aperture-Combined Quadrant Photodiode	89
6.1 A New Look at the Channel Model	90
6.1.1 Approximating the PDF of the Observation	94
6.2 Calibration System and SPO Estimation	96
6.2.1 Calibration Procedure	96
6.2.2 The Theoretical Lower Bound	99
6.2.3 SPO Estimation	101
6.3 Numerical Assessment and Experiment	102
6.3.1 Numerical Assessment of Calibration Algorithm	104
6.3.2 Numerical Assessment of SPO Estimator	107
6.3.3 Experiment Results	110
6.4 Conclusion	113
7 Conclusions	117
7.1 Conclusions	117
7.2 Future Research	118
Appendices	121
A Evaluation of the NLOS Channel	121
B Internal Reflection of the Aperture-Combined Receiver	127
C Theoretical Lower Bound for the MML Estimator	131
Bibliography	133

List of Figures

1.1	Electromagnetic spectrum.	3
2.1	Optical-power-current-voltage characteristic curve.	12
2.2	LED packaging.	12
2.3	Normalized Lambertian pattern.	13
2.4	Normalized radiation pattern of LXML-PWC2, along with the luminous efficacy of human eyes.	14
2.5	The responsivity $R(\lambda)$ of FDS010, along with the normalized radiation pattern of LXML-PWC2.	16
2.6	LOS and NLOS links between a PD and a LED.	16
2.7	System model of N_L LEDs and N_P PDs.	19
2.8	Block diagram of a single link for the visible light system.	20
2.9	Angular diversity receiver with $N_{P,s} = 6$	22
2.10	Coordinates and orientations of PDs in the receiver frame.	22
2.11	Structure of quadrant photodiode.	24
2.12	Geometry of the light spot of a light beam.	25
2.13	Structure of AQPDP.	25
3.1	Optimization on $SO(3)$ manifold.	34
4.1	Angular diversity receiver with $N_{P,s} = 4$	49
4.2	Plane-based pose estimation problem. P : the virtual image plane, P' : the plane of the ceiling.	50
4.3	Simulation setup. The three orthonormal vectors in three different colors at each sample on the path represent the frame of the receiver (shown with $\theta_R = 0$ rad), where the red, green and blue vector represent the x -axis, y -axis and z -axis, respectively. The pink arrows represent the LEDs (only a fraction of them are shown) on the ceiling. θ_r indicates the traveled angle along the dotted ellipse in the XY plane.	52
4.4	RMSE versus iteration for SNR= 25 dB and SNR= 35 dB. (a) Position estimation errors, (b) Orientation estimation errors.	54
4.5	RMSE of the position estimate and the theoretical bound for $\theta_R = -\pi/3$ rad with (a) SNR = 25 dB and (b) SNR = 35 dB.	55
4.6	RMSE of the orientation estimate and the theoretical bound for $\theta_R = -\pi/3$ rad with (a) SNR = 25 dB and (b) SNR = 35 dB.	56

4.7	RMSE versus θ_R for SNR= 25 dB and SNR= 35 dB. (a) Position estimation errors, (b) Orientation estimation errors.	58
4.8	RMSEs of estimating position and orientation parameters as a function of SNR when $N_L = 24$ for Case 1: $\theta_R = 0$ rad and Case 2: $\theta_R = -\pi/3$ rad.(a) position estimation errors, bottom row, (b) orientation estimation errors.	60
4.9	RMSEs of estimating position and orientation parameters and as a function of the number of LEDs when SNR = 35 dB for Case 1: $\theta_R = 0$ rad and Case 2: $\theta_R = -\pi/3$ rad. (a) position estimation errors, (b) orientation estimation errors.	61
4.10	Averaged SPOB on the position vector (a) as a function of the position in the XY plane fixed at 1.5 m in z -axis, (b) as a function of the height.	62
4.11	Averaged SPOB on the orientation matrix (a) as a function of the position in the XY plane fixed at 1.5 m in z -axis, (b) as a function of the height.	63
4.12	The averaged indicator as a function of θ_P . (a) Indicator for different SNRs (b) Indicator for different N_L s.	64
5.1	Distribution of $\mathbf{n}_b = \mathbf{R}_\epsilon \mathbf{n}_a$	69
5.2	Bhattacharyya distance between received power and approximated ones.	71
5.3	RMSE of the position as a function of the traveled angle θ_r along the elliptical path for $\sigma_\epsilon^2 = 1 \times 10^{-2}$ rad ²	77
5.4	RMSE of the orientation as a function of the traveled angle θ_r along the elliptical path for $\sigma_\epsilon^2 = 1 \times 10^{-2}$ rad ²	78
5.5	RMSE versus $1/\sigma_\epsilon^2$ for SNR = 35 dB.	81
5.6	RMSE of position and orientation estimates versus SNR for $N_L = 24$	83
5.7	RMSE of position and orientation estimates versus N_L for SNR = 35 dB.	84
5.8	The root of theoretical lower bound as a function of the position of the receiver.	86
5.9	The root of theoretical lower bound as a function of the position of the receiver.	87
6.1	The channel link model of AQPD. The position of the LED and centers of the aperture and the light spot comply with the perspective projection model, while the shape and size of the light spot is determined by the aperture.	90
6.2	System frame for calibration.	96
6.3	Histogram of $[\mathbf{t}]_1$ as a function of ξ	102
6.4	Evaluation of approximated mean and covariance. (a) Approximated values as a function of ξ . (b) RMSE as a function of ξ	103

6.5	Histograms of the empirical observation along with fitted Gaussian curves.	104
6.6	RMSE of the estimator (a) as a function of $\bar{\xi}$, where $N_L = 25$, $N_T = 4$, and $\theta_\beta = \pi/9$ rad, (b) as a function of θ_β , where SNR = 45 dB, $N_L = 25$, and $N_T = 4$	105
6.7	RMSE of the estimator (a) as a function of N_L , where SNR = 45 dB, $N_T = 4$, and $\theta_\beta = \pi/9$ rad, (b) as a function of N_T , SNR = 45 dB, $N_L = 25$, and $\theta_\beta = \pi/9$ rad.	108
6.8	RMSE for position and orientation estimates as a function of θ_r , compared with the mean received SNR $\bar{\xi}$	109
6.9	RMSE for position and orientation estimates as a function of the mean received SNR $\bar{\xi}$	109
6.10	Experiment setup.	110
6.11	Block diagram of the experiment setup.	110
6.12	The square with four LEDs and the trajectory for the square.	112
6.13	$x - y$ view of the estimated position for 1.0 m in z -direction and $\pi/6$ rad tilt angle.	115
A.1	Scenario for ray-tracing simulation.	123
A.2	Impulse response corresponding to different components.	124
A.3	Magnitude of the channel frequency response.	125
B.1	Illustration of AQPD created in TracePro.	128
B.2	Illustration of the simulated reflection inside the house.	128
B.3	Irradiance response of reflection inside the house.	130

List of Tables

1.1	Comparison of indoor positioning technologies [1,2]	2
3.1	Matrix Lie group properties for $SO(3)$ and $SE(3)$	33
6.1	Experiment specification.	111
6.2	Performance of different algorithms.	114
A.1	Simulation configuration for ray-tracing	122
B.1	Simulation configuration for TracePro	127

List of Abbreviations

AOA	Angle of Arrival
AQPD	Aperture-Combined Quadrant Photodiode
AR	Augmented Reality
BCRB	Bayesian Cramér-Rao Bound
CRB	Cramér-Rao Bound
DLT	Direct Linear Transformation
FDM	Frequency Division Multiplexing
FIM	Fisher Information Matrix
FOV	Field of View
GNM	Gauss Newton Method
GPS	Global Positioning System
HIM	Hybrid Information Matrix
HMM	Hybrid Maximum Likelihood/Maximum <i>a Posterior</i>
HCRB	Hybrid Cramér-Rao Bound
IM/DD	Intensity Modulation-Direct Detection
IMU	Inertial Measurement Unit
IPM	Interior Point Method
KLD	Kullback-Leibler Divergence
KKT	Karush-Kuhn-Tucker
LBS	Location Based Services
LOS	Line of Sight
LS	Least Squares
MAP	Maximum <i>a Posterior</i>
MCRB	Misspecified Cramér-Rao Bound
MEMS	Micro Electro Mechanical System
ML	Maximum Likelihood

MLMP	Multiple LEDs and Multiple PDs
MML	Misspecified Maximum Likelihood
MSE	Mean Squared Error
NLOS	Non Line of Sight
NLS	Nonlinear Least Squares
PD	Photodiode
PDF	Probability Density Function
PO	Position and Orientation
PSD	Power Spectral Density
QPD	Quadrant Photodiode
RF	Radio Frequency
RE	Receiving Element
RFID	Radio Frequency Identification
RSS	Received Signal Strength
RMSE	Root Mean Square Error
SPO	Simultaneous Position and Orientation
SNR	Signal to Noise Ratio
$SO(3)$	Special Orthogonal Group
$SE(3)$	Special Euclidean Group
SVD	Singular Value Decomposition
TIA	Transimpedance Amplifier
TDOA	Time Difference of Arrival
UWB	Ultrawide Band
VLC	Visible light communication
VLP	Visible light positioning
VR	Virtual Reality
V2I	Vehicle to Infrastructure
V2V	Vehicle to Vehicle

List of Notations

$p(x y)$	Notational shorthand for $p_X Y(X = x Y = y)$
$E_{x z}\{f(x, y, z)\}$	Expectation of $f(x, y, z)$ w.r.t. x , conditioned on z , i.e., $\int p(x z)f(x, y, z)dx$
$D(p(\mathbf{y} \Theta) q(\mathbf{y} \hat{\Theta}))$	The Kullback-Leibler divergence (KLD) between the PDFs $p(\mathbf{y} \Theta)$ and $q(\mathbf{y} \hat{\Theta})$
\hat{x}	An estimate of x
\mathbf{x}	A vector \mathbf{x}
$[x]_i$	The i^{th} element of the vector \mathbf{x}
\mathbf{X}	A matrix/set \mathbf{X}
\mathbf{X}^T	The transpose of \mathbf{X}
$[\mathbf{X}]_{i,j}$	Element at row i , column j of \mathbf{X}
$[\mathbf{X}]^i$	The i^{th} column of matrix \mathbf{X}
$\det(\mathbf{X})$	The determinant of matrix \mathbf{X}
$\text{tr}(\mathbf{X})$	The trace of matrix \mathbf{X}
$\ \mathbf{x}\ $	Norm of \mathbf{x} : $\ \mathbf{x}\ = \sqrt{\sum_k [\mathbf{x}]_k^2}$
$\mathbf{x} \sim \mathcal{N}(\boldsymbol{\mu}, \boldsymbol{\Sigma})$	\mathbf{x} is a real random vector drawn from a multivariate Gaussian distribution with mean $\boldsymbol{\mu}$ and covariance matrix $\boldsymbol{\Sigma}$
$\ \mathbf{x}\ _{\boldsymbol{\Sigma}}^2$	The squared Mahalanobis distance with respect to covariance $\boldsymbol{\Sigma}$: $\ \mathbf{x}\ _{\boldsymbol{\Sigma}}^2 = \mathbf{x}^T \boldsymbol{\Sigma}^{-1} \mathbf{x}$
$\mathbf{1}_{N \times M}$	An $N \times M$ matrix of ones
$\mathbf{0}_{N \times M}$	An $N \times M$ matrix of zeros
\mathbf{I}_N	An $N \times N$ identity matrix
\mathbf{e}_i	A unit basis vector with its i^{th} element being 1
$\arg \max_{\Theta} f(\Theta)$	The value of Θ that maximizes $f(\Theta)$
$(\cdot)^\dagger$	The Moore-Penrose pseudoinverse operator
\cdot^\wedge	The operator that converts a 3×1 vector into the Lie algebra $\mathfrak{so}(3)$:

$$\begin{bmatrix} a_1 \\ a_2 \\ a_3 \end{bmatrix}^\wedge = \begin{bmatrix} 0 & -a_3 & a_2 \\ a_3 & 0 & -a_1 \\ -a_2 & a_1 & 0 \end{bmatrix}$$

\cdot^\vee The inverse operator of \cdot^\wedge

\cdot^\wedge The operator that converts a 6×1 vector into the Lie algebra $\mathfrak{se}(3)$ of $SE(3)$:

$$\left([\mathbf{a}^T, \mathbf{b}^T]^T \right)^\wedge = \begin{bmatrix} \mathbf{b}^\wedge & \mathbf{a} \\ \mathbf{0}^T & 0 \end{bmatrix} \in \mathbb{R}^{4 \times 4}, \quad \mathbf{a}, \mathbf{b} \in \mathbb{R}^{3 \times 1}$$

\cdot^γ The inverse operator of \cdot^\wedge

\cdot^\odot The operator that converts a 4×1 vector into a 2×3 matrix:

$$\left([a_1, a_2, a_3, a_4]^T \right)^\odot = \begin{bmatrix} a_3 & 0 & a_1 \\ 0 & a_3 & a_2 \end{bmatrix}$$

\cdot^\ominus The operator that converts a 4×1 vector into a 4×6 matrix:

$$\left([\boldsymbol{\xi}^T, \eta]^T \right)^\ominus = \begin{bmatrix} \eta \mathbf{I}_3 & -\boldsymbol{\xi}^\wedge \\ \mathbf{0}^T & \mathbf{0}^T \end{bmatrix}$$

List of Symbols

A_e	Effective collection area of a PD
A_R	Active area of a bare PD
$\Delta\lambda_n$	Bandwidth of an optical filter
B	Electrical bandwidth
γ	Lambertian order
$G_C(\theta)$	Concentrator gain
h	Channel gain, the ratio between the PD's incident optical power and LED's output optical power
I_a	Noise density of an amplifier
\mathcal{L}	Log-likelihood function
\mathbf{n}	The normal of the receiver, represented in the system frame
\mathbf{n}_L	The direction in which a LED is radiating, represented in the system frame
\mathbf{n}_P	The direction in which a PD is pointing, represented in the system frame
$\mathbf{n}_{P,r}$	The direction in which a PD is pointing, represented in the receiver frame
N_0	One-sided power spectral density (PSD)
ϕ	The radiation angle at the LED
ϕ_{FOV}	Field of view of a LED
$\Phi_{\frac{1}{2}}$	The half-power angle
p_n	Average background spectral irradiance
P_t	Optical transmit power of a LED
P_n	Received ambient optical power
q	The electronic charge
\mathbf{r}	The position of the receiver, represented in the system frame
\mathbf{R}	The orientation of the receiver, expressed in a rotation matrix
\mathbf{r}_P	The position of a PD, represented in the system frame
$\mathbf{r}_{P,r}$	The position of a PD, represented in the receiver frame
\mathbf{R}_P	The orientation of a PD
\mathbf{r}_L	The position of a LED, represented in the system frame
$R_o(\phi)$	The LED's radiation pattern at ϕ
R_p	Responsivity of a PD
θ	The incidence angle at the PD

θ_{FOV}	Field-of-view angle of a PD
$T_F(\theta)$	Optical filter gain
\mathbf{T}	The position and orientation of the receiver, expressed in an element of $SE(3)$
v	The distance between a LED and a PD
\mathbf{v}	The vector between a LED and a PD
\mathbf{y}	Observation vector

Summary

With the development of technology and upgrading of services, there is a growing demand for indoor location-based service (LBS). The indoor positioning plays a key role in LBS. Traditional RF-based indoor positioning technologies have several problems, such as low accuracy, insufficient range, and high cost, etc. Therefore, alternative technologies are being considered. As the modulation frequency of white LEDs can reach several MHz, white LEDs can be used for wireless communication and positioning. And with high-efficiency and long-lasting white LEDs gradually becoming the main source of lighting, it makes the low cost, low power consumption, and long lifetime communication and positioning possible. Visible light communication (VLC)-based positioning or visible light positioning (VLP) reuses readily available lighting infrastructure and has the advantages of high accuracy, low cost, and high indoor ubiquity, making it one of the most promising solutions for indoor positioning.

VLP has been considered in many works. As, compared to an image sensor (such as CCD cameras), photodiodes (PD)s consume less energy and can detect signals that are modulated at higher frequencies, the receiver consisting of a single PD or a PD array is gaining interest. Especially the PD array, consisting of multiple PDs, has the ability to increase the reliability, resulting in an improvement of the performance. Currently, there are two types of multiple PDs structure for the receiver, i.e., the PD array with different PD tilt angles – angular diversity receiver – and the PD array combined with apertures – aperture-combined receiver.

Since the visible light channel is largely sensitive to both the distance and angle with respect to the transmitter, a high-precision position estimate can only be achieved if the receiver's orientation is provided. If the orientation is not known, this should be taken into account when designing the estimation algorithm. However, research on the orientation of the receiver is limited. Many works assume the orientation is perfectly known in advance, i.e., an external device is used to determine the orientation of the receiver, which, however, is a strong assumption in reality. On the one hand, the external orientation estimation device is not always available for the receiver. For such a case, the estimator has to simultaneously estimate the position and orientation (PO) from the observed light signal only. On the other hand, even though the receiver is equipped with an external orientation estimation device, the drawback of using these devices is their low accuracy, i.e. they suffer from severe biases and drift problems, especially when the receiver, which is carried by a user or attached to a carrier, experiences some random movement. Consequently, even

if the receiver determines its orientation with an external orientation estimation device, the estimated orientation is subject to noise and orientation errors, meaning the instantaneous orientation is not perfectly known [3, 4]. Hence, the external device can only provide a probability distribution of the orientation to the position estimator, which can be used as prior information for the position estimation.

This thesis focuses on the simultaneous position and orientation estimation (SPO) estimation for visible light systems, particularly those with multiple LEDs and multiple PDs (MLMP). We focus on three specific topics: simultaneous position and orientation estimation for the angular diversity receiver (in the absence of prior information on orientation), hybrid position and orientation estimation for the angular diversity receiver in the presence of prior information on the orientation, and simultaneous position and orientation estimation for the aperture-combined quadrant photodiode (AQPD) (in the absence of prior information on orientation).

In the first topic, we investigate the SPO problem using received signal strength (RSS), for angular diversity receivers without an external orientation estimation device. We design two SPO algorithms using the principle of optimization on manifolds, which alleviates the constraints from the rotation matrix. In addition, we propose an initialization algorithm, based on the direct linear transformation (DLT) principle, to obtain an initial estimate in closed-form for the iterative algorithms. To evaluate the performance of the proposed RSS-based SPO algorithms, we derive the Cramér-Rao bound (CRB). In particular, the CRB on the orientation error corresponds to the intrinsic CRB or the CRB on manifolds, which measures the error in the estimated rotation matrix in a physically meaningful way. Computer simulations show an asymptotic tightness between the performance of the proposed algorithms and the theoretical lower bound, demonstrating the effectiveness of the proposed solutions.

In the second topic, we design an RSS-based hybrid position and orientation estimation algorithm using the hybrid maximum likelihood (ML)/maximum *a posteriori* (MAP) (HMM) principle for angular diversity receivers with an available external orientation estimation device, to take into account the presence of prior information on the orientation. The proposed HMM estimator is compared with the three estimators, i.e., the designed SPO estimator, the existing misspecified maximum likelihood (MML) estimator and the first-order-approximation-based positioning algorithm, subject to the orientation uncertainty. Further, in order to analytically assess the performance of the proposed estimator, the hybrid Cramér-Rao bound (HCRB) for HMM is derived. Computer simulations show an asymptotic tightness between the performance of the estimator and its associated theoretical lower bound.

In the last topic, we propose a calibration and a SPO estimation algorithm for the AQPD (without an external orientation estimation device). To this end, we first model the RSS of the AQPD as a function of the receiver's PO and misalignment using the prospective projection model. Then, we show that

the commonly applied strategy of differencing and normalization to the RSS, claimed by most works to be able to improve the robustness against RSS variation, results in a complex probability density function (PDF), which makes an effective and efficient estimation hard to achieve. Therefore, an approximated PDF in a simple closed-form is derived, based on which the calibration and the SPO estimation algorithms using the least squares (LS) estimation are proposed. The proposed calibration does not require any information about the PO of the receiver and is robust to the received power variation, which is, therefore, easy to employ and is able to relax the calibration setup. The corresponding CRB on the estimated misalignment is also derived, which can be used as an indicator to show how large the signal-to-noise ratio (SNR) or the number of LEDs should be for a desired accuracy. Both the Monte Carlo simulation and the real experiment confirm the effectiveness of the proposed calibration and the SPO estimation algorithms.

Samenvatting

Door de evolutie van de beschikbare technologie is er een sterke groei van indoor locatiegebaseerde diensten (LBS). De mogelijkheid tot positiebepaling voor binnenhuis is belangrijk voor de ontwikkeling van LBS. Traditionele RF-gebaseerde indoor positioneringstechnologieën ondervinden allerlei soorten problemen, zoals lage nauwkeurigheid, onvoldoende bereik en hoge kosten. Daarom wordt er gekeken naar alternatieve technologieën. Aangezien witte LED's kunnen gemoduleerd worden tot verschillende MHz, kunnen witte LED's worden gebruikt voor draadloze communicatie en plaatsbepaling. Aangezien witte LED's met hun hoge efficiëntie en lange levensduur geleidelijk de belangrijkste verlichtingsbron worden, is het mogelijk om communicatie en plaatsbepaling aan te bieden met lage kosten, laag stroomverbruik en lange levensduur. Plaatsbepaling op basis van zichtbaar-licht-communicatie (VLC) of zichtbaar-licht-positionering (VLP) maakt gebruik van de beschikbare verlichtingsinfrastructuur en heeft als voordelen zijn van hoge nauwkeurigheid, de lage kostprijs en de hoge alomtegenwoordigheid binnenshuis, waardoor het één van de meestbelovende oplossingen voor binnenplaatsbepaling is.

VLP werd reeds onderzocht in verschillende werken. Aangezien fotodiodes (PD) minder energie verbruiken dan beeldsensoren (zoals CCD cameras) en signalen kunnen detecteren die met hogere frequenties gemoduleerd zijn, wint de ontvanger bestaande uit een enkele PD of een PD-array aan belangstelling. Vooral de PD-array, bestaande uit meerdere PD's, heeft de mogelijkheid om de betrouwbaarheid te verhogen, wat resulteert in een verbetering van de prestaties. Momenteel zijn er twee soorten ontvangerstructuren met meerdere PDs, namelijk een PD-array met verschillende PD-kantelhoeken (angular diversity receiver) en een PD-array gecombineerd met aperturen (aperture-combined receiver).

Aangezien het kanaal voor zichtbaar licht in hoge mate gevoelig is voor zowel de afstand als de hoek ten opzichte van de zender, kan een zeer nauwkeurige positiebepaling alleen worden verkregen als de oriëntatie van de ontvanger bekend is. Indien de oriëntatie niet bekend is, moet hiermee rekening worden gehouden bij het ontwerp van het schattingsalgoritme. Het onderzoek naar de oriëntatie van de ontvanger is echter beperkt. In veel werken wordt ervan uitgegaan dat de oriëntatie van tevoren perfect gekend is, d.w.z. dat een extern apparaat wordt gebruikt om de oriëntatie van de ontvanger te bepalen, wat in werkelijkheid echter een onrealistische veronderstelling is. Enerzijds is een externe oriënteringsschatter niet altijd beschikbaar in de ontvanger. In een dergelijk geval moet de schatter gelijktijdig de positie en de oriëntatie

(PO) schatten op basis van het waargenomen lichtsignaal alleen. Anderzijds, ook al is de ontvanger uitgerust met een externe oriëntatieschatter, is er het probleem van de geringe nauwkeurigheid van deze toestellen. De externe oriënteringsschatters hebben te kampen met ernstige afwijkingen en driftproblemen, vooral wanneer de ontvanger, die door een gebruiker wordt gedragen of op een drager is bevestigd, een willekeurige beweging ondergaat. Bijgevolg is, zelfs wanneer de ontvanger zijn oriëntatie bepaalt met een extern toestel voor oriëntatieschatting, de geschatte oriëntatie onderhevig aan ruis en oriëntatiefouten, wat betekent dat de ogenblikkelijke oriëntatie niet perfect gekend is [3, 4]. Het externe toestel kan dus alleen een waarschijnlijkheidsverdeling van de oriëntatie aan de positie-schatter verstrekken, wat dan als priori informatie voor de positie-schatting kan worden gebruikt.

Deze dissertatie richt zich op de PO-schatting voor systemen met zichtbaar licht, in het bijzonder systemen met meerdere LEDs en meerdere fotodiodes (PDs) (MLMP). Wij concentreren ons op drie specifieke onderwerpen: gelijktijdige positie- en oriëntatieschatting voor de angulaire diversiteitsontvanger (in afwezigheid van voorafgaande informatie over de oriëntatie), hybride positie- en oriëntatieschatting voor de angulaire diversiteitsontvanger in aanwezigheid van voorafgaande informatie over de oriëntatie, en gelijktijdige positie- en oriëntatieschatting voor de apertuur-gecombineerde kwadrant-fotodiode (AQP) (in afwezigheid van voorafgaande informatie over de oriëntatie).

In het eerste onderwerp onderzoeken we het probleem van de gelijktijdige positie- en oriëntatieschatting (SPO) met behulp van de ontvangen signaalsterkte (RSS), voor ontvangers met hoekdiversiteit maar zonder een externe oriëntatie schatter. We ontwerpen twee SPO algoritmes die gebruik maken van het principe van optimalisatie op variëteiten, wat de restricties vereenvoudigt die opgelegd zijn door de rotatiematrix. Bovendien stellen we een initialisatiealgoritme voor, gebaseerd op het principe van directe lineaire transformatie (DLT), om een initiële schatting in gesloten vorm te verkrijgen voor de iteratieve algoritmes. Om de prestaties van de voorgestelde RSS-gebaseerde SPO algoritmes te evalueren, leiden we de Cramér-Rao limiet (CRB) af. Meer specifiek, de benodigde CRB op de oriëntatiefout is de intrinsieke CRB, m.a.w. de CRB voor variëteiten, waarbij de fout in de geschatte rotatiematrix op een fysisch betekenisvolle manier gemeten wordt. Computersimulaties tonen aan dat de performantie van de voorgestelde algoritmen de theoretische ondergrens asymptotisch dicht benadert, wat de doeltreffendheid van de voorgestelde oplossingen aantoont.

In het tweede onderwerp ontwerpen we een op RSS gebaseerd hybride algoritme voor positie- en oriëntatiebepaling. Dit algoritme maakt gebruik van het hybride maximum likelihood (ML)/maximum *a posteriori* (MAP) (HMM) principe voor ontvangers met hoekdiversiteit en een beschikbaar extern oriëntatieraamapparaat, en houdt rekening met de aanwezigheid van voorafgaande informatie over de oriëntatie. De voorgestelde HMM-schatter wordt vergeleken met drie schatters, namelijk de door ons voorgestelde SPO-schatter uit het eerste onderzoeksonderwerp, de bestaande foutgespecificeerde maximum likeli-

hood (MML)-schatter en het positioneringsalgoritme gebaseerd op de eerste orde benadering, onderhevig aan de oriëntatie-onzekerheid. Verder wordt, om de prestaties van de voorgestelde schatter analytisch te beoordelen, de hybride Cramér-Rao bound (HCRB) voor HMM afgeleid. Computersimulaties tonen aan dat de performantie van de voorgestelde schatter de bijbehorende theoretische ondergrens asymptotisch benadert.

In het laatste onderwerp stellen wij een kalibratie- en een SPO-schattingsalgoritme voor de AQPD voor (zonder een extern oriëntatie-instrument). Daartoe modelleren wij eerst de RSS van de AQPD als een functie van de PO en de uitlijningsfout van de ontvanger met behulp van het prospectieve projectiemodel. Vervolgens tonen we aan dat de algemeen toegepaste strategie van differentiëren en normaliseren op de RSS, waarvan in de meeste werken wordt beweerd dat het de robuustheid tegen RSS variaties verbetert, resulteert in een complexe kansdichtheidsfunctie (PDF), waardoor een effectieve en efficiënte schatting moeilijk te bekomen is. Daarom wordt een benaderde gesloten-vorm kansfunctie voorgesteld, op basis waarvan de kalibratie- en de SPO-schattingsalgoritmen met least squares (LS)-schatting worden afgeleid. De voorgestelde kalibratie vereist geen informatie over de PO van de ontvanger, wat de kalibratieprocedure vereenvoudigt, en is robuust voor variaties in het ontvangen vermogen. De overeenkomstige CRB op de geschatte uitlijningsfouten wordt ook afgeleid, om te worden gebruikt als indicator voor de benodigde signaal-ruisverhouding (SNR) of aantal LED's om een gewenste nauwkeurigheid te bekomen. Zowel de Monte Carlo simulatie als experimenten bevestigen de doeltreffendheid van de voorgestelde kalibratie- en SPO-schattingsalgoritmes.

1

Introduction

1.1 State-of-the-Art

With the development of technology and the upgrading of services, people's demand for location-based services (LBS) is increasing. In addition, modern humans spend 80% ~ 90% of their time in indoor environments [5], therefore, indoor LBS has a direct impact on people's work and life. In recent years, indoor LBS concepts have proliferated, and applications such as routing in large buildings, warehouse logistics management, assistive healthcare systems, location-based mobile advertising, and real-time Q&A revolving, etc, have been proposed. In order to realize these applications, the positioning technology is the key to support LBS.

The rapid development of wireless communication technology has provided a variety of solutions for positioning. Nowadays, the satellite positioning system represented by Global Positioning System (GPS) has become a mature and widely used outdoor positioning system with its advantages of wide coverage and high positioning accuracy. However, in indoor environments, the electromagnetic signals transmitted by satellites are obscured by building walls and floors, which makes GPS perform poorly in indoor and underground environments. In addition, the user requirements of different indoor positioning systems are diverse. Specific requirement parameters, such as accuracy, robustness, cost, coverage, latency, etc, depend on application scenarios [6]. Further, some LBS provides people with value-added services based on location information by combining wireless communication technology and positioning technology, so the deployed system is expected to combine communication and positioning. These challenges have prompted academia and industry to explore indoor positioning technologies that meet these requirements. The current mainstream indoor wireless positioning technologies include: WiFi [7], Bluetooth [8], radio frequency identification (RFID) [9], ultrawide band (UWB) [10], and so on. A comparison of these technologies is provided in Tab. 1.1. Since the need for low positioning costs and ubiquitous indoor positioning technologies is gaining importance, the current and future trend is to utilize existing infrastructure as much as possible to avoid the high time and labor costs of

Table 1.1: Comparison of indoor positioning technologies [1, 2]

Technology	Typical Accuracy (m)	Cost	Infrastructure	Advantage	Disadvantage
WiFi	1-7	Low	Reuses already installed WiFi infrastructure	Widely available, does not require complex extra hardware	Prone to noise, requires complex processing algorithms
UWB	0.1-0.3	High	Specialized infrastructure required	Immune to interference, provides high accuracy	Shorter range, high cost
RFID	1-2	Medium	Specialized infrastructure required	Consumes low power, has wide range	Low accuracy
Bluetooth	2-5	Medium	Specialized infrastructure required	Has high throughput, wide reception range, low energy consumption	Low accuracy, prone to noise
Ultrasound	0.1-0.3	High	Specialized infrastructure required	High accuracy	High dependence on sensor placement
Acoustics	0.4	Low	Specialized infrastructure required	Can be used for proprietary applications, can provide high accuracy	Affected by sound pollution, requires extra anchor points or hardware
VLP	0.01-0.35	Low	Reuses existing LED lighting infrastructure	Wide-scale availability, potential to provide high accuracy, multi-path free	Range is affected by obstacles, primarily requires line-of-sight

dedicated hardware deployment. Visible light communication (VLC)-based positioning or visible light positioning (VLP) is an emerging and highly promising technology that has the potential to meet the requirements of high accuracy, high ubiquity, and low positioning cost at the same time.

Visible light systems, have seen a rapid growth in recent years, behind which are two main driving factors, namely unregulated spectrum and ubiquitous indoor access. On the one hand, the demand for wireless transmission capacity, and thus the demand for spectrum, are continuously increasing, as result of the rapid popularization of high throughput applications (such as, augmented reality/virtual reality (AR/VR), high-resolution video, cloud computing, and cloud storage) and the explosive growth of wireless connected devices (such as, high-performance mobile devices, smart home devices, and wearable devices). The visible light spectrum provides an alternative unregulated spectrum to the already crowded radio frequency (RF) spectrum, as shown in Fig. 1.1. On the other hand, highly efficient and long-lasting white LEDs, which are gradually becoming the main source of light for illumination, can be modulated at frequencies up to several MHz. This is not possible with the conventional light devices such as fluorescent and incandescent lamps. Consequently, white LEDs can be used for wireless communication and positioning, making it possible to achieve high rate communication and positioning with low cost, low power consumption, and long lifetime [1]. As lighting infrastructure is required for human activities inherently, visible light systems are able to provide ubiquitous indoor access by reusing existing lighting infrastructures.

Besides, additional advantages of visible light systems are: 1) Visible light is environmentally friendly compared to RF solutions, which makes it feasible for electromagnetically sensitive environments; 2) Since visible light cannot penetrate opaque objects and walls, not only does this alleviate the inter-cell

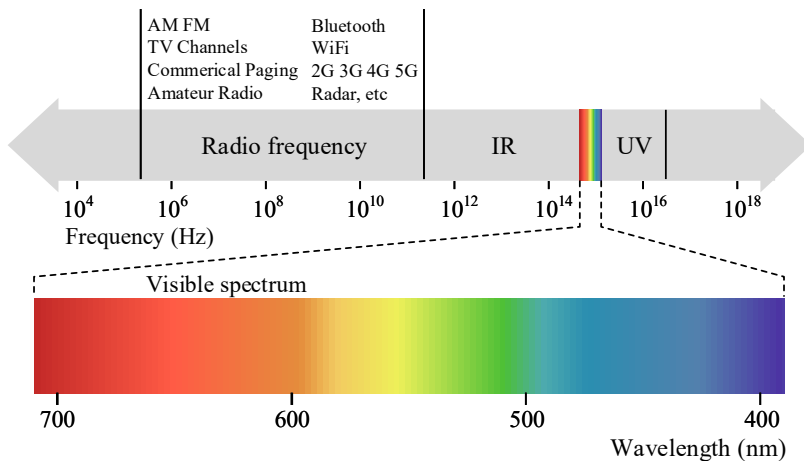


Figure 1.1: Electromagnetic spectrum.

interference and increase the capacity, but also it provides an inherent wireless communication security; 3) Since the visible light channel is largely sensitive to the distance and angle with respect to the transmitter, the visible light system is expected to estimate the receiver's position and/or orientation accurately. Potential applications/services, including but not limited to, are

- IoT applications: With the help of visible light systems, electronics used in indoor environments can be interconnected to realize IoT applications, such as smart homes, smart offices, and smart industry.
- Defense and security: Because visible light cannot be detected on the other side of a wall, visible light systems prevent eavesdropping through walls, which is particularly useful in the field of defense and security applications.
- Intelligent transport: Utilizing LEDs of vehicles and traffic infrastructures, visible light systems can be used for intelligent transport applications, such as vehicle-to-vehicle (V2V) communication, vehicle-to-infrastructure (V2I) communication, and LBS.
- Sensitive environment: Visible light systems provide an electromagnetic interference-free solution to communication and positioning, which can be used in many electromagnetically sensitive environments, such as hospitals, mines, petrochemical plants, and oil platforms, to achieve asset tracking, personnel tracking and data monitoring.

Depending on the type of sensor used at the receiver, indoor visible light positioning systems can be divided into photodiode (PD)-based and image-sensor-based systems, with their positioning algorithms designed on different signal features for each type of indoor visible light positioning system. On the one hand, the output of the image sensor is an image. This type of receiver first identifies (in combination with a proper multiplexing protocol) and determines the coordinates of multiple LEDs in an image. Once the coordinates of these LEDs in the image are obtained, the image transformation relating the positions of LEDs and their images is used to find the orientation and position of the receiver. For now, there are already some demonstrations of image-sensor-based systems. For example, Philips' image-sensor-based solution aimed at improving the shopping experience has been demonstrated in supermarkets such as Carrefour in Lille, France, EDEKA Parchman in Germany and Aswaaq in Dubai, United Arab Emirates. On the other hand, a PD is a solid-state device that senses incident light and converts it into an electric current. The current generated by the PD is proportional to the power of the incident light. As the light emitted from the LED propagates through the optical wireless channel, its intensity undergoes changes before reaching the PD, and this change is determined by the channel characteristics. The PD receiver processes the received signal (in combination with a proper multiplexing protocol) to obtain information about the characteristic of the received light signal from multiple

LEDs, for example, received signal strength (RSS), time difference of arrival (TDOA) or angle-of-arrival (AOA) information. Based on this characteristic information and its relation to the channel, algorithms can be designed to estimate the position (and orientation) of the receiver. Experimental results of works on PD-based systems showed that such systems can achieve centimeter-level 3D positioning accuracy [11, 12]. By comparison, camera-based receivers are able to provide accurate AOA information and benefits users with a simpler receiver structure, however, due to the frame rate limitation of cameras, the camera-based receiver might not provide a sufficient data rate for positioning which limits its applications, especially when the camera moves fast. This drawback becomes more apparent when we take into account communication, where LEDs are modulated at high frequencies to avoid flicker perceived by the human eye. In contrast, PD-based receivers consume less energy and can detect signals that are modulated at higher frequencies.

1.2 Problem Statement

As, compared to an image sensor, PDs consume less energy and can detect signals that are modulated at higher frequencies, most recent works focus on receivers consisting of one or more PDs. Compared to the single PD, the PD array, consisting of multiple PDs, has the ability to increase the receiver's field of view (FOV) and angular diversity by tilting the PDs in the array or using apertures [13, 14, 15]. As a result, receivers with multiple PDs have more reliable presence of line-of-sight paths and obtains more information, resulting in improved performance and reliability. Therefore, the PD array is gaining interest. Besides, since the visible light channel is largely sensitive to both the distance and angle with respect to the transmitter, a high-precision position estimate can only be achieved if the receiver's orientation is provided. However, if the orientation is not known, this should be taken into account when designing the estimation algorithm. This thesis studies the position and orientation estimation problem for the above mentioned structures with multiple PDs, i.e., the PD array with different PD tilt angles – angular diversity receiver – and the PD array combined with apertures – aperture-combined receiver.

Positioning using visible light is considered in many works [16]. However, research on the orientation of the receiver is limited. The effects of unknown orientation were investigated in some papers. In [17], a study of an unknown tilt orientation of the receiver shows that, if not properly dealt with, tilting has an impact of significant degradation on the performance. The effect of unknown transmitter and receiver orientations on the channel gain is investigated in [18]. The results show that the effect of an unknown orientation increases with the distance between transmitter and receiver. Most works on VLP restrict their attention to the special case where the orientation of the receiver is parallel to the transmitter or the ceiling, and some works [19, 20, 21, 22, 17, 18] consider the performance of the VLP system when the receiver is tilted. In [19], a method to compensate for the RSS changes caused by the tilted orientation

is proposed, and the conclusion is that if the compensation is applied, the tilting only results in a slight degradation of the performance, while [21] takes advantage of angular diversity provided by the tilted orientation of the receiver to improve the performance. In [22], the authors analyze the VLP performance for a tilted receiver. These papers assume the orientation is perfectly known in advance, i.e., an external device is used to determine the orientation of the receiver, which, however, is a strong assumption in reality.

On the one hand, an external orientation estimation device is not always available for the receiver. For such a case, the estimator has to simultaneously estimate the position and orientation from the observed light signal only. Recently, several simultaneous position and orientation estimation (SPO) algorithms for VLC with a single PD using RSS have been proposed in [23, 24]. In these papers, a receiver consisting of a single PD is considered, and the orientation of the PD is represented by its normal vector. Although this representation is simple, it has several limitations. Firstly, the normal vector representation is blind to the change in yaw angle, i.e. the representation can not reflect the heading direction. Although this flaw has little impact on the receiver with a single PD in terms of channel gain, the representation fails whenever the heading estimation is required. Secondly, for receivers equipped with multiple PDs or a PD array, the receiver moves and rotates in a rigid manner, and changes in yaw angle of the receiver will affect all PDs that are not at the rotation center. Therefore, a more general representation of the orientation is required, allowing to describe the orientation with three degrees of freedom, e.g. by using the rotation matrix description.

On the other hand, even if the receiver is equipped with an external orientation estimation device, in most cases, the external orientation estimation device is a Micro-Electro-Mechanical System (MEMS)-based inertial measurement unit (IMU), as the cost and power consumption of such devices is low. The drawback of using these devices is their low accuracy, i.e. they suffer from severe biases and drift problems, especially when the receiver, which is carried by a user or attached to a carrier, experiences some random movement. Consequently, even if the receiver determines its orientation with an external orientation estimation device, the estimated orientation is subject to noise and orientation errors, meaning the instantaneous orientation is not perfectly known [3, 4]. Most positioning algorithms extracting the orientation information from an external device often neglect the uncertainty generated by the external device and assume the orientation is perfectly estimated. As this orientation uncertainty largely affects the positioning performance of state-of-the-art algorithms, it should be taken into account in the design of a positioning algorithm. To the best of our knowledge, there are only a few works [25, 26] on estimators taking into account the presence of prior information on the orientation. In [25], the authors derive a theoretical bound to analyze the performance of a receiver with a single PD. Because, in this paper, the orientation of the PD is also represented by its normal vector, it has the same drawback of the lacking of degrees of freedom. The work [26] analyzed the characteristics of

the received signal strength subject to the orientation uncertainty, using the rotation matrix description, for a receiver consisting of a single PD. Based on a first-order approximated likelihood function, it designed an RSS-based position estimator using the maximum likelihood principle. However, this approach cannot be extended directly to the receiver consisting of a PD array, as not only the approach used in [26] is a positioning only algorithm, i.e, it treats the orientation as a nuisance parameter, but also applying this approach to a PD array system would result in biased estimates due to the approach's inconsistency.

This thesis focuses on the position and orientation estimation for visible light systems, particularly those with multiple LEDs and multiple PDs. We will design estimators in the presence and absence of prior information on the orientation, respectively, and will also study the corresponding theoretical lower bounds. The research will carefully consider both the receivers of angular diversity structure and aperture-combined structure. We will conduct simulations and experiments to evaluate performances of proposed algorithms.

1.3 Contributions and Publications

In this thesis, three topics of position and orientation estimation for visible light systems involving multiple LEDs and multiple PDs are investigated for the previously given problems. Specifically, the first topic – simultaneous position and orientation estimation (SPO) for angular diversity receivers – investigates the SPO problem for angular diversity receivers without an external orientation estimation device. The second topic – hybrid position and orientation estimation for angular diversity receiver in the presence of prior orientation information – investigates the SPO problem for angular diversity receivers with an available external orientation estimation device. The last topic – simultaneous position and orientation estimation for aperture-combined quadrant photodiode (AQPD) receiver – investigates the SPO problem for the AQPD receiver (a special type of aperture-combined receivers) under the assumption that no external orientation estimation device is available.

During the course of the work, the following papers were written:

1. Journal Publications

- **Shengqiang Shen**, Shiyin Li, and Heidi Steendam. "Simultaneous Position and Orientation Estimation for Visible Light Systems With Multiple LEDs and Multiple PDs." *IEEE Journal on Selected Areas in Communications* 38, no. 8 (2020): 1866-1879.
- Shiyin Li, **Shengqiang Shen**, and Heidi Steendam. "A Positioning Algorithm for VLP in the Presence of Orientation Uncertainty." *Signal Processing* 160 (2019): 13-20.

2. Abstracts

- **Shengqiang Shen**, and Heidi Steendam. "An RSS Approximation for Visible Light Positioning in the Presence of Orientation Uncertainty."

26th Symposium on Communications and Vehicular Technology in the Benelux (SCVT 2019).

3. Other Articles

- **Shengqiang Shen**, Shiyin Li, and Heidi Steendam. "Hybrid Position and Orientation Estimation for Visible Light Systems in the Presence of Prior Information on the Orientation." submitted to *IEEE Transaction on Wireless Communications*.
- **Shengqiang Shen**, Jose Miguel Menéndez Sánchez, Shiyin Li, and Heidi Steendam. "Simultaneous Position and Orientation Estimation for Visible Light Systems using Aperture-combined Quadrant Photodiode." in preparation.

1.4 Outline

Chapter 2 introduces the basic concepts that are used throughout the rest of the work. We overview fundamental parts of the visible light system under consideration. Particularly, the physical characteristics of LEDs and PDs are introduced, and the line-of-sight (LOS) and the noise in the visible light system are modeled and analyzed. The modulation scheme is introduced and the system architecture is outlined. Finally, two types of receiver structures are highlighted.

Chapter 3 provides some basic principles from the estimation theory and optimization on $SO(3)/SE(3)$ that are useful for designing estimators. They form the basis for the derivation of algorithms to perform the estimation of the receiver's position and orientation.

Chapter 4 investigates the simultaneous position and orientation estimation for angular diversity receiver. Two RSS-based SPO algorithms using the optimization on manifolds principle are first derived, together with the expression of the theoretical bound. Subsequently, the closed-form solution for coarse estimation using the DLT is discussed. The numerical results and comparison of the proposed methods with the theoretical bound are given for evaluation. The optimal design of the PD receiver diversity is investigated in this chapter as well.

Chapter 5 deals with the hybrid position and orientation estimation for angular diversity receiver in the presence of prior information on the orientation. We first introduce the model of orientation uncertainty from an external orientation estimation device. The RSS-based hybrid position and orientation estimation algorithm using the HMM principle is then designed. Subsequently, the expression for the theoretical bound is derived. Numerical results comparing the proposed algorithm with state-of-the-art algorithms, and the comparison with the theoretical lower bound, are given and discussed.

Chapter 6 focuses on the simultaneous position and orientation estimation for aperture-combined quadrant photodiode. The strategy of differencing and

normalization is analyzed with its PDF. An approximated PDF is derived, and a calibration system model is designed. The calibration along with the SPO estimation algorithms using the least squares principle are proposed. Subsequently, the theoretical bound is derived. The Monte Carlo numerical comparison as well as the real experimental evaluation are given.

Chapter 7 presents the general conclusions of this thesis and discusses possible directions for future work.

2

Fundamentals of Visible Light System

This chapter first details the physical properties of LEDs and PDs and analyzes in detail the characteristics of visible light LOS channels and noise. Then the most commonly used modulation scheme for visible light systems is introduced and the system architecture is outlined. Finally, the structures of two types of receivers with multiple PDs are highlighted. By providing the models used throughout the thesis, this chapter serves as the basis for subsequent chapters.

2.1 Physical Aspects

2.1.1 Properties of LEDs

Let us consider the conversion of a voltage signal to an optical signal by a LED. As a special type of diode, the LED has the property of the unidirectional conduction, i.e, a LED conducts current only when the forward voltage across the LED exceeds its threshold value V_T . In addition, the conducted current varies nonlinearly with the input voltage. As illustrated by the red curve in Fig. 2.1, only a limited range of the voltage-current characteristic curve of LEDs can be regarded as linear. Further, the conducted current leads the LED to illuminate, and usually, the optical power of a LED can be regarded as linearly proportional to the current, as illustrated by the green curve in Fig. 2.1. Hence, when the input voltage signal exceeds this linear range, the output optical signal will suffer from nonlinear distortion, which causes unwanted effects on the signals.

A driven LED radiates light according to the radiation pattern scaled by the optical power. Since the radiation pattern and the optical power are the main factors determining the RSS value, we will briefly introduce the LED's radiation pattern and the optical power. The radiation pattern of a LED specifies the radiance in a particular direction. This pattern is determined by the LED packaging, which usually includes a LED die, a lens, a reflector cup,

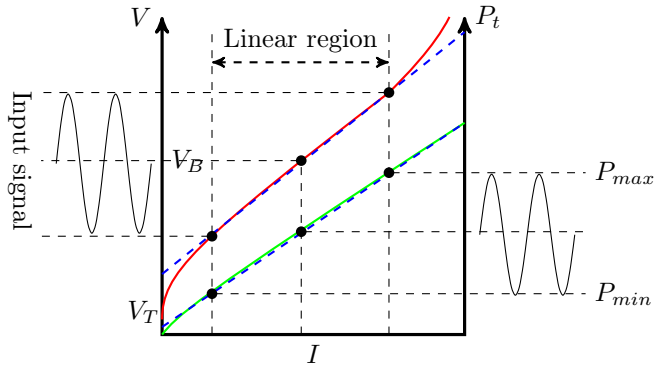


Figure 2.1: Optical-power-current-voltage characteristic curve.

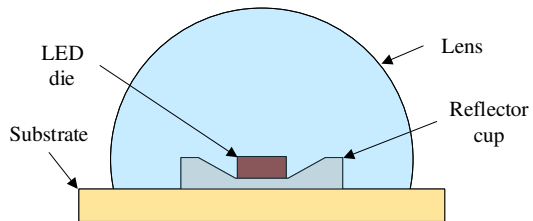


Figure 2.2: LED packaging.

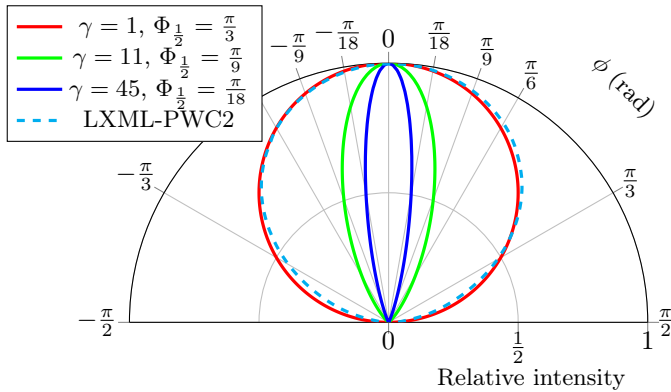


Figure 2.3: Normalized Lambertian pattern.

and a substrate, as illustrated in Fig. 2.2. The radiation pattern is the net result of the shape of the reflector cup, the size and design criteria of the LED die, and the geometry and the material of the lens [27]. Most off-the-shelf LEDs radiate light according to a generalized Lambertian pattern [28]. This implies the radiation pattern can be modeled as

$$R_o(\phi) = \frac{(\gamma + 1)}{2\pi} \cos^\gamma(\phi) \Pi\left(\frac{\phi}{\phi_{FOV}}\right),$$

where the Lambertian order $\gamma = -\ln 2 / \ln(\cos \Phi_{\frac{1}{2}})$, $\Phi_{\frac{1}{2}}$ denotes the half-power angle and depends on the LED packaging, ϕ is the radiation angle at the LED and $\Pi(\cdot)$ is a rectangular window indicating that light is emitted only at angles smaller than the LED's field of view ϕ_{FOV} . Fig. 2.3 shows the radiation pattern for $\Phi_{\frac{1}{2}} = \{\frac{\pi}{3}, \frac{\pi}{9}, \frac{\pi}{18}\}$, along with the pattern of the LUXEON Rebel ES LED (LXML-PWC2). It can be seen that a small $\Phi_{\frac{1}{2}}$ leads to a large Lambertian order and to a narrow and concentrated radiation pattern, and that the LXML-PWC2 complies with the first-order Lambertian pattern.

As optical devices designed for illumination, commercial white LEDs are optimized for the human eye and are usually characterized by photometric quantities instead of radiometric quantities. The photometric quantity describes the perceived brightness to the human eye, while the radiometric quantity, such as the optical power P_t , measures the radiant energy in terms of absolute power. Since the human eye and the PD have different responses to different wavelengths, it is important to derive P_t from an appropriate photometric quantity. The optical transmit power P_t can be obtained by integration of the radiation spectrum, as

$$P_t = P_p \int_{\lambda_{min}}^{\lambda_{max}} p_\lambda(\lambda) d\lambda, \quad (2.1)$$

where $p_\lambda(\lambda)$, as a function of wavelength λ , is the normalized radiation spectrum with a peak value of 1, and P_p is the peak value of the (non-normalized) ra-

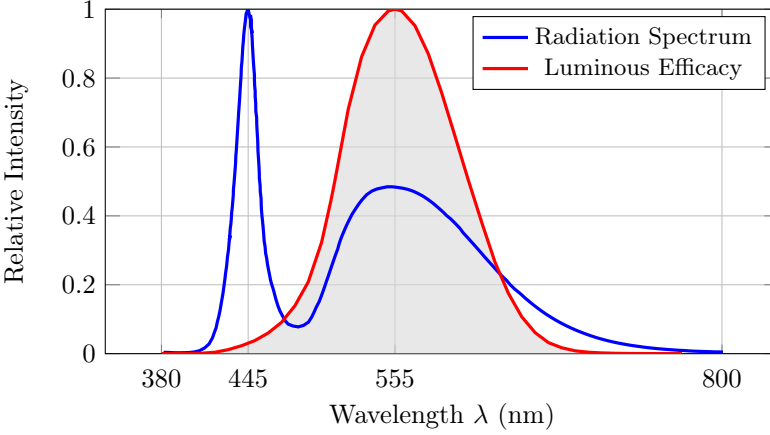


Figure 2.4: Normalized radiation pattern of LXML-PWC2, along with the luminous efficacy of human eyes.

radiation spectrum. Most manufacturers provide the normalized radiation spectrum (or equivalently the normalized color spectrum) as shown in Fig. 2.4 but not P_p . Instead, they provide the luminous flux Φ_v , i.e., the photometric quantity measuring the perceived power of light, which is linked to P_p by

$$\Phi_v = P_p V_p \int_{\lambda_{min}}^{\lambda_{max}} p_\lambda(\lambda) v_\lambda(\lambda) d\lambda, \quad (2.2)$$

where $v_\lambda(\lambda)$, as a standardized function of wavelength λ , is the normalized luminous efficacy with a peak value of 1. The luminous efficacy measures the human eye's sensitivity to light spectrum, and it has a peak value of $V_p = 683 \text{ lm/W}$ at 555 nm, where the eye is most sensitive. Taking both (2.1) and (2.2) into account, we obtain

$$P_t = \frac{\Phi_v \int_{\lambda_{min}}^{\lambda_{max}} p_\lambda(\lambda) d\lambda}{V_p \int_{\lambda_{min}}^{\lambda_{max}} p_\lambda(\lambda) v_\lambda(\lambda) d\lambda}. \quad (2.3)$$

As an example, the white LED of LXML-PWC2 has a luminous flux $\Phi_v = 320 \text{ lm}$ for an input electrical power of $P_e = 3.1 \text{ W}$ (corresponding to a forward current of 1000 mA and a forward voltage of 3.1 V). Using (2.3), we obtain the optical power $P_t = 0.99 \text{ W}$, which results in a power factor $\eta_P = P_t/P_e = 0.32$. This calculated power factor agrees with the discussion in [29].

2.1.2 Properties of PDs

The PD is a solid-state device that senses incident light and converts it into an electric current. The current generated by the PD is proportional to the

power of the incident light. In order to improve the quality of the received signal, an optical filter and/or a concentrator can be installed in front of the PD, where the filter attenuates the out-of-band radiation (such as the infrared radiation), and the concentrator increases the effective area of the bare PD. Then the output of the PD is amplified by a transimpedance amplifier (TIA) before being further processed. The TIA is preferably used for sensors whose current response is more linear than the voltage response, as is the case with PDs.

Together with a filter and a concentrator, a PD achieves an effective collection area $A_e(\theta)$, which depends on the incident angle and is given by

$$A_e(\theta) = A_R T_F(\theta) G_C(\theta) \cos(\theta) \Pi\left(\frac{\theta}{\theta_{FOV}}\right),$$

where A_R is the active area of the bare PD, θ is the incidence angle at the PD, $T_F(\theta)$ is the filter gain, $G_C(\theta)$ is the concentrator gain, and $\Pi(\theta/\theta_{FOV})$ indicates that no light will be detected by the PD if the incident angle is larger than the field-of-view angle θ_{FOV} . After the light travels over a distance v from a LED, the irradiance attenuates with a factor v^2 , i.e., light intensity at distance v and radiation angle ϕ equals

$$I_s(v, \phi) = P_t R_o(\phi) / v^2, \quad (2.4)$$

where P_t denotes the LED's optical power. Then the received optical power, given by

$$P = I_s(v, \phi) A_e(\theta), \quad (2.5)$$

is converted into an electrical signal by the PD. The rate at which the PD converts the received optical power into an electrical signal is decided by the PD's material and is modeled by the responsivity $R_p(\lambda)$ of the PD. Fig. 2.5 illustrates the $R_p(\lambda)$ of the PD FDS010 as a function of wavelength. Assuming that the incident light undergoes the same attenuation for all wavelengths, we can calculate the average responsivity as

$$\bar{R}_p = \frac{\int_{\lambda_{min}}^{\lambda_{max}} R_p(\lambda) p_\lambda(\lambda) d\lambda}{\int_{\lambda_{min}}^{\lambda_{max}} p_\lambda(\lambda) d\lambda} \quad (2.6)$$

As an example, with a PD of FDS010 and a LED of LXML-PWC2, the average responsivity is $\bar{R}_p = 0.27$ A/W.

2.1.3 Channel Model

Usually, light can reach the active area of a PD via a direct path – LOS channel – or after being reflected at least once – NLOS channel –, as shown in Fig. 2.6. In this thesis, we assume that the influence of the NLOS channel is negligible and that the LOS channel dominates¹.

¹The impact of the NLOS channel is evaluated in Appendix A. It can be seen that when the reflectivity of the environment is low and the receiver moves within an area with a certain distance from the wall, the assumption is valid.

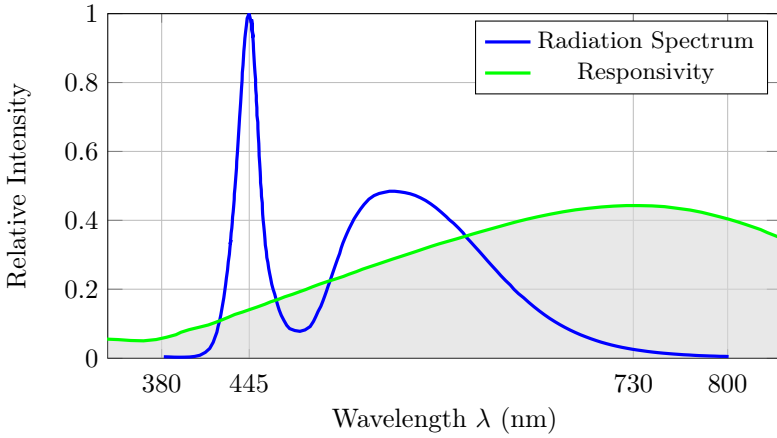


Figure 2.5: The responsivity $R(\lambda)$ of FDS010, along with the normalized radiation pattern of LXML-PWC2.

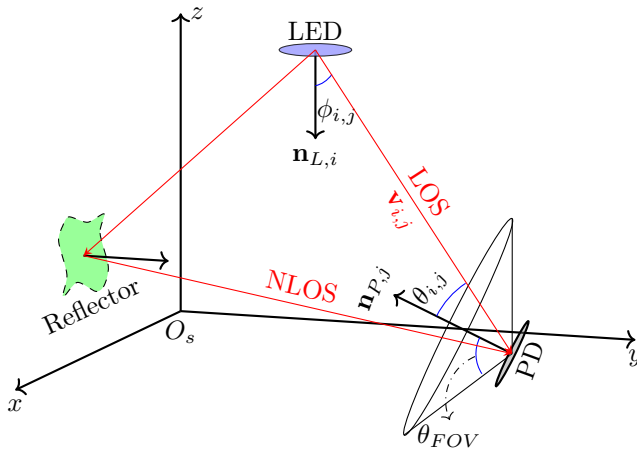


Figure 2.6: LOS and NLOS links between a PD and a LED.

Taking both (2.4) and (2.5) into account, we obtain the LOS channel gain model for a LED-PD pair [28, eq. (10)]:

$$h = \frac{(\gamma + 1) A_R}{2\pi v^2} \cos^\gamma(\phi) T_F(\theta) G_C(\theta) \cos(\theta) \Pi\left(\frac{\theta}{\theta_{FOV}}\right) \Pi\left(\frac{\phi}{\phi_{FOV}}\right), \quad (2.7)$$

where h is defined as the ratio between the PD's incident optical power and LED's output optical power, factor $\Pi(\theta/\theta_{FOV}) \cdot \Pi(\phi/\phi_{FOV})$ in (2.7) implies that a PD can detect the light only when the LED is within its FOV, and the PD itself is within the FOV of the LED, i.e. when $0 \leq \theta \leq \theta_{FOV}$ and $0 \leq \phi \leq \phi_{FOV}$. Further, we assume that the receiver is made of bare PDs with ideal bandpass optical filters of visible light and that no concentrator is used, then (2.7) can be simplified as

$$h = \frac{(\gamma + 1) A_R}{2\pi v^2} \cos^\gamma(\phi) \cos(\theta) \Pi\left(\frac{\theta}{\theta_{FOV}}\right) \Pi\left(\frac{\phi}{\phi_{FOV}}\right), \quad (2.8)$$

which is also valid for the receiver with omnidirectional optical filter and omnidirectional concentrator up to a constant factor. Eqn. (2.8) is the general formula for the LOS channel gain made from a combination of a LED and a PD. However, since special structures are assumed for the receiver, we will reformulate the LOS channel gain after taking into account the structure later.

2.1.4 Noise Analysis

There are several noise sources in a visible light system, e.g., shot noises induced by the desired signal and the ambient light, dark current produced by the PD, and the thermal and shot noise from the preamplifier. Since the shot noise of ambient light and the thermal noise from the preamplifier dominate these noise sources [28], we will neglect other noise sources. Thermal noise is normally modeled with a Gaussian distribution, while shot noise is normally Poisson distributed due to the discrete nature of the photons incident on the PD. However, the intense ambient light striking the detector leads to a steady high-intensity shot noise [28, 30], and when the intensity of shot noise is high, the statistics become that of a Gaussian random process [31]. Therefore, we can model the noise in a visible light system as a Gaussian process, which is assumed by most works on VLC and VLP, e.g. [24, 22, 16, 32].

The one-sided power spectral density (PSD) of the photocurrent induced by the ambient light is given by [28, eq. (15)]

$$N_0 = 2q\bar{R}_p P_n, \quad (2.9)$$

where q is the electronic charge, the received ambient optical power P_n is

$$P_n = p_n \Delta\lambda_n T_0 A_R n^2, \quad (2.10)$$

and p_n with an unit of $\text{W}/(\text{cm}^2 \text{nm})$ is the average spectral irradiance over the bandwidth $\Delta\lambda_n$ of the optical filter, T_0 is the peak transmission of the optical

filter, and n is the refractive index of the concentrator. For a given amplifier noise density I_a and a electrical bandwidth B , the noise variance σ_w^2 can be calculated as [33, eq. (6)]

$$\sigma_w^2 = (N_0 + I_a^2)B \quad (2.11)$$

For a transmitted power P_t , the received SNR is defined as

$$\text{SNR}_R \triangleq \left(\frac{R_p P_t h}{\sigma_w} \right)^2. \quad (2.12)$$

However, since the received SNR depends on the receiver's position and orientation (PO), fixing the received SNR in the simulation will set a confinement on the parameter space of receiver's PO. To solve this complication, we instead use the SNR defined as

$$\text{SNR} \triangleq \left(\frac{(\gamma+1)A_R P_t R_p}{2\pi\sigma_w} \right)^2 \quad (2.13)$$

which discards the position- and orientation-related dependency in the received power. Taking into account the definition of the channel gain h (2.8), it follows that the received SNR is proportional to the above defined SNR by a factor $\left(\frac{2\pi h}{(\gamma+1)A_R} \right)^2$. In other words, the used SNR is equal to the received SNR for a PD, right below a LED and pointing to that LED, i.e. $\theta = \phi = 0$ rad, at a distance of $v = 1$ m.

As an example, assuming a background spectral irradiance $p_n = 5.8 \times 10^{-6}$ W/(cm² · nm) with an ideal optical filter of visible light bandwidth $\Delta\lambda = 360$ nm [14] and without concentrator, the shot noise to a circular PD with radius of 1 mm has power spectral density $N_0 = 5.25 \times 10^{-23}$ A²/Hz. Further assuming an amplifier noise density $I_a = 5 \times 10^{-12}$ A/ $\sqrt{\text{Hz}}$ [33] and an electrical bandwidth $B = 1$ MHz [34], the noise variance is $\sigma_w^2 = 2.13 \times 10^{-17}$ A². Considering an optical transmit power $P_t = 1$ W, an average responsivity $R_p = 0.3$ A/W, an area $A_R = \pi r_P^2$ with radius $r_P = 1 \times 10^{-3}$ m, an optical transmit power $P_t = 1$ W, and a Lambertian order $\gamma = 1$, this results in an SNR = 34.6 dB.

2.2 (De)Modulation Scheme

For optical wireless systems, the scheme of intensity modulation - direct detection (IM/DD) is preferred to the coherent scheme because of its low cost and simplicity. As opposed to the coherent scheme that modulates both the amplitude and phase of the light at the transmitter and uses heterodyne or homodyne detection at the receiver, the IM/DD scheme only modulates the intensity of the light at the transmitter and directly detects the intensity of the light at the receiver; no frequency conversion is involved. Since the IM/DD is already the de facto method of implementing optical wireless systems, in this thesis, we will only consider the IM/DD scheme.

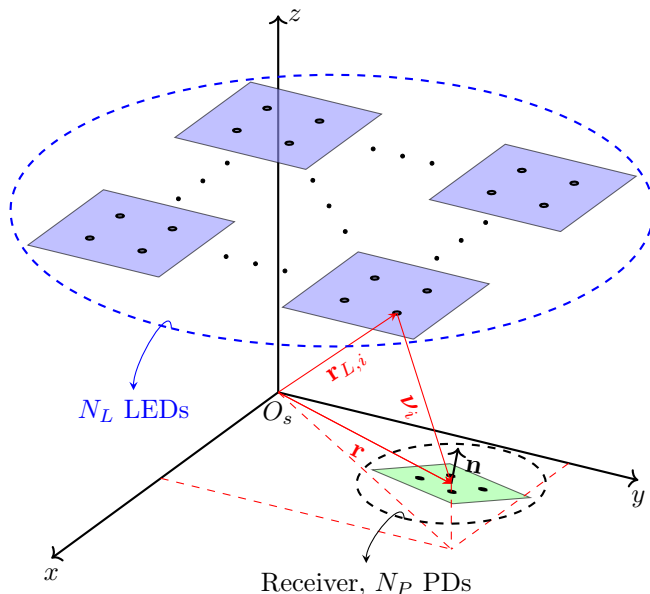


Figure 2.7: System model of N_L LEDs and N_P PDs.

The IM/DD scheme requires the modulation signal to be real-valued and positive due to the unidirectional conduction of the LED, otherwise the portion of the signal below the threshold will be clipped. As an example, for a pure sinusoidal wave taking on both negative or positive values, a DC bias must be added to it so that the amplitude of this composite signal must always be greater than the threshold voltage to avoid clipping.

2.3 System Overview

In this thesis, we consider a system containing N_L LEDs and a receiver containing N_P PDs with neither optical filters nor concentrators, i.e., bare PDs, as shown in Fig. 2.7. More specifically, we assume that the system adopts a frequency-division multiplexing (FDM) protocol (each LED is modulated by a DC-biased sinusoidal wave with a distinctive frequency) and that all devices are properly tuned to operate in the linear region, so that each PD is able to separate the signals from the different LEDs². Then each combination of a LED and a PD forms a single link, and the total observation consists of the RSS values from every link. For each link, the block diagram is shown in Fig.

²Since the DC bias terms at the receiver is usually difficult to separate for different LEDs and that the ambient light induces a DC noise component, the system is assumed to utilize only the AC part of the transmitted optical power. Therefore, in the following, when we talk about the transmitted optical power, we refer to the AC part of the transmitted optical power.

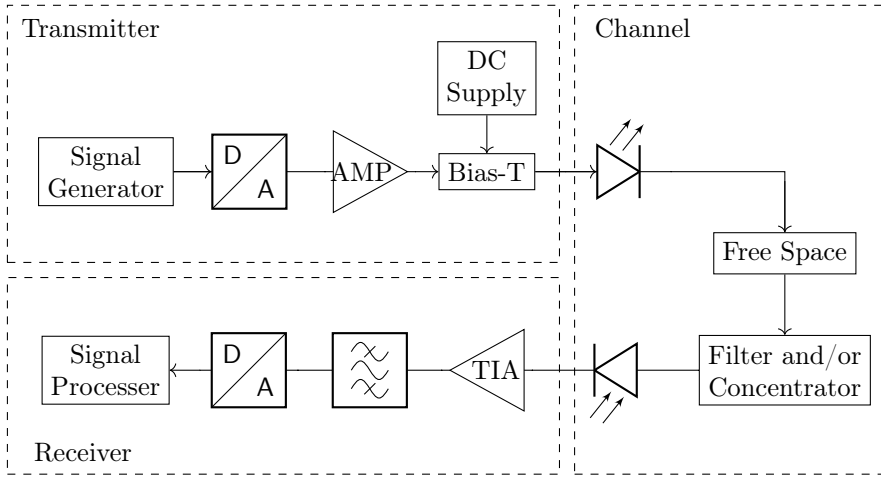


Figure 2.8: Block diagram of a single link for the visible light system.

2.8, where three key components, i.e., transmitter, receiver and channel, are highlighted in dashed boxes. Note that the LED is physically installed at the transmitter, but it is usually included as a part of the channel model, so are the PD, the filter and/or the concentrator at the receiver. In the following, we will describe the transmitter and receiver in sequence.

2.3.1 Transmitter

At the transmitter end, the generated signal is first converted into a corresponding analog signal by a digital-to-analog converter and then amplified, as shown in the transmitter-sub-box in Fig. 2.8. The Bias-T circuit is used to bias the mean of the generated signal to the center of the linear range of the LED, and the modulation index is adjusted to keep the biased signal within the linear range.

2.3.2 Receiver

At the receiver end, the output of the PD is amplified by a TIA and then fed to an analog-to-digital converter to extract RSS information. Since each LED is modulated by a DC-biased sinusoidal wave with a distinctive frequency, the RSS information can be extracted using power spectrum analysis. We assume that all LEDs' coordinates, normals, and properties (such as brightness, radiation pattern and modulation settings) are known by the receiver.

2.3.3 Coordinate Systems

Since all PDs are placed rigidly on the receiver, i.e., all PDs translate and rotate along with the receiver but preserve their relative distances and relative

orientations, it is easier to define the structure (including the coordinates and orientations of each PD) in a frame that is fixed to the receiver, i.e., the receiver frame. In addition, the presentation of the PO of the receiver in a frame fixed to the environment, i.e., the system frame, is more useful for LBS. Therefore, we will consider two coordinate systems, namely, the receiver and system frames, and the receiver's PO presentation in the system frame can be used to transform coordinates between these two systems. We will use an extra subscript r to indicate coordinates represented in the receiver frame, i.e. the coordinates \mathbf{x}_r in the receiver frame corresponds its counterpart \mathbf{x} in the system frame. And these coordinates are linked by a transformation function $\mathbf{x}_r = f(\mathbf{x})$.

Let us now define some generic notations that will be used throughout the work. For the transmitter part, it is assumed that the i^{th} LED of the system has coordinates $\mathbf{r}_{L,i} \in \mathbb{R}^{3 \times 1}$ and normal $\mathbf{n}_{L,i} \in \mathbb{R}^{3 \times 1}$, i.e. the direction in which the LED is radiating. The position and the orientation of the receiver in the system frame are denoted by $\mathbf{r} \in \mathbb{R}^{3 \times 1}$ and $\mathbf{R} \in SO(3)^3$, respectively, where the receiver's normal \mathbf{n} , i.e. the normal of the receiver plane, is expressed by $\mathbf{n} = \mathbf{R}\mathbf{n}_0$ with the reference normal $\mathbf{n}_0 = [0 \ 0 \ 1]^T$, as shown in Fig. 2.7.

2.4 Receiver Structures with Multiple PDs

For a receiver with multiple PDs, special care is needed when designing the structure of the receiver in order to avoid the channel matrix is ill-conditioned. In general, the distance between the PDs of a receiver is very small compared with the LED-PD distance, the channel gains between a LED and PDs with identical normal are highly correlated, resulting in ill-conditioning. One common approach to solve this problem is to provide the receiver with angular diversity. This idea leads to two different designs, i.e., the angular diversity receiver and the aperture-combined receiver. In an angular diversity receiver, PDs are oriented at different directions to achieve the angular diversity, while the aperture-combined receiver uses an additional aperture structure to obtain angular diversity. In the rest part of this section, these two receiver structures will be discussed and modeled in detail.

2.4.1 Angular Diversity Receiver

The angular diversity receiver, which is considered in several works [35, 36, 37, 38], consists of multiple PDs oriented symmetrically at different directions to achieve a better angular diversity. More specifically, $N_{P,s}$ PDs are placed symmetrically around the center of the receiver, and are tilted away from the center of the receiver, as shown in Fig. 2.9.

Recall that the subscript r corresponds to coordinates in the receiver frame. The frame of the receiver, as shown in Fig. 2.10, is defined by setting the origin O_r to the centroid of the receiver. The coordinates of the j^{th} PD are specified by

³ $SO(3)$ is the special orthogonal group, i.e., the set of all rotation matrices. More details on $SO(3)$ is given in Section 3.2.

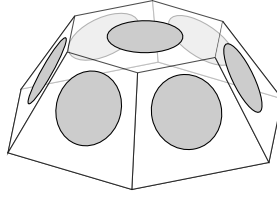


Figure 2.9: Angular diversity receiver with $N_{P,s} = 6$

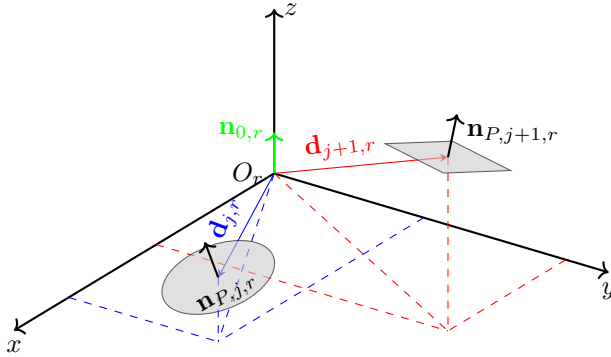


Figure 2.10: Coordinates and orientations of PDs in the receiver frame.

a relative distance vector $\mathbf{d}_{j,r} \in \mathbb{R}^{3 \times 1}$ to the origin, while the normal of the j^{th} PD is specified by a rotation matrix $\mathbf{R}_{P,j} \in SO(3)$ with respect to a reference orientation $\mathbf{n}_{0,r}$, i.e. $\mathbf{n}_{P,j,r} = \mathbf{R}_{P,j} \mathbf{n}_{0,r}$, where $\mathbf{R}_{P,j}$ is assumed to be known and fixed. As the reference orientation, we select the normal of the receiver plane, i.e. $\mathbf{n}_{0,r} = [0 \ 0 \ 1]^T$, as shown in Fig. 2.10. Further, let the angle between the normal of the receiver and the normal of a PD be θ_P . Using the axis-angle representation, the normal of the j^{th} PD is specified by $\mathbf{n}_{P,j,r} = \exp((\theta_P \mathbf{z}_{P,j})^\wedge) \mathbf{n}_0$, where the operator \cdot^\wedge converts a vector into a skew-symmetric matrix, the matrix exponential function $\exp(\cdot)$ converts the skew-symmetric matrix into a rotation matrix⁴, and $\mathbf{z}_{P,j} = [\cos(j2\pi/N_{P,s}), \sin(j2\pi/N_{P,s}), 0]^T$ is the unit vector in the $x - y$ plane of the receiver so that the j^{th} PD has an azimuth angle of $j2\pi/N_{P,s} - \pi/2$. The relative distance vector $\mathbf{d}_{j,r}$ that specifies the position of j^{th} PD to the center of the receiver is given by $\mathbf{d}_{j,r} = d_j \mathbf{n}_{P,j,r}$, i.e. $\mathbf{d}_{j,r}$ is parallel to $\mathbf{n}_{P,j,r}$. An additional PD placed right above the center of the receiver has normal \mathbf{n}_0 . Thus, the receiver has a total of $N_P = N_{P,s} + 1$ PDs.

In order to obtain the channel model for the angular diversity receiver, we first convert the structure definition into the frame of the system. The coordinates of the j^{th} PD, denoted by $\mathbf{r}_{P,j}$, are given by $\mathbf{r}_{P,j} = \mathbf{r} + \mathbf{d}_j$, where $\mathbf{d}_j = \mathbf{R} \mathbf{d}_{j,r}$, and the normal of the j^{th} PD is specified by $\mathbf{n}_{P,j} = \mathbf{R} \mathbf{n}_{P,j,r}$.

⁴A more detailed introduction to rotation matrices and their mathematical operations is given in Section 3.2.

Assuming the vector $\boldsymbol{\nu}_i = \mathbf{r} - \mathbf{r}_{L,i}$ is the vector between the i^{th} LED and the receiver centroid, the incidence vector between the i^{th} LED and the j^{th} PD of the receiver is $\mathbf{v}_{i,j} = \boldsymbol{\nu}_i + \mathbf{d}_j$. Using this definition, as shown in Fig. 2.6, we find the distance $v_{i,j}$ between the i^{th} LED and the j^{th} PD, the radiation angle $\phi_{i,j}$, i.e. the angle between $\mathbf{v}_{i,j}$ and the normal $\mathbf{n}_{L,i}$ of the LED, and the incidence angle $\theta_{i,j}$, i.e. the angle between $-\mathbf{v}_{i,j}$ and the normal $\mathbf{n}_{P,j}$ of the PD:

$$v_{i,j} = \|\mathbf{v}_{i,j}\|, \quad (2.14)$$

$$\cos(\phi_{i,j}) = \frac{\mathbf{n}_{L,i}^T \mathbf{v}_{i,j}}{\|\mathbf{v}_{i,j}\|} = \frac{\mathbf{n}_{L,i}^T (\boldsymbol{\nu}_i + \mathbf{d}_j)}{\|\boldsymbol{\nu}_i + \mathbf{d}_j\|}, \quad (2.15)$$

$$\cos(\theta_{i,j}) = -\frac{\mathbf{n}_{P,j}^T \mathbf{v}_{i,j}}{\|\mathbf{v}_{i,j}\|} = -\frac{\mathbf{n}_{P,j}^T (\boldsymbol{\nu}_i + \mathbf{d}_j)}{\|\boldsymbol{\nu}_i + \mathbf{d}_j\|}. \quad (2.16)$$

Taking into account (2.14)–(2.16), (2.8) can be rewritten as

$$h_{i,j} = K_{i,j} \frac{(\mathbf{n}_{L,i}^T (\boldsymbol{\nu}_i + \mathbf{R}\mathbf{d}_{j,r}))^\gamma}{\|\boldsymbol{\nu}_i + \mathbf{R}\mathbf{d}_{j,r}\|^{\gamma+3}} (\mathbf{R}\mathbf{R}_{P,j}\mathbf{n}_0)^T (\boldsymbol{\nu}_i + \mathbf{R}\mathbf{d}_{j,r}), \quad (2.17)$$

where $K_{i,j} = -\frac{(\gamma+1)A_{R,j}\Pi_{i,j}}{2\pi}$ and $\Pi_{i,j} = \Pi(\theta_{i,j}/\theta_{FOV}) \cdot \Pi(\phi_{i,j}/\phi_{FOV})$.

2.4.2 Aperture-Combined Receiver

This second type of receiver is composed of PDs and apertures. The aperture is chosen so that its size is very large compared to the wavelength of the light, and it is placed at a specific height above and parallel to the PD. As a result [15], the light reaching the PD is the light that passes through its aperture, and the incident light will cast a light spot on the PD plane in the same shape as the aperture⁵. There are two available designs for the aperture-combined receiver. The first one is composed of multiple receiving elements (REs), each of which is made of a bare PD and an aperture [39,40]. And the second one, a more compact one, is based on a quadrant PD (QPD) combined with a single aperture, i.e. the aperture-combined QPD (AQPD), which was proposed for visible light positioning (VLP) in [34]. In the rest of this thesis, we will focus on the AQPD receiver.

The QPD is a segmented photodiode consisting of four matched PDs on a single chip, separated by very thin gaps, as shown in Fig. 2.11. Even though these four PDs are deposited on a single chip, each PD is an individual channel, namely, the QPD is a special PD array with a compact structure. The QPD is widely used to track a laser beam, by detecting the position of the light spot from the laser on its surface. The light spot on the QPD's surface, as shown in Fig. 2.12, leads the QPD to produce a unique 4-tuple of RSS values

⁵In practice, the receiver is assembled by housing a PD and an aperture, so that the light can only reach the PD through the aperture. The impact of the internal reflection inside the house is evaluated in Appendix B. It can be seen that the impact of the reflection is negligible.

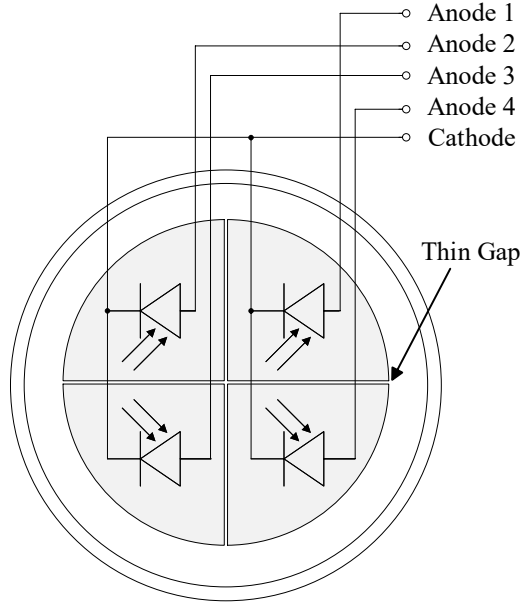


Figure 2.11: Structure of quadrant photodiode.

proportional to the overlap areas, i.e., the RSS output is uniquely determined by the position of light spot. Because of this, the position of the light spot can be estimated from the RSS values, which in turn e.g. is useful in detecting an object's angle coordinates [41]. The above principle of estimating the position of a laser light spot from the RSS values of a QPD can be exploited by the receiver of a visible light system to create a light spot of a visible light LED on the QPD with the help of an aperture [34]. In this approach, we place an opaque screen with a circular aperture at a specific height above and parallel to the surface of the QPD, as shown in Fig. 2.13⁶. The position of the light spot in the QPD plane not only depends on the position of the light source, but also on the PO of the receiver, implying the RSS outputs in the constituent PDs of the QPD are functions of the position of the light source and the PO of the receiver.

For the AQPD receiver, the receiver frame is defined with its $x - y$ plane being the plane of the aperture and the z axis being the normal to that plane. The origin O_r of this receiver frame coincides with the center of the aperture.

The channel gain for the AQPD receiver is determined by the radiation pattern of the LED and the irradiance attenuation, implying the incident power at the QPD (and thus the optical power in the light spot) depends on the

⁶Note that this AQPD has a similar structure as the sun position sensor described in [42]. However, while the sun position sensor only needs to track a single light source, i.e. the sun, the AQPD in this thesis needs to be able to extract the signals and positions of the different LEDs, with a higher accuracy than needed for the sun positioning sensor.

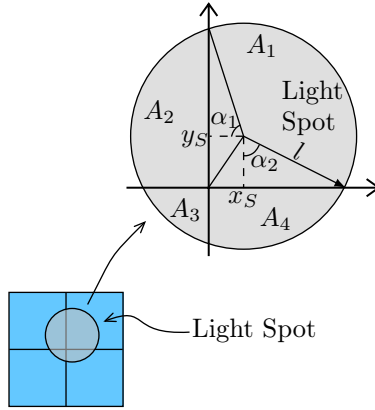


Figure 2.12: Geometry of the light spot of a light beam.

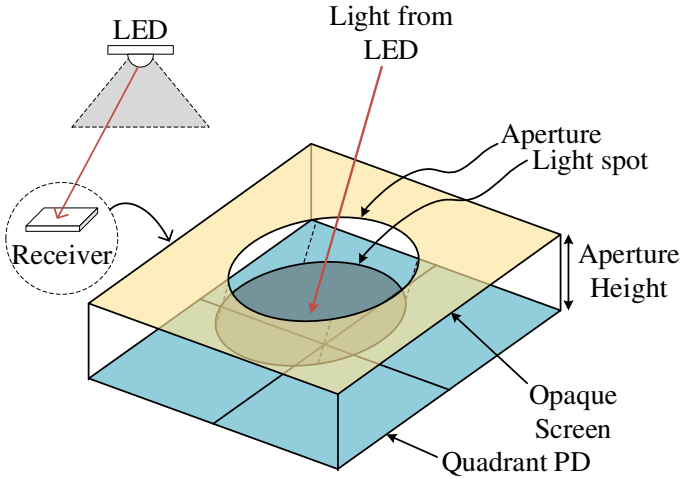


Figure 2.13: Structure of AQPD.

relative PO of the receiver with respect to the LED. Besides, the RSS values in the quadrants are proportional to the overlap areas of the light spot with the quadrants of the QPD. Let $\mathbf{r}_{S,i}$ denote the position of the light spot made by the i^{th} LED in the system frame. We define the distance vector between the i^{th} LED and the light spot as $\mathbf{v}_i = \mathbf{r}_{S,i} - \mathbf{r}_{L,i}$. With this definition, we can write the distance v_i between the LED and the light spot, the radiation angle ϕ_i , i.e. the angle between \mathbf{v}_i and the normal $\mathbf{n}_{L,i}$ of the LED, and the incidence angle θ_i , i.e. the angle between the vector $-\mathbf{v}_i$ and the normal \mathbf{n}_Q of the QPD as:

$$v_i = \|\mathbf{v}_i\|, \quad (2.18)$$

$$\cos(\phi_i) = \frac{\mathbf{n}_{L,i}^T \mathbf{v}_i}{\|\mathbf{v}_i\|}, \quad (2.19)$$

$$\cos(\theta_i) = -\frac{\mathbf{n}_Q^T \mathbf{v}_i}{\|\mathbf{v}_i\|}. \quad (2.20)$$

Denoting the overlap area vector $\mathbf{A}_i = [A_1, \dots, A_4]^T$ with A_j the overlap area of the j th quadrant, $j = 1, \dots, 4$ and taking into account (2.8) and (2.18-2.20), the channel gain vector is given by

$$\mathbf{h}_i = -\frac{(\gamma + 1) \Pi_{\phi, \theta, i} (\mathbf{n}_{L,i}^T \mathbf{v}_i)^\gamma \mathbf{n}_Q^T \bar{\mathbf{v}}_i}{2\pi \|\mathbf{v}_i\|^{\gamma+3}} \mathbf{A}_i. \quad (2.21)$$

2.5 Conclusion

In this chapter, we present the basic concepts of the visible light system. The properties of off-the-shelf LEDs and PDs, including optical and electrical properties, are discussed, and the LOS channel model is presented in detail. Noise effects are also reviewed and the definition of SNR is given. The most commonly used modulation scheme in visible light systems is then presented and the system architecture is outlined. The rest of this chapter focuses on the structures of two types of multiple PDs receivers, i.e. the angular diversity receiver and the aperture-combined quadrant photodiode receiver, whose models are described and formulated. This chapter provides basic concepts and models for the following chapters of this thesis.

3

Estimation Theory and Basics of $SO(3)/SE(3)$

The target of this thesis, i.e., estimation of the position and orientation from the observation provided by the receiver, is an application of estimation theory, which allows to extract the value of a parameter set Θ from a noisy observation vector \mathbf{y} . The estimation theory provides fundamental principles to be satisfied by an optimal estimate, and its implementation leads us to the corresponding estimator. However, when the resulting estimate is a nonlinear function of \mathbf{y} , it is usually impossible to directly get a closed-form solution of the optimal estimate, and numerical optimization methods have to be used to obtain the solution. Further, we will see that in our case of position and orientation estimation, not only is the estimation for our problems nonlinear, but (a part of or all of) the parameter set Θ also lies in a special set, i.e., the special orthogonal group $SO(3)$ or the special Euclidean group $SE(3)$, which belongs to the matrix Lie Group and comes with its own constraints. As a result, in order to calculate the optimal estimate, the straightforward solution is to resort to a constrained optimization algorithm, which is usually complex and time-consuming. Instead, as we will see, the optimization can be achieved in a simple but robust way using the properties of $SO(3)/SE(3)$, which updates the estimate within the valid set, i.e., intrinsically satisfying the constraints, so that unconstrained optimization is achieved.

In this chapter, we will discuss these two aspects, i.e., the estimation theory leading to the optimal estimator and the basics of $SO(3)/SE(3)$.

3.1 Estimation Problems

There are four key components in an estimation model, i.e., the parameter space, a probabilistic transition mechanism, an observation space, and the estimation rule. The parameter space is the domain of the unknown parameter Θ . Since the observation \mathbf{y} is corrupted by noise, the mapping from the parameter space to the observation space is modeled by a probabilistic transition mecha-

nism $p(\mathbf{y}|\Theta)$ parameterized by Θ . The estimation rule gives the mapping from a given observation into an estimate $\hat{\Theta}$. Two main classes of estimation rules can be identified, depending on whether prior information on the parameter Θ is available or not, namely, the classical approach for situations without prior information or otherwise the Bayesian approach. In what follows, we will first introduce the maximum likelihood (ML) estimation and the maximum *a posteriori* (MAP) estimation, which are well-established estimation rules for the problem assuming a known $p(\mathbf{y}|\Theta)$, with and without prior information on Θ , respectively. Later, the estimation rule of hybrid ML/MAP (HMM) estimation is discussed as well. The HMM estimation deals with the special case where only part of parameter set Θ has prior information. The last principle, the least squares (LS) estimation, is also introduced, which does not require $p(\mathbf{y}|\Theta)$ but only makes the assumption about the model of \mathbf{y} . Additionally, since the estimation rule operates on the random observation \mathbf{y} , the resulting estimate $\hat{\Theta}$ is also a random variable. Therefore, there is an inherent concern about the goodness of the particular estimator in question. To this end, we will take a close look at the Cramér-Rao bound and its variants, which give fundamental limits on the minimum achievable mean squared estimation error of estimators. The above estimation rules¹ and corresponding bounds all assume that $p(\mathbf{y}|\Theta)$ is correctly specified. A misspecified $p(\mathbf{y}|\Theta)$ affects the performance of estimators, therefore, in this chapter, we will also introduce the effect of a misspecified $p(\mathbf{y}|\Theta)$ on the estimate and the concept of misspecified maximum likelihood (MML) estimation.

3.1.1 ML Estimation

For the classical estimation problem, assuming that there is no prior information on the parameter set, the estimator needs to find an estimate based only on observation. For an observed vector \mathbf{y} , the PDF $p(\mathbf{y}|\Theta)$, when viewed as a function of the unknown parameter set Θ (with \mathbf{y} fixed), measures the likelihood for a given value of the parameter set, and is called the likelihood function. The goal of ML estimation is to find the parameter values that maximize the likelihood function over the parameter space. Further, since in many cases the PDF belongs to the exponential family and since logarithms are strictly increasing functions, it is more convenient to work with the log-likelihood function in ML estimation, as

$$\hat{\Theta}_{ml} = \arg \max_{\Theta} \mathcal{L}(\Theta; \mathbf{y}) \quad (3.1)$$

where $\mathcal{L}(\Theta; \mathbf{y}) = \ln p(\mathbf{y}|\Theta)$ is the log-likelihood function.

¹Even though the LS estimation does not require $p(\mathbf{y}|\Theta)$, it is equivalent to the ML estimation for a normal distributed $p(\mathbf{y}|\Theta)$. Therefore, the performance of the LS estimation still depends on the properties of $p(\mathbf{y}|\Theta)$.

3.1.2 MAP Estimation

It can be seen that $p(\mathbf{y}|\Theta)$ specifies the information from observation \mathbf{y} , and if the unknown parameter set Θ possesses a prior information $p(\Theta)$, those two information measures can be combined by applying Bayes' rule as

$$p(\Theta|\mathbf{y}) = \frac{p(\mathbf{y}|\Theta)p(\Theta)}{p(\mathbf{y})}, \quad (3.2)$$

where $p(\Theta|\mathbf{y})$ is the posterior distribution of Θ . The method of MAP estimation estimates Θ by finding the values of the parameter set that maximizes the posterior distribution over the parameter space. And, for the same reason as above, the MAP estimation finds

$$\hat{\Theta}_{map} = \arg \max_{\Theta} \mathcal{L}_B(\Theta; \mathbf{y}), \quad (3.3)$$

where

$$\mathcal{L}_B(\Theta; \mathbf{y}) = \ln p(\mathbf{y}|\Theta) + \ln p(\Theta), \quad (3.4)$$

is the Bayesian log-likelihood function. Notice that the effect of denominator $p(\mathbf{y})$ in (3.2) is neglected, because it is not a function of Θ .

3.1.3 HMM Estimation

Assume the parameter set Θ can be written as a hybrid set

$$\Theta = \begin{bmatrix} \Theta_d \\ \Theta_r \end{bmatrix}, \quad (3.5)$$

where Θ_d is the part without prior information and Θ_r is the part with prior information $p(\Theta_r|\Theta_d)$. The HMM estimator finds the estimate $\hat{\Theta}$ that maximizes the joint PDF $p(\mathbf{y}, \Theta_r|\Theta_d)$ over the parameter space, where

$$p(\mathbf{y}, \Theta_r|\Theta_d) = p(\mathbf{y}|\Theta)p(\Theta_r|\Theta_d), \quad (3.6)$$

and

$$\begin{aligned} \hat{\Theta}_{hmm} &= \begin{bmatrix} \hat{\Theta}_{d,ml} \\ \hat{\Theta}_{r,map} \end{bmatrix} \\ &= \arg \max_{\Theta} \mathcal{L}_H(\Theta; \mathbf{y}). \end{aligned} \quad (3.7)$$

The hybrid log-likelihood function $\mathcal{L}_H(\Theta; \mathbf{y})$ in (3.7) is defined as

$$\mathcal{L}_H(\Theta; \mathbf{y}) = \ln p(\mathbf{y}|\Theta) + \ln p(\Theta_r|\Theta_d), \quad (3.8)$$

3.1.4 LS Estimation

Assume the observation vector \mathbf{y} is given by

$$\mathbf{y} = \mathbf{g}(\Theta) + \mathbf{n}, \quad (3.9)$$

where the signal model \mathbf{g} as a function of Θ is known. We make no probabilistic assumptions about the noise vector \mathbf{n} . The LS estimation is defined to be

$$\hat{\Theta}_{ls} = \arg \min_{\Theta} \|\mathbf{y} - \mathbf{g}(\Theta)\|^2. \quad (3.10)$$

We can see that the LS estimation is identical to the ML estimation, thus

$$\hat{\Theta}_{ls} = \hat{\Theta}_{ml}, \quad (3.11)$$

if we model the noise \mathbf{n} as independent and identically distributed Gaussian $\mathcal{N}(\mathbf{0}, \sigma_n^2 \mathbf{I})$.

3.1.5 Measures of Error

The estimation error, denoted as Θ_e , gives a measure of the residual error between the estimated and true parameters. The measure is induced by the structure of parameter space, for instance, the measure in Euclidean space is given by the distance $\Theta_e \triangleq \hat{\Theta} - \Theta$, and the distance in $SO(3)$ will be given in the next section. As stated, the estimate $\hat{\Theta}$ given by the estimator is a random variable, so will the estimation error Θ_e also be. Therefore, the performance of an estimator is usually measured by the mean squared error (MSE) of its estimate, which is defined as

$$\text{MSE}(\Theta) = E_{\mathbf{y}} \{ \Theta_e \Theta_e^T \}. \quad (3.12)$$

Due to the presence of noise, the estimation error cannot be arbitrarily small, and the minimum achievable MSE is specified by the theoretical lower bound. The most well known theoretical lower bounds include the Cramér-Rao Lower bound (CRB), which is a lower bound on the MSE for an unbiased estimator without prior information, and the variants of the CRB, which are applicable to other conditions of prior information. The lower bound for the MSE is given by

$$\text{MSE}(\Theta) \succeq \mathbf{J}_X^{-1}, \quad (3.13)$$

where the subscript $X \in \{F, B, H\}$ of the information matrix \mathbf{J}_X indicates under which condition of prior information the lower bound applies. Next, we will discuss these information matrices and the corresponding lower bounds in turn.

For a parameter set without prior information, the Fisher information matrix (FIM) \mathbf{J}_F is given by

$$\mathbf{J}_F = E_{\mathbf{y}} \{ \nabla_{\Theta} \ln p(\mathbf{y}|\Theta) \cdot \nabla_{\Theta}^T \ln p(\mathbf{y}|\Theta) \}$$

$$= -E_{\mathbf{y}} \{ \Delta_{\Theta}^{\Theta} \ln p(\mathbf{y}|\Theta) \}, \quad (3.14)$$

where $\nabla_{\mathbf{x}}$ is the partial derivative matrix operator, and $\Delta_{\mathbf{x}}^{\mathbf{z}} \triangleq \nabla_{\mathbf{z}} \nabla_{\mathbf{x}}^T$ denotes the Hessian operator. The resulting lower bound is the classical CRB, i.e., $\text{CRB} = \mathbf{J}_F^{-1}$.

When all elements of the parameter possess prior information, the Bayesian information matrix \mathbf{J}_B is given by

$$\begin{aligned} \mathbf{J}_B &= E_{\mathbf{y}, \Theta} \{ \nabla_{\Theta} \ln p(\mathbf{y}, \Theta) \cdot \nabla_{\Theta}^T \ln p(\mathbf{y}, \Theta) \} \\ &= -E_{\mathbf{y}, \Theta} \{ \Delta_{\Theta}^{\Theta} \ln p(\mathbf{y}, \Theta) \}. \end{aligned} \quad (3.15)$$

The resulting lower bound is the Bayesian CRB (BCRB), i.e., $\text{BCRB} = \mathbf{J}_B^{-1}$.

When only the parameter part Θ_r of (3.5) possess prior information, the hybrid information matrix (HIM) \mathbf{J}_H is given by

$$\begin{aligned} \mathbf{J}_H &= E_{\mathbf{y}, \Theta_r | \Theta_d} \{ \nabla_{\Theta} \ln p(\mathbf{y}, \Theta_r | \Theta_d) \cdot \nabla_{\Theta}^T \ln p(\mathbf{y}, \Theta_r | \Theta_d) \} \\ &= -E_{\mathbf{y}, \Theta_r | \Theta_d} \{ \Delta_{\Theta}^{\Theta} \ln p(\mathbf{y}, \Theta_r | \Theta_d) \}. \end{aligned} \quad (3.16)$$

The resulting lower bound is the hybrid CRB (HCRB), i.e., $\text{HCRB} = \mathbf{J}_H^{-1}$. The HIM can be divided into two parts

$$\mathbf{J}_H = \mathbf{J}_D + \mathbf{J}_P, \quad (3.17)$$

where

$$\mathbf{J}_D = E_{\Theta_r | \Theta_d} \{ \mathbf{J}_F \}, \quad (3.18)$$

and

$$\begin{aligned} \mathbf{J}_P &= E_{\Theta_r | \Theta_d} \{ \nabla_{\Theta} \ln p(\Theta_r | \Theta_d) \nabla_{\Theta}^T \ln p(\Theta_r | \Theta_d) \} \\ &= -E_{\Theta_r | \Theta_d} \{ \Delta_{\Theta}^{\Theta} \ln p(\Theta_r | \Theta_d) \}. \end{aligned} \quad (3.19)$$

The \mathbf{J}_D term in (3.18) represents the contribution of the data (the observation), while the \mathbf{J}_P term in (3.19) represents the contribution of the prior information. In the case where Θ_r is independent of Θ_d , i.e.

$$p(\Theta_r | \Theta_d) = p(\Theta_r), \quad (3.20)$$

we have

$$\mathbf{J}_D = E_{\Theta_r} \{ \mathbf{J}_F \}, \quad (3.21)$$

and

$$\mathbf{J}_P = \begin{bmatrix} \mathbf{0} & \mathbf{0} \\ \mathbf{0} & -E_{\Theta_r} \{ \Delta_{\Theta_r}^{\Theta_r} \ln p(\Theta_r) \} \end{bmatrix}. \quad (3.22)$$

Now, let us take a look at the MML estimation. The MML estimation is not an estimation rule designed for some particular estimation problem. On the contrary, it is a term coined to describe the case where the ML estimation is

applied to a misspecified model². That is, the MML estimation is the designed ML estimation based upon a misspecified PDF $p_m(\mathbf{y}|\Theta)$ instead of the true one $p(\mathbf{y}|\Theta)$. The misspecification is a result of either imperfect knowledge of the true model or the intention to simplify the analytical derivation and implementation of an algorithm. In the first case, the misspecified PDF $p_m(\mathbf{y}|\Theta)$ represents a model that was previously considered accurate, while the PDF $p(\mathbf{y}|\Theta)$ represents a more accuracy model that is later discovered as the knowledge of the system at hand develops. In the later case, the misspecified PDF $p_m(\mathbf{y}|\Theta)$ represents an approximated model to the known true model $p(\mathbf{y}|\Theta)$, which is intended to simplify the implementation of the estimator.

Following the ML estimation rule under the misspecified PDF $p_m(\mathbf{y}|\Theta)$, the MML estimate is the one that maximizes the misspecified log-likelihood function, that is,

$$\hat{\Theta}_{mml} = \arg \max_{\Theta} \mathcal{L}_M(\Theta; \mathbf{y}), \quad (3.23)$$

where $\mathcal{L}_M(\Theta; \mathbf{y}) = \ln p_m(\mathbf{y}|\Theta)$ is the misspecified log-likelihood function. The MML estimation results in biased estimates that converge (with respect to the SNR and number of the observation) to [43, eq. (1)]

$$\hat{\Theta} = \arg \min_{\Theta} D(p(\mathbf{y}|\Theta) || p_m(\mathbf{y}|\tilde{\Theta})), \quad (3.24)$$

where $D(p(\mathbf{y}|\Theta) || p_m(\mathbf{y}|\tilde{\Theta}))$ is the Kullback-Leibler divergence (KLD) between the true and the misspecified PDFs.

There is also a CRB-like theoretical lower bound called misspecified CRB (MCRB) for the MML estimator, which is given by

$$\text{MCRB}(\Theta) = (\mathbf{M}_1(\hat{\Theta}))^{-1} \mathbf{M}_2(\hat{\Theta}) (\mathbf{M}_1(\hat{\Theta}))^{-1} + \text{Bias}(\hat{\Theta}, \Theta), \quad (3.25)$$

where the matrices \mathbf{M}_1 , \mathbf{M}_2 , and $\text{Bias}(\hat{\mathbf{r}}, \mathbf{r})$ are respectively given by

$$\mathbf{M}_1(\hat{\Theta}) = E_{\mathbf{y}|\Theta} \left\{ \Delta_{\Theta}^{\Theta} \ln p_m(\mathbf{y}|\Theta) \Big|_{\Theta=\hat{\Theta}} \right\}, \quad (3.26)$$

$$\mathbf{M}_2(\hat{\Theta}) = E_{\mathbf{y}|\Theta} \left\{ (\nabla_{\Theta} \ln p_m(\mathbf{y}|\Theta) \cdot \nabla_{\Theta}^T \ln p_m(\mathbf{y}|\Theta)) \Big|_{\Theta=\hat{\Theta}} \right\}, \quad (3.27)$$

and

$$\text{Bias}(\hat{\Theta}, \Theta) = \hat{\Theta}_e \hat{\Theta}_e^T. \quad (3.28)$$

As in general, $p(\mathbf{y}|\Theta) \neq p_m(\mathbf{y}|\mathbf{r}; \tilde{\mathbf{R}})$, the matrices \mathbf{M}_1 and \mathbf{M}_2 are in general not equal [43].

3.2 Basics of $SO(3)/SE(3)$

3.2.1 The Groups of $SO(3)$ and $SE(3)$

For the problem of position and orientation estimation, the parameter to be estimated is the set $\Theta = \{\mathbf{R}, \mathbf{r}\}$, where $\mathbf{R} \in SO(3)$ is an orientation matrix

²There is also a Bayesian version under misspecified models, which is however beyond the scope of this thesis, the interested reader may refer to [43].

Table 3.1: Matrix Lie group properties for $SO(3)$ and $SE(3)$

Property	$SO(3)$	$SE(3)$
Closure	$\forall \mathbf{R}_1, \mathbf{R}_2 \in SO(3)$ $\Rightarrow \mathbf{R}_3 = \mathbf{R}_1 \mathbf{R}_2 \in SO(3)$	$\forall \mathbf{T}_1, \mathbf{T}_2 \in SE(3)$ $\Rightarrow \mathbf{T}_3 = \mathbf{T}_1 \mathbf{T}_2 \in SE(3)$
Associativity	$\forall \mathbf{R}_1, \mathbf{R}_2, \mathbf{R}_3 \in SO(3)$ $\Rightarrow \mathbf{R}_1 (\mathbf{R}_2 \mathbf{R}_3) = (\mathbf{R}_1 \mathbf{R}_2) \mathbf{R}_3$	$\forall \mathbf{T}_1, \mathbf{T}_2, \mathbf{T}_3 \in SE(3)$ $\Rightarrow \mathbf{T}_1 (\mathbf{T}_2 \mathbf{T}_3) = (\mathbf{T}_1 \mathbf{T}_2) \mathbf{T}_3$
Identity	$\exists! \mathbf{I}_3 \in SO(3), \forall \mathbf{R} \in SO(3)$ $\Rightarrow \mathbf{R} \mathbf{I}_3 = \mathbf{I}_3 \mathbf{R} = \mathbf{R}$	$\exists! \mathbf{I}_4 \in SE(3), \forall \mathbf{T} \in SE(3)$ $\Rightarrow \mathbf{T} \mathbf{I}_4 = \mathbf{I}_4 \mathbf{T} = \mathbf{T}$
Invertibility	$\forall \mathbf{R} \in SO(3)$ $\Rightarrow \mathbf{R}^{-1} \in SO(3)$	$\forall \mathbf{T} \in SE(3)$ $\Rightarrow \mathbf{T}^{-1} \in SE(3)$

and $\mathbf{r} \in \mathbb{R}^{3 \times 1}$ is a position vector. The special orthogonal group $SO(3)$ is the set of square matrices satisfying

$$SO(3) = \{ \mathbf{R} \in \mathbb{R}^{3 \times 3} \mid \mathbf{R}^T \mathbf{R} = \mathbf{R} \mathbf{R}^T = \mathbf{I}, \det(\mathbf{R}) = +1 \}. \quad (3.29)$$

In some cases, it is more convenient to represent the position and orientation in a compact form as elements of the special Euclidean group, $\mathbf{T} \in SE(3)$.

$$SE(3) = \left\{ \mathbf{T} = \begin{bmatrix} \mathbf{R} & \mathbf{r} \\ \mathbf{0}^T & 1 \end{bmatrix} \in \mathbb{R}^{4 \times 4} \mid \mathbf{R} \in SO(3), \mathbf{r} \in \mathbb{R}^{3 \times 1} \right\}. \quad (3.30)$$

The groups $SO(3)$ and $SE(3)$ do not form a vector space, as generally

$$\mathbf{R}_1 + \mathbf{R}_2 \notin SO(3), \text{ for } \mathbf{R}_1, \mathbf{R}_2 \in SO(3). \quad (3.31)$$

Instead they belong to the matrix Lie group. The matrix group is a set of matrices for which the following four group axioms are satisfied: closure, associativity, identity and invertibility. More specifically, this translates into the properties as shown in Tab. 3.1 for $SO(3)$ and $SE(3)$.

Moreover, as special cases of Lie group, $SO(3)$ and $SE(3)$ also have the structure of a differentiable manifold, i.e., intuitively their elements are organized continuously and smoothly, so that we can use differential calculus on $SO(3)$ and $SE(3)$.

3.2.2 The Gradient of Functions on $SO(3)/SE(3)$

The estimation rule introduced in Section 3.1 leads to an objective function. Let $f(\mathbf{R}) \in \mathbb{R}$ be a real-valued objective function defined on $\mathbf{R} \in SO(3)$. When it is impossible to find a closed-form solution to the objective function, a numerical optimization method has to be applied. Further, since \mathbf{R} is a member of $SO(3)$ rather than an arbitrary 3×3 real matrix, \mathbf{R} has to satisfy the following constraints:

$$\mathbf{R}^T \mathbf{R} = \mathbf{R} \mathbf{R}^T = \mathbf{I}, \quad \det(\mathbf{R}) = +1. \quad (3.32)$$

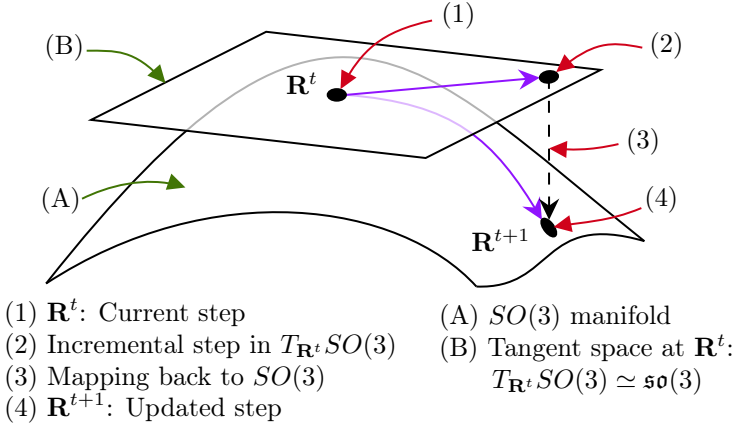


Figure 3.1: Optimization on $SO(3)$ manifold.

To find an optimal point of f constrained by (3.32), we can resort to a constrained non-linear optimization algorithm, which is complex, time consuming and non-robust. However, since $SO(3)$ is an embedded submanifold of $\mathbb{R}^{3 \times 3}$, we can estimate the parameters in $SO(3)$ using an (iterative) optimization algorithm on manifolds [44]. While in the standard optimization algorithm, the estimated variable and incremental step are in the same Euclidean space, in the optimization algorithm on manifolds, the estimated variable and incremental step are located in different spaces, i.e. the estimated variable in the manifold and the incremental step size in the associated tangent space. In each iteration, the algorithm calculates the incremental steps in the tangent space $\mathfrak{so}(3)$ to the manifold $SO(3)$, and then those incremental steps are mapped back on the manifold again to update the steps, which is elaborated in detail in Fig. 3.1³. Since the optimization is iteratively progressed in the manifolds, it relieves the restrictions imposed by the constraints (3.32), simplifying the optimization process. As a result, by viewing the optimization problem in the $SO(3)$ manifold, the problem reduces to an unconstrained non-linear problem that can be solved using the principle of optimization on manifolds.

The gradient⁴ of f with respect to \mathbf{R} is calculated by introducing an in-

³Strictly speaking, $\mathfrak{so}(3)$ is the Lie algebra of $SO(3)$ and is the tangent space at \mathbf{I} , while the tangent space at \mathbf{R}^t is isomorphic to $\mathfrak{so}(3)$ or $T_{\mathbf{R}^t}SO(3) \simeq \mathfrak{so}(3)$. More specifically, $T_{\mathbf{R}^t}SO(3)$ is the set of all matrices Δ such that $(\mathbf{R}^t)^T \Delta \in \mathfrak{so}(3)$. The gradient given later corresponds to the equivalent incremental step in $\mathfrak{so}(3)$ instead of the one in $T_{\mathbf{R}^t}SO(3)$.

⁴The formal definition of the gradient requires many mathematical concepts that are not relevant to what follows. Therefore, we only give the method for calculating the gradient, and the interested reader is referred to [45, p. 48] for the formal definition. This calculation is a result of a proposition given in [45, p. 49], but there are other ways to calculate the gradient, for example, using the relation between the submanifold and the embedding Euclidean space

finitesimal perturbation $\exp(\boldsymbol{\omega}^\wedge)$ as [46, eqs. (7.174) and (7.177)]

$$\begin{aligned} \nabla_{\mathbf{R}} f(\mathbf{R}) &= \frac{\partial}{\partial \boldsymbol{\omega}} \bigg|_{\boldsymbol{\omega}=\mathbf{0}} f(\exp(\boldsymbol{\omega}^\wedge) \mathbf{R}) \\ &\triangleq \begin{bmatrix} \frac{d}{dt} \big|_{t=0} f(\exp(te_1^\wedge) \mathbf{R}) \\ \frac{d}{dt} \big|_{t=0} f(\exp(te_2^\wedge) \mathbf{R}) \\ \frac{d}{dt} \big|_{t=0} f(\exp(te_3^\wedge) \mathbf{R}) \end{bmatrix}, \end{aligned} \quad (3.33)$$

where \mathbf{e}_i is a unit basis vector with its i^{th} element being 1, the operator \cdot^\wedge converts a 3×1 vector into $\mathfrak{so}(3)$, which is,

$$\begin{bmatrix} a_1 \\ a_2 \\ a_3 \end{bmatrix}^\wedge = \begin{bmatrix} 0 & -a_3 & a_2 \\ a_3 & 0 & -a_1 \\ -a_2 & a_1 & 0 \end{bmatrix}. \quad (3.34)$$

The function $\exp(\cdot)$ is the matrix exponential function, which is given by

$$\exp(\mathbf{A}) = \mathbf{I}_N + \mathbf{A} + \frac{1}{2!} \mathbf{A}^2 + \frac{1}{3!} \mathbf{A}^3 + \dots = \sum_{n=0}^{\infty} \frac{1}{n!} \mathbf{A}^n \quad (3.35)$$

where $\mathbf{A} \in \mathbb{R}^{N \times N}$ is a square matrix. Note that equation (3.33) is a function mapping from $SO(3)$ to $\mathbb{R}^{3 \times 1}$.

The update step for the optimization on $SO(3)$ is given by [46, eq. (7.179)]

$$\mathbf{R}^{t+1} = \exp\left(\left(\alpha \nabla_{\mathbf{R}} \big|_{\mathbf{R}^t} f\right)^\wedge\right) \mathbf{R}^t, \quad (3.36)$$

where α is the step size, and $\exp(\cdot)$ maps $(\alpha \nabla_{\mathbf{R}} \big|_{\mathbf{R}^t} f)^\wedge$ – an element in $\mathfrak{so}(3)$ – back into $\exp\left((\alpha \nabla_{\mathbf{R}} \big|_{\mathbf{R}^t} f)^\wedge\right)$ – an element in $SO(3)$ ⁵.

There is also an inherent physical meaning for the concepts introduced above. According to Euler's rotation theorem [50], a rotation matrix \mathbf{R} can be expressed as

$$\mathbf{R}_{\mathbf{u}} = \exp(\mathbf{u}^\wedge) \quad (3.37)$$

where, physically, $\mathbf{u} \in \mathbb{R}^{3 \times 1}$ is the axis-angle representation of $\mathbf{R}_{\mathbf{u}}$, and, consequently, $\mathbf{R}_{\mathbf{u}}$ realizes the rotation that rotates the rigid object around the unit axis of $\mathbf{u}/\|\mathbf{u}\|$ by an angle $\|\mathbf{u}\|$. Equation (3.37) is equivalent to Rodrigues' rotation formula

$$\mathbf{R}_{\mathbf{u}} = \mathbf{I}_3 + \left(\frac{\sin \|\mathbf{u}\|}{\|\mathbf{u}\|}\right) \mathbf{u}^\wedge + \left(\frac{1 - \cos \|\mathbf{u}\|}{\|\mathbf{u}\|^2}\right) (\mathbf{u}^\wedge)^2 \quad (3.38)$$

given in [45, p. 50].

⁵A valid mapping R from the tangent space $T\mathcal{M}$ to the manifold \mathcal{M} , i.e., $R: T\mathcal{M} \mapsto \mathcal{M}$, is called a retraction on a manifold \mathcal{M} , which has to satisfy several particular properties (please refer to the Definition 3.41 in [45, p. 46] for the formal definition). For Lie groups, one valid retraction is the Lie exponential map given by the matrix exponential function [45, p. 152], which is intensively used in the robotic society [47, 48, 49].

that converts the axis-angle representation to the rotation matrix representation. Since the rotation vector \mathbf{u} is physically the axis-angle presentation of the rotation matrix $\mathbf{R}_{\mathbf{u}}$, we can calculate \mathbf{u} from $\mathbf{R}_{\mathbf{u}}$ conveniently by

$$\|\mathbf{u}\| = \arccos\left(\frac{\text{tr}(\mathbf{R}_{\mathbf{u}}) - 1}{2}\right) \quad (3.39)$$

and

$$\mathbf{u} = \frac{\|\mathbf{u}\|}{2 \sin \|\mathbf{u}\|} \begin{bmatrix} [\mathbf{R}_{\mathbf{u}}]_{3,2} - [\mathbf{R}_{\mathbf{u}}]_{2,3} \\ [\mathbf{R}_{\mathbf{u}}]_{1,3} - [\mathbf{R}_{\mathbf{u}}]_{3,1} \\ [\mathbf{R}_{\mathbf{u}}]_{2,1} - [\mathbf{R}_{\mathbf{u}}]_{1,2} \end{bmatrix}. \quad (3.40)$$

Now, we can define the distance of two rotation matrices $\mathbf{R}_1, \mathbf{R}_2 \in SO(3)$ as the rotation vector \mathbf{u}_d associated with the residual rotation matrix \mathbf{R}_d that physically measures how much \mathbf{R}_2 must rotate to reach \mathbf{R}_1 , namely

$$\mathbf{R}_d = \mathbf{R}_1 \mathbf{R}_2^T \in SO(3). \quad (3.41)$$

Mathematically, \mathbf{u}_d is the vector associated with \mathfrak{so} , i.e., $\mathbf{u}_d = \log(\mathbf{R}_d)^\vee$, where the matrix logarithmic function $\log(\cdot)$ maps from $SO(3)$ into $\mathfrak{so}(3)$, the operator of \cdot^\vee converts $\mathbf{a}^\wedge \in \mathfrak{so}(3)$ into the vector \mathbf{a} , i.e the inverse operator of \cdot^\wedge .

Previously, we considered the gradient of a function $f(\mathbf{R})$ with respect to \mathbf{R} . To obtain the gradient of $f(\mathbf{T})$ with respect to $\mathbf{T} \in SE(3)$, a similar approach is used. The gradient is calculated by introducing an infinitesimal perturbation $\exp(\boldsymbol{\xi}^\wedge)$ as [46, eq. (7.191)]

$$\begin{aligned} \nabla_{\mathbf{T}} f(\mathbf{T}) &= \left. \frac{\partial}{\partial \boldsymbol{\xi}} \right|_{\boldsymbol{\xi}=\mathbf{0}} f(\exp(\boldsymbol{\xi}^\wedge) \mathbf{T}) \\ &\triangleq \begin{bmatrix} \left. \frac{d}{dt} \right|_{t=0} f(\exp(te_1^\wedge) \mathbf{T}) \\ \vdots \\ \left. \frac{d}{dt} \right|_{t=0} f(\exp(te_6^\wedge) \mathbf{T}) \end{bmatrix}, \end{aligned} \quad (3.42)$$

where the operator \cdot^\wedge converts a 6×1 vector into the Lie algebra $\mathfrak{se}(3)$ of $SE(3)$, which is,

$$\left([\mathbf{a}^T, \mathbf{b}^T]^T \right)^\wedge = \begin{bmatrix} \mathbf{b}^\wedge \mathbf{a} \\ \mathbf{0}^T 0 \end{bmatrix} \in \mathbb{R}^{4 \times 4}, \quad \mathbf{a}, \mathbf{b} \in \mathbb{R}^{3 \times 1}. \quad (3.43)$$

3.2.3 Distribution on $SO(3)$

In some cases, it is necessary to associate uncertainty with the rotation by specifying an appropriate distribution on $SO(3)$. There are various ways to parameterize distribution on $SO(3)$ [51]. Different PDFs have been proposed in the literature, for example, the von Mises-Fisher distribution and the tangent defined distribution. However, the von Mises-Fisher distribution has two drawbacks [52]: (1) it is isotropic and cannot specify the dominant dimension

(e.g., yaw of the vehicle during travel), and (2) estimating the concentration parameter is usually very difficult [53]. Instead, parameterizing uncertainty over $SO(3)$ by injecting uncertainty onto the manifold [54,55] from a local tangent space about some mean element is easier to parameterize. Therefore, in this thesis, we will use the later method.

For a given $p(\mathbf{u})$ for the rotation vector \mathbf{u} , the induced distribution of \mathbf{R} such that $\mathbf{R} = \exp(\mathbf{u}^\wedge)\bar{\mathbf{R}}$ is obtained using change of variables as [46, eq. (7.109)]

$$p(\mathbf{R}|\bar{\mathbf{R}}) = p(\mathbf{u})|\det(\mathbf{J}(\mathbf{u}))| \quad (3.44)$$

based on the differential of [46, eq. (7.107)]

$$d\mathbf{R} = |\det(\mathbf{J}(\mathbf{u}))|d\mathbf{u} \quad (3.45)$$

where [46, eqs. (7.108) and (7.76b)]

$$|\det(\mathbf{J}(\mathbf{u}))| = \frac{2(1 - \cos\|\mathbf{u}\|)}{\|\mathbf{u}\|^2} \quad (3.46)$$

and

$$\mathbf{J}(\mathbf{u})^{-1} = \frac{\|\mathbf{u}\|}{2} \cot \frac{\|\mathbf{u}\|}{2} \mathbf{I}_3 + \left(1 - \frac{\|\mathbf{u}\|}{2} \cot \frac{\|\mathbf{u}\|}{2}\right) \frac{\mathbf{u}\mathbf{u}^\top}{\|\mathbf{u}\|^2} - \frac{\mathbf{u}^\wedge}{2} \quad (3.47)$$

In (3.47), the function $\mathbf{J}(\mathbf{u})^{-1} : \mathbb{R}^{3 \times 1} \mapsto \mathbb{R}^{3 \times 1}$ gives the gradient of \mathbf{u} with respect to \mathbf{R} [46, eq. (7.104b)].

3.2.4 The Intrinsic CRB on $SO(3)$

When the parameter to be estimated belongs to a manifold, the MSE can be expressed in terms of the geodesic distance on the manifold⁶. In such a case, the corresponding CRB is termed as the intrinsic CRB (ICRB) [56].

As the parameter \mathbf{R} belongs to the manifold $SO(3)$, the residual error between the estimated and true parameters can be expressed by $\mathbf{u}_e = \log(\mathbf{R}\hat{\mathbf{R}}^\top)^\vee$ and the corresponding MSE is expressed as [58, eq. (1)]

$$\text{MSE}(\Theta) = E_{\mathbf{y}}\{\mathbf{u}_e\mathbf{u}_e^\top\}. \quad (3.48)$$

Then the ICRB on $SO(3)$ is defined by [58] $\text{ICRB} = \mathbf{J}_I^{-1} + \mathbf{C}_I$, where \mathbf{J}_I is the intrinsic Fisher information matrix (IFIM), and \mathbf{C}_I is the curvature term and it is generally neglected for small errors [58,59]. The IFIM is defined as [58, eq. (2)] the matrix \mathbf{J}_I such that for any $\boldsymbol{\zeta}, \boldsymbol{\xi} \in \mathbb{R}^{3 \times 1}$

$$\boldsymbol{\xi}^\top \mathbf{J}_I \boldsymbol{\xi}$$

⁶If the MSE is expressed in terms of distances in the embedding Euclidean space, the constrained CRB can also be used. But it is stated that [56] the constrained CRB is less natural than the intrinsic CRB. In addition, as stated in a recent work [57], the constrained and the intrinsic CRBs are potentially relevant and deserve further investigation. However, to the best of the author's knowledge, there is currently no other work on the connection between these two bounds.

$$= \int \left(\frac{d}{dt} \Big|_{t=0} \ln p(\mathbf{y} | \exp(t\boldsymbol{\xi}^\wedge) \mathbf{R}) \right) \left(\frac{d}{dt} \Big|_{t=0} \ln p(\mathbf{y} | \exp(t\boldsymbol{\zeta}^\wedge) \mathbf{R}) \right) p(\mathbf{y} | \mathbf{R}) d\mathbf{y} \quad (3.49)$$

and

$$\boldsymbol{\xi}^T \mathbf{J} \boldsymbol{\zeta} = \frac{1}{2} \left((\boldsymbol{\xi} + \boldsymbol{\zeta})^T \mathbf{J} (\boldsymbol{\xi} + \boldsymbol{\zeta}) - \boldsymbol{\xi}^T \mathbf{J}_I \boldsymbol{\xi} - \boldsymbol{\zeta}^T \mathbf{J}_I \boldsymbol{\zeta} \right) \quad (3.50)$$

are satisfied.

The IFIM can be calculated in a more compact form by noticing that for a scale function f defined on \mathbf{R} , i.e., $f : \mathbf{R} \in SO(3) \mapsto f(\mathbf{R}) \in \mathbb{R}$,

$$\frac{d}{dt} \Big|_{t=0} f(\exp(t\boldsymbol{\xi}^\wedge) \mathbf{R}) = f_{\mathbf{R}} \boldsymbol{\xi}^\wedge \mathbf{R} \quad (3.51)$$

where $[f_{\mathbf{R}}]_{i,j} = \frac{\partial f}{\partial [\mathbf{R}]_{i,j}}$. Then we have

$$\frac{d}{dt} \Big|_{t=0} f(\exp(t(\boldsymbol{\xi} + \boldsymbol{\zeta})^\wedge) \mathbf{R}) = \frac{d}{dt} \Big|_{t=0} f(\exp(t\boldsymbol{\xi}^\wedge) \mathbf{R}) + \frac{d}{dt} \Big|_{t=0} f(\exp(t\boldsymbol{\zeta}^\wedge) \mathbf{R}) \quad (3.52)$$

and thus

$$\begin{aligned} & \boldsymbol{\xi}^T \mathbf{J}_I \boldsymbol{\zeta} \\ &= \int \left(\frac{d}{dt} \Big|_{t=0} \ln p(\mathbf{y} | \exp(t\boldsymbol{\xi}^\wedge) \mathbf{R}) \right) \left(\frac{d}{dt} \Big|_{t=0} \ln p(\mathbf{y} | \exp(t\boldsymbol{\zeta}^\wedge) \mathbf{R}) \right) p(\mathbf{y} | \mathbf{R}) d\mathbf{y} \end{aligned} \quad (3.53)$$

Further recalling the calculation (3.33) of the gradient for a scale function f and taking into account that $[\mathbf{J}_I]_{i,j} = \mathbf{e}_i^T \mathbf{J}_I \mathbf{e}_j$, it can be seen that the IFIM can be calculated by

$$\mathbf{J}_I = \int (\nabla_{\mathbf{R}} \ln p(\mathbf{y} | \mathbf{R})) (\nabla_{\mathbf{R}}^T \ln p(\mathbf{y} | \mathbf{R})) p(\mathbf{y} | \mathbf{R}) d\mathbf{y}. \quad (3.54)$$

It can be seen that the IFIM can be calculated in a "classical" way when the gradient is calculated by (3.33).

3.3 Conclusion

In this chapter we briefly introduce some topics from the estimation theory and basics on $SO(3)/SE(3)$, which will come in handy in subsequent chapters.

The estimation theory will be used to find the objective function for position and orientation estimation. Some well known estimators dedicated for different conditions of prior information (including LS, ML, MAP and HMM) are reviewed. The measure of MSE for evaluating an estimator's performance is introduced, with emphasis on the corresponding theoretical lower bound which gives the minimum achievable MSE.

The remainder of this chapter focuses on the basics of $SO(3)/SE(3)$, with emphasis on the principle of optimization on $SO(3)/SE(3)$. When the closed form solution to the objective function is not easy to obtain, a numerical optimization method has to be adopted. The principle of optimization on $SO(3)/SE(3)$ provides a simple but robust method to deal with the constraints imposed by the properties of rotation matrix. In addition, this section also introduces the concepts of distribution on $SO(3)$ and intrinsic CRB on $SO(3)$, which will be used in the following.

4

Simultaneous Position and Orientation Estimation for the Angular Diversity Receiver

In this chapter, we investigate the simultaneous position and orientation estimation (SPO) problem using received signal strength (RSS), for the angular diversity receiver without an external orientation estimation device. Due to the constraints imposed by the rotation matrix as mentioned in Section 3.2.2, in this chapter, we design two SPO algorithms using the principle of optimization on manifolds, which alleviates the constraints from the rotation matrix. In addition, we propose an initialization algorithm, based on the direct linear transformation (DLT) principle, to obtain an initial estimate in closed-form for the iterative algorithms. To evaluate the performance of the proposed RSS-based SPO algorithms, we derive the Cramér-Rao bound (CRB). Finally, computer simulations show an asymptotic tightness between the performance of the proposed algorithms and the theoretical lower bound, demonstrating the effectiveness of the proposed solutions.

4.1 Problem Statement

We consider a system containing N_L LEDs and a VLP receiver containing N_P bare PDs, as shown in Fig. 2.7. Let us define the $N_L N_P \times 1$ vector $\mathbf{y} = [\mathbf{y}_1^T, \dots, \mathbf{y}_{N_P}^T]^T$ as the vector of observations, with $\mathbf{y}_j = [y_{1,j}, \dots, y_{N_L,j}]^T$. Assuming the LOS component dominates the received signal, we obtain

$$\mathbf{y} = \mathbf{g} + \mathbf{w}, \quad (4.1)$$

where the $N_L N_P \times 1$ vector \mathbf{g} is defined as $\mathbf{g} = [\mathbf{g}_1^T, \dots, \mathbf{g}_{N_P}^T]^T$ with $\mathbf{g}_j = R_{p,j} [P_{t,1} h_{1,j}, \dots, P_{t,N_L} h_{N_L,j}]^T$, $h_{i,j}$ is given in (2.17), $P_{t,i}$ is the power trans-

mitted by the i^{th} LED and $R_{p,j}$ is the responsivity of the j^{th} PD. The $N_L N_P \times 1$ vector \mathbf{w} models the noise, which is represented by a zero-mean multivariate Gaussian random variable with covariance matrix $\Sigma_{\mathbf{w}} = \sigma_w^2 \mathbf{I}_{N_L N_P}$. Based on the observation (4.1) the SPO algorithm needs to jointly estimate the position \mathbf{r} and the orientation \mathbf{R} .

Let us define the wanted parameter set $\Theta = \{\mathbf{r}, \mathbf{R}\}$ and define the log-likelihood function as

$$\begin{aligned} \mathcal{L}(\Theta; \mathbf{y}) &= \ln p(\mathbf{y}|\Theta) \\ &= \text{const} - \frac{1}{2} \|\mathbf{y} - \mathbf{g}\|_{\Sigma_{\mathbf{w}}}^2, \end{aligned} \tag{4.2}$$

where $\|\mathbf{x}\|_{\Sigma}^2 = \mathbf{x}^T \Sigma^{-1} \mathbf{x}$ denotes the squared Mahalanobis distance with respect to covariance Σ , and $p(\mathbf{y}|\Theta)$ is the conditional probability density function of \mathbf{y} given Θ , which complies with $\mathbf{y}|\Theta \sim \mathcal{N}(\mathbf{g}(\Theta), \Sigma_{\mathbf{w}})$. The maximum likelihood (ML) estimate of Θ , i.e. $\hat{\Theta} = \{\hat{\mathbf{r}}, \hat{\mathbf{R}}\}$, maximizes the log-likelihood function \mathcal{L} :

$$\hat{\Theta} = \underset{\Theta}{\text{arg max}} \mathcal{L}. \tag{4.3}$$

As (4.3) is a non-linear least squares (NLS) problem, it has no closed-form solution, implying it has to be solved using an iterative optimization algorithm. Even worse, since \mathbf{R} is a member of $SO(3)$ rather than an arbitrary 3×3 real matrix, \mathbf{R} has to satisfy the following constraints:

$$\mathbf{R}^T \mathbf{R} = \mathbf{R} \mathbf{R}^T = \mathbf{I}, \quad \det(\mathbf{R}) = +1. \tag{4.4}$$

To solve (4.3) constrained by (4.4), we can resort to a constrained non-linear optimization algorithm, which is complex, time consuming and non-robust. However, since $SO(3)$ is an embedded submanifold of $\mathbb{R}^{3 \times 3}$, we can estimate the parameters in $SO(3)$ using an (iterative) optimization algorithm on manifolds [44]. In Subsection 4.2.1, we adapt Newton's method on $SO(3)$ from [60] to solve the problem at hand, while the interior point method on $SO(3)$ is discussed in Subsection 4.2.2.

4.2 Estimation Algorithms

In the previous section, we showed that the SPO problem is a constrained non-linear least squares problem (constrained by the rotation matrix) that can be solved by standard optimization algorithms. However, the resulting algorithms are complex and non-robust. In this section, we first consider the Gauss-Newton method on manifolds. Its counterpart, i.e. standard Gauss-Newton, is an iterative method that is regularly used for solving non-linear least squares problems. However, the Gauss-Newton method does not always converge properly. Therefore, in order to achieve a proper convergence, we propose an interior point method on manifolds that additionally considers the boundary condition, i.e. the constraint imposed on the position vector. This

algorithm is an extension of the standard interior method, which is an effective method to solve non-linear optimization problems that contain an inequality constraint.

4.2.1 Gauss-Newton Method on Manifolds

As in the standard Gauss-Newton optimization, the first step is to find the steepest descent direction to determine the search direction. This search direction $\Delta_{\Theta} = [\Delta_{\mathbf{r}}^T, \Delta_{\mathbf{R}}^T]^T$ is given by

$$\Delta_{\Theta} = -(\nabla_{\Theta} \mathbf{g})^{\dagger} (\mathbf{g} - \mathbf{y}), \quad (4.5)$$

where $(\cdot)^{\dagger}$ denotes the Moore-Penrose pseudoinverse, $\nabla_{\Theta} \mathbf{g} = [\nabla_{\Theta} \mathbf{g}_1, \dots, \nabla_{\Theta} \mathbf{g}_{N_P}]^T \in \mathbb{R}^{N_L N_P \times 6}$ denotes the Jacobian matrix of \mathbf{g} with respect to Θ , with $\nabla_{\Theta} \mathbf{g}_j = R_{p,j} [P_{t,1} \nabla_{\Theta} h_{1,j}, \dots, P_{t,N_L} \nabla_{\Theta} h_{N_L,j}]^T \in \mathbb{R}^{N_L \times 6}$, and $\nabla_{\Theta} h_{i,j} = \left[\left(\frac{\partial h_{i,j}}{\partial \mathbf{r}} \right)^T, \left(\frac{\partial h_{i,j}}{\partial \mathbf{R}} \right)^T \right] \in \mathbb{R}^{1 \times 6}$. The partial derivative $\frac{\partial h_{i,j}}{\partial \mathbf{r}}$ is calculated in Euclidean space, while $\frac{\partial h_{i,j}}{\partial \mathbf{R}}$ is calculated by introducing an infinitesimal perturbation $\exp(\omega^{\wedge})$ as follows (see (3.33)),

$$\frac{\partial h_{i,j}}{\partial \mathbf{R}} = \frac{\partial}{\partial \omega} \Big|_{\omega=0} \left\{ K_{i,j} \frac{(\mathbf{n}_{L,i}^T (\mathbf{v}_i + \exp(\omega^{\wedge}) \mathbf{R} \mathbf{d}_{j,r}))^{\gamma}}{\|\mathbf{v}_i + \exp(\omega^{\wedge}) \mathbf{R} \mathbf{d}_{j,r}\|^{\gamma+3}} \cdot (\exp(\omega^{\wedge}) \mathbf{R} \mathbf{R}_{P,j} \mathbf{n}_0)^T (\mathbf{v}_i + \exp(\omega^{\wedge}) \mathbf{R} \mathbf{d}_{j,r}) \right\}, \quad (4.6)$$

where the infinitesimal perturbation $\exp(\omega^{\wedge}) \in SO(3)$ is expressed as

$$\exp(\omega^{\wedge}) = \exp \begin{pmatrix} 0 & -\omega_z & \omega_y \\ \omega_z & 0 & -\omega_x \\ -\omega_y & \omega_x & 0 \end{pmatrix}, \quad (4.7)$$

the operator $(\cdot)^{\wedge}$ converts the rotation vector $\omega = [\omega_x \ \omega_y \ \omega_z]^T$ into a skew-symmetric matrix $\omega^{\wedge} \in \mathfrak{so}(3)$, and $\exp(\cdot)$ is the matrix exponential function. Equation (4.6) can be calculated by

$$\frac{\partial h_{i,j}}{\partial \mathbf{R}} = \frac{\partial h_{i,j}}{\partial \mathbf{v}_{i,j}} \frac{\partial \mathbf{v}_{i,j}}{\partial \mathbf{R}} + \frac{\partial h_{i,j}}{\partial \mathbf{n}_{P,j}} \frac{\partial \mathbf{n}_{P,j}}{\partial \mathbf{R}} \quad (4.8)$$

where

$$\frac{\partial h_{i,j}}{\partial \mathbf{v}_{i,j}} = K_{i,j} \left\{ \frac{\gamma (\mathbf{n}_{L,i}^T \mathbf{v}_{i,j})^{\gamma-1} (\mathbf{n}_{P,j}^T \mathbf{v}_{i,j})}{\|\mathbf{v}_{i,j}\|^{\gamma+3}} \mathbf{n}_{L,i}^T + \frac{(\mathbf{n}_{L,i}^T \mathbf{v}_{i,j})^{\gamma}}{\|\mathbf{v}_{i,j}\|^{\gamma+3}} \mathbf{n}_{P,j}^T - \frac{(\gamma+3) (\mathbf{n}_{L,i}^T \mathbf{v}_{i,j})^{\gamma} (\mathbf{n}_{P,j}^T \mathbf{v}_{i,j})}{\|\mathbf{v}_{i,j}\|^{\gamma+5}} \mathbf{v}_{i,j}^T \right\}, \quad (4.9)$$

$$\frac{\partial h_{i,j}}{\partial \mathbf{n}_{P,j}} = K_{i,j} \frac{(\mathbf{n}_{L,i}^T \mathbf{v}_{i,j})^\gamma (\mathbf{n}_{P,j}^T \mathbf{v}_{i,j})}{\|\mathbf{v}_{i,j}\|^{\gamma+3}} \mathbf{v}_{i,j}^T, \quad (4.10)$$

$$\begin{aligned} \frac{\partial \mathbf{n}_{P,j}}{\partial \mathbf{R}} &= \frac{\partial (\mathbf{R} \mathbf{n}_{P,j,r})}{\partial \mathbf{R}} = \frac{\partial}{\partial \boldsymbol{\omega}} \Big|_{\boldsymbol{\omega}=0} (\exp(\boldsymbol{\omega}^\wedge) \mathbf{R} \mathbf{n}_{P,j,r}) \\ &= -(\mathbf{R} \mathbf{n}_{P,j,r})^\wedge \end{aligned} \quad (4.11a)$$

$$= (\mathbf{n}_{P,j}^\wedge)^T, \quad (4.11b)$$

$$\begin{aligned} \frac{\partial \mathbf{v}_{i,j}}{\partial \mathbf{R}} &= \frac{\partial (\mathbf{R} \mathbf{d}_{j,r})}{\partial \mathbf{R}} = \frac{\partial}{\partial \boldsymbol{\omega}} \Big|_{\boldsymbol{\omega}=0} (\exp(\boldsymbol{\omega}^\wedge) \mathbf{R} \mathbf{d}_{j,r}) \\ &= -(\mathbf{R} \mathbf{d}_{j,r})^\wedge \end{aligned} \quad (4.12a)$$

$$= (\mathbf{d}_j^\wedge)^T. \quad (4.12b)$$

The equalities (4.11a) and (4.12a) hold because of [46, eq. (7.174)]. Further utilizing the equalities $\mathbf{x}^\wedge \mathbf{y} = -\mathbf{y}^\wedge \mathbf{x}$, $\mathbf{x}^\wedge \mathbf{x} = \mathbf{0}$, for $\mathbf{x}, \mathbf{y} \in \mathbb{R}^{3 \times 1}$, and $\frac{\partial h_{i,j}}{\partial \mathbf{r}} = \frac{\partial h_{i,j}}{\partial \mathbf{v}_{i,j}}$, the partial differential vector of $h_{i,j}$ is then given by

$$\begin{aligned} \nabla_{\Theta} h_{i,j} &= K_{i,j} \cdot \\ &\begin{bmatrix} \frac{\gamma (\mathbf{n}_{L,i}^T \mathbf{v}_{i,j})^{\gamma-1} (\mathbf{n}_{P,j}^T \mathbf{v}_{i,j})}{\|\mathbf{v}_{i,j}\|^{\gamma+3}} \\ \frac{(\mathbf{n}_{L,i}^T \mathbf{v}_{i,j})^\gamma}{\|\mathbf{v}_{i,j}\|^{\gamma+3}} \\ -\frac{(\gamma+3) (\mathbf{n}_{L,i}^T \mathbf{v}_{i,j})^\gamma (\mathbf{n}_{P,j}^T \mathbf{v}_{i,j})}{\|\mathbf{v}_{i,j}\|^{\gamma+5}} \end{bmatrix}^T \cdot \begin{bmatrix} \mathbf{n}_{L,i}^T, & \mathbf{n}_{L,i}^T \cdot (\mathbf{d}_j^\wedge)^T \\ \mathbf{n}_{P,j}^T, & \boldsymbol{\nu}_i^T \cdot (\mathbf{n}^\wedge)^T \\ \mathbf{v}_{i,j}^T, & \boldsymbol{\nu}_i^T \cdot (\mathbf{d}_j^\wedge)^T \end{bmatrix}. \end{aligned} \quad (4.13)$$

In contrast to the standard Gauss-Newton algorithm, the update step for the algorithm on manifolds is given by

$$\mathbf{r}^{t+1} = \mathbf{r}^t + \alpha \boldsymbol{\Delta}_{\mathbf{r}}, \quad \mathbf{R}^{t+1} = \exp((\alpha \boldsymbol{\Delta}_{\mathbf{R}})^\wedge) \mathbf{R}^t, \quad (4.14)$$

where α is the step size, and $\exp(\cdot)$ maps $(\alpha \boldsymbol{\Delta}_{\mathbf{R}})^\wedge$ – an element in $\mathfrak{so}(3)$ – back into $\exp((\alpha \boldsymbol{\Delta}_{\mathbf{R}})^\wedge)$ – an element in $SO(3)$.

4.2.2 Interior Point Method on Manifolds

In our experiments, we found that the Gauss-Newton algorithm not always converges properly, especially when the SNR is low or the number of observations is small. In these situations, it often happens that a position is found that is outside of the room with the LEDs and receiver. To avoid such outliers and improve the convergence of the algorithm, in the following we design an interior point method on manifolds that takes into account a boundary condition, i.e. the position of the receiver is confined within a target area (the

room), which is expressed as $\mathbf{0} \leq \mathbf{r} \leq \mathbf{b}$, where the position \mathbf{r} of the receiver is confined within the bounds of the room given by the coordinates $\mathbf{0}$ and \mathbf{b} . As the bounds $\mathbf{0} \leq \mathbf{r} \leq \mathbf{b}$ are hard to implement in a practical optimization algorithm, due to the discontinuity of the equality sign, the interior point method replaces the strict inequality by a barrier function $-\mu \sum_{i=1}^6 \ln([\mathbf{s}]_i)$, where \mathbf{s} is a slack variable vector and μ is the barrier parameter, and $[\cdot]_i$ is defined as the operator that returns the i^{th} element when the operand is a vector and it returns the i^{th} row as a row vector when the operand is a matrix. Forcing \mathbf{s} to be strictly positive is equivalent to $\mathbf{0} \leq \mathbf{r} \leq \mathbf{b}$. This barrier function is added as a penalty function to our objective function (4.3) to enforce the boundary condition:

$$\hat{\Theta} = \arg \min_{\Theta} \left\{ -\mathcal{L} - \mu \sum_{i=1}^6 \ln([\mathbf{s}]_i) \right\}, \quad (4.15)$$

s.t. $\mathbf{c} - \mathbf{s} = \mathbf{0}$

where $\mathbf{c}^T = [\mathbf{r}^T, (\mathbf{b} - \mathbf{r})^T]$ is the rearranged inequality vector. The interior point method consists of finding (approximate) solutions of (4.15) for a sequence of positive $\{\mu\}$ that converges to zero. In the first steps, the barrier parameter μ is taken strictly positive to keep the algorithm within the feasible region, whereas in later steps, the barrier parameter converges to zero to better resemble the condition $\mathbf{0} \leq \mathbf{r} \leq \mathbf{b}$. For each μ , the interior point method finds the solution to the Karush-Kuhn-Tucker (KKT) conditions for (4.15) using Newton's method. As such, the interior point method is a two-level iteration algorithm, where the outer iteration decays μ gradually and the inner iteration updates iteratively the state (comprised of the parameter set Θ , the Lagrange multiplier \mathbf{z} of \mathbf{c} , and the slack variable vector \mathbf{s}) for a given μ . To determine the search direction $(\Delta_{\Theta}, \Delta_{\mathbf{z}}, \Delta_{\mathbf{s}})$ for the inner iteration, the algorithm finds the solution to the symmetric primal-dual system [61, eq. (19.12)], which is given by

$$\begin{bmatrix} -\Delta_{\Theta}^{\Theta} \mathcal{L}(\Theta) & \mathbf{A}^T \\ \mathbf{A} & -\mathbf{Z}^{-1} \mathbf{S} \end{bmatrix} \begin{bmatrix} \Delta_{\Theta} \\ -\Delta_{\mathbf{z}} \end{bmatrix} = \begin{bmatrix} \mathbf{A}^T \mathbf{z} + \nabla_{\Theta} \mathcal{L}(\Theta) \\ \mu \mathbf{Z}^{-1} \mathbf{1} - \mathbf{c} \end{bmatrix}, \quad (4.16a)$$

$$\Delta_{\mathbf{s}} = \mathbf{Z}^{-1} (\mu \mathbf{1} - \mathbf{Z} \mathbf{s} - \mathbf{S} \Delta_{\mathbf{z}}), \quad (4.16b)$$

where $\mathbf{1}$ is the all-ones vector, the diagonal matrices \mathbf{Z} and \mathbf{S} are given by $\mathbf{Z} = \text{diag}(\mathbf{z})$, $\mathbf{S} = \text{diag}(\mathbf{s})$, respectively, and

$$\mathbf{A} = \begin{bmatrix} \mathbf{I}_{3 \times 3} & \mathbf{0}_{3 \times 3} \\ -\mathbf{I}_{3 \times 3} & \mathbf{0}_{3 \times 3} \end{bmatrix} \quad (4.17)$$

is the Jacobian matrix of \mathbf{c} with respect to Θ . Since in the Hessian matrix in (4.16a), the analytical derivation of $\Delta_{\Theta}^{\Theta} \mathcal{L}(\Theta)$ is cumbersome, in the following it is approximated by $\Delta_{\Theta}^{\Theta} \mathcal{L}(\Theta) \approx (\nabla_{\Theta} \mathbf{g})^T (\nabla_{\Theta} \mathbf{g})$. Note that the same expression can be found in the Moore-Penrose pseudoinverse, used in the Gauss-Newton algorithm.

The solution of (4.16) defines the search direction for the inner iteration, while the step length is determined by

$$\alpha_{\mathbf{s}}^{\max} = \max \{ \alpha \in (0, 1] : \mathbf{s} + \alpha \Delta_{\mathbf{s}} \geq (1 - \tau) \mathbf{s}, \alpha \|\Delta_{\mathbf{R}}\| \leq (1 - \tau) \pi \}, \quad (4.18a)$$

$$\alpha_{\mathbf{z}}^{\max} = \max \{ \alpha \in (0, 1] : \mathbf{z} + \alpha \Delta_{\mathbf{z}} \geq (1 - \tau) \mathbf{z} \}. \quad (4.18b)$$

The constraint, $\alpha \|\Delta_{\mathbf{R}}\| \leq (1 - \tau) \pi$, in the formula of $\alpha_{\mathbf{s}}^{\max}$ prevents the absolute value of the incremental step for \mathbf{R} from being larger than π , which arises from the fact that the matrix exponential function that converts the incremental step back in the manifold is a periodic function with a period of 2π . As a result, the update step for the interior point algorithm on manifolds is given by

$$\mathbf{r}^{t+1} = \mathbf{r}^t + \alpha_{\mathbf{s}} \Delta_{\mathbf{r}}, \quad \mathbf{R}^{t+1} = \exp((\alpha_{\mathbf{s}} \Delta_{\mathbf{R}})^{\wedge}) \mathbf{R}^t, \quad (4.19a)$$

$$\mathbf{s}^{t+1} = \mathbf{s}^t + \alpha_{\mathbf{s}} \Delta_{\mathbf{s}}, \quad \mathbf{z}^{t+1} = \mathbf{z}^t + \alpha_{\mathbf{z}} \Delta_{\mathbf{z}}. \quad (4.19b)$$

The merit function measuring the quality of an updated state is given in terms of the barrier function (4.15) by

$$m_{\iota}(\Theta, \mathbf{s}) = -\mathcal{L}(\Theta) - \mu \sum_{i=1}^6 \ln([\mathbf{s}]_i) + \iota \|\mathbf{c} - \mathbf{s}\|_1, \quad (4.20)$$

where ι is the penalty parameter that determines the weight that we assign to constraint satisfaction relative to the minimization of the objective. The error function (reflecting the maximum residual error in the KKT conditions), which indicates whether a local minimum solution is achieved, is calculated by [61]

$$\epsilon = \max \{ \|\nabla_{\Theta} \mathcal{L}(\Theta) + \mathbf{A}^T \mathbf{z}\|, \|\mathbf{S} \mathbf{z} - \mu \mathbf{1}\|, \|\mathbf{c} - \mathbf{s}\| \}. \quad (4.21)$$

An overview of the proposed interior point method on the $SO(3)$ manifold is shown in Algorithm 4.1, where ϵ_{TOL} is the tolerance that specifies the required accuracy of the computed solution, μ is initialized by a large positive number and decreases iteratively with a decay rate of σ , and τ could be set to a typical value of $\tau = 0.995$ [61].

4.2.3 Convergence and Complexity Analysis

Besides the performance of the proposed methods, which will be discussed in Section 4.4, we also want to discuss the convergence and complexity of the algorithms. First we discuss the convergence. In the Gauss-Newton method, the convergence is determined by the properties of the Jacobian matrix $\nabla_{\Theta} \mathbf{g}$. Assuming the dimension of the observation vector is not less than the number of unknown parameters, the Jacobian matrix is full-row-rank, implying $\nabla_{\Theta} \mathbf{g}$ is invertible. Further, since $((\nabla_{\Theta} \mathcal{L})^T \cdot \Delta_{\Theta}) < 0$ holds for any non-critical point, the sequence $\{\Delta_{\Theta}\}$ of incremental steps towards the optimal Θ is a gradient-related sequence, whose accumulation point Δ_{Θ}° is a critical point according to

Algorithm 4.1 Algorithm for IPM on the $SO(3)$ manifold

Input: $\mathbf{0} \leq \mathbf{r}^0 \leq \mathbf{b}$, $\mathbf{R}^0 \in SO(3)$
Output: Θ
Initialization : Select $\mu > 0, \tau \in (0, 1), \sigma \in (0, 1), \epsilon_{\text{TOL}}$, set $t = 0$

 1: Compute $\mathbf{z}^0, \mathbf{s}^0$
LOOP Process

 2: **for** $i = 1$ to maxiterations_o **do**

 3: **for** $j = 1$ to maxiterations_i **do**

 4: Compute $\Delta_{\Theta}, \Delta_{\mathbf{z}}, \Delta_{\mathbf{s}}$ from (4.16)

 5: Compute $\alpha_{\mathbf{s}}^{\max}, \alpha_{\mathbf{z}}^{\max}$ using (4.18)

 6: Compute $\alpha_{\mathbf{s}} \in (0, \alpha_{\mathbf{s}}^{\max}], \alpha_{\mathbf{z}} \in (0, \alpha_{\mathbf{z}}^{\max}]$ such that (4.20) decreases

 7: Update $\Theta, \mathbf{s}, \mathbf{z}$ using (4.19)

 8: Compute ϵ from (4.21)

 9: **if** $\epsilon \leq \epsilon_{\text{TOL}}$ **then**

10: break

 11: **end if**

 12: **end for**

 Set $\mu = \sigma\mu$

 13: **end for**

 14: **return** Θ

the convergence of line-search methods. As a consequence, in the neighborhood of Δ_{Θ}^* , the convergence rates of the Gauss-Newton method is superlinear [44]. On the other hand, in the interior point method, the convergence rate is determined by the properties of the Hessian matrix of the objective function in (4.15) and its approximation. In case the difference between the actual and approximated Hessian matrices becomes sufficiently small at the critical point, the optimization in the inner iteration will converge superlinearly [44]. In the situation at hand, the approximated Hessian matrix differs from the actual one by a symmetric matrix that equals zero at the critical point, implying the inner iterations converges superlinearly. By reducing the barrier parameter μ at an appropriate rate [62], the convergence of the combination of inner and outer iterations, i.e., the interior point method as a whole, also is superlinear. Hence, both proposed algorithms will show superlinear convergence rates.

Next, we discuss the complexity. In the Gauss-Newton method, the complexity during each iteration is dominated by the computation of the Moore-Penrose pseudoinverse of $\nabla_{\Theta} \mathbf{g}$, which is a $N_L N_L \times 6$ matrix. As a consequence, the Gauss-Newton method has a complexity of $\mathcal{O}\left((N_L N_P)^2\right)$ flops per iteration [63]. On the other hand, the complexity of the interior point method is dominated by the matrix inversion required to solve (4.16a) in each inner iteration. Therefore, the interior point method has a complexity of $\mathcal{O}\left((N_L N_P)^3\right)$ flops per iteration [63]. Hence, it is clear that the complexity of the interior point method is higher than that of the Gauss-Newton method.

4.2.4 Initial Coarse Estimation

The algorithms given in the previous section are iterative methods, and a proper initialization is required for convergence. To this end, we propose in this section an initialization algorithm. In the following, we assume that all LEDs are installed at the ceiling and an angular diversity receiver is considered. This receiver type, which is considered in several works [35, 36, 37, 38], consists of multiple PDs oriented symmetrically at different directions to achieve a better angular diversity. More specifically, $N_{P,s}$ PDs are placed symmetrically around the center of the receiver, and are tilted away from the center of the receiver, as shown in Fig. 4.1. Let the angle between the normal of the receiver and the normal of a PD be θ_P . Using the axis-angle representation, the normal of the j^{th} PD is specified by $\mathbf{n}_{P,j,r} = \exp((\theta_P \mathbf{z}_{P,j})^\wedge) \mathbf{n}_0$, where $\mathbf{z}_{P,j} = [\cos(j2\pi/N_{P,s}), \sin(j2\pi/N_{P,s}), 0]^\text{T}$. An additional PD placed right above the center of the receiver has normal \mathbf{n}_0 . The relative distance vector $\mathbf{d}_{j,r}$ that specifies the position of j^{th} PD to the center of the receiver is given by $\mathbf{d}_{j,r} = d_j \mathbf{n}_{P,j,r}$, i.e. $\mathbf{d}_{j,r}$ is parallel to $\mathbf{n}_{P,j,r}$. In the following, we will show that the problem of position and orientation estimation can be converted into a plane-based pose estimation problem, by properly selecting a set of points at the ceiling that correspond to the intersections of the normals $\mathbf{n}_{P,j,r}$ on the virtual image plane, i.e., the plane in the frame of the receiver containing all points having amplitude 1 in the z -direction. This plane-based pose estimation problem can easily be solved using the direct linear transformation (DLT) method from computer vision. As in this method, the points at the ceiling must be known, we design a method to estimate these points.

First, let us define two planes: P' denotes the plane of ceiling, while P is the virtual image plane containing the point $\mathbf{q}_j = \mathbf{n}_{P,j,r} / [\mathbf{n}_{P,j,r}]_3^{-1}$. Let \mathbf{q}'_j represent the intersection point of the plane P' with the line starting from the center \mathbf{r} of the receiver and radiating in the direction $\mathbf{n}_{P,j}$. Assuming the intersection points \mathbf{q}'_j are known (the estimation of \mathbf{q}'_j is deferred to the end of this section), then the problem of finding the closed-form SPO solution is converted into a plane-based pose estimation problem² as shown in Fig. 4.2. With at least four $(\mathbf{q}'_j, \mathbf{q}_j)$, the position vector and rotation matrix can be estimated using the direct linear transformation (DLT) method [64], which is a commonly used method for the estimation of the relative pose between a plane and a camera, based on projections of sets of coplanar features in computer

¹Taking into account that the plane P contains all points with $[\mathbf{x}]_3 = 1$, i.e., having amplitude 1 in the z -direction, then \mathbf{q}_j is the intersection point of P with the line starting in O_r and radiating in the direction $\mathbf{n}_{P,j,r}$. Since both \mathbf{q}_j and P are defined in the frame of the receiver, they will move and rotate along with the receiver in a rigid way, i.e. \mathbf{q}_j has a fixed location on P .

²Because \mathbf{q}_j and P move and rotate along with the receiver in a rigid way, \mathbf{q}'_j is actually the projection of \mathbf{q}_j along $\mathbf{n}_{P,j}$ on P' . However, if we switch the roles of these two points (taking \mathbf{q}'_j as the object and \mathbf{q}_j as the projection), \mathbf{q}_j and \mathbf{q}'_j could be viewed as points in a pinhole camera model where the pinhole is positioned at the receiver center \mathbf{r} and has a focus of unit length. "Object" \mathbf{q}'_j (in the frame of the system) is "projected" onto the virtual image plane as \mathbf{q}_j (represented by homogeneous coordinates in the frame of the receiver).

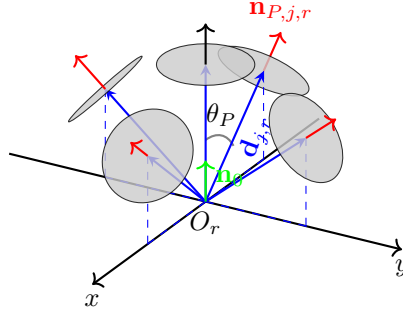


Figure 4.1: Angular diversity receiver with $N_{P,s} = 4$.

vision. The solution of the DLT is given by

$$\begin{cases} \hat{\mathbf{R}} = \begin{bmatrix} \hat{\mathbf{T}}^T \\ [\hat{\mathbf{T}}^T]_1 \times [\hat{\mathbf{T}}^T]_2 \\ 1 \end{bmatrix}, \\ \hat{\mathbf{r}} = -\hat{\mathbf{R}}\mathbf{M} \begin{bmatrix} 0 \\ 0 \\ \lambda \end{bmatrix} + \text{diag}([0, 0, 1]^T) \mathbf{b}, \end{cases} \quad (4.22)$$

where \mathbf{b} is the boundary condition (see Subsection 4.2.2), $\lambda = \frac{\text{tr}(\hat{\mathbf{T}}^T \mathbf{M})}{\text{tr}(\hat{\mathbf{M}}^T \mathbf{M})}$, \mathbf{M} is given by

$$[[\mathbf{M}]_1, [\mathbf{M}]_2, [\mathbf{M}]_3]^T = \mathbf{m}, \quad (4.23)$$

with \mathbf{m} the last column of \mathbf{V}_Q that comes from the Singular Value Decomposition (SVD) of $\mathbf{Q} = \mathbf{U}_Q \mathbf{\Lambda}_Q \mathbf{V}_Q^T$, where the diagonal elements of $\mathbf{\Lambda}_Q$ are arranged in descending order, and the matrix $\mathbf{Q}^T = [\mathbf{Q}_1^T, \dots, \mathbf{Q}_N^T]$, where \mathbf{Q}_i is defined as

$$\mathbf{Q}_i = \begin{bmatrix} \mathbf{0}_{3 \times 1}, & -\mathbf{q}'_i{}^T, & [\mathbf{q}_i]_2 \mathbf{q}'_i{}^T \\ -\mathbf{q}'_i{}^T, & \mathbf{0}_{3 \times 1}, & -[\mathbf{q}_i]_1 \mathbf{q}'_i{}^T \end{bmatrix}. \quad (4.24)$$

The matrix $\hat{\mathbf{T}} \in \mathbb{R}^{3 \times 2}$ in (4.22) is given by $\hat{\mathbf{T}} = \mathbf{U}_T \mathbf{V}_T^T$, where \mathbf{U}_T and \mathbf{V}_T come from the thin SVD of $[[\mathbf{M}]^1, [\mathbf{M}]^2] = \mathbf{U}_T \mathbf{\Lambda}_T \mathbf{V}_T^T$, where the operator $[\cdot]^i$ returns the i^{th} column of a matrix as a column vector. Since the above algorithm does not make any assumption about the visibility of either side of the plane P' , another potential estimate exists, i.e., the mirror symmetry with

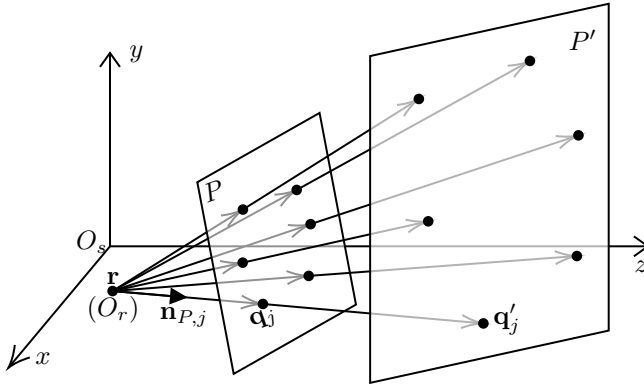


Figure 4.2: Plane-based pose estimation problem. P : the virtual image plane, P' : the plane of the ceiling.

respect to the plane P' , given by

$$\begin{cases} \hat{\mathbf{R}} = \text{diag}([-1, -1, 1]^T) \begin{bmatrix} \hat{\mathbf{T}}^T \\ [\hat{\mathbf{T}}^T]_1 \times [\hat{\mathbf{T}}^T]_2 \end{bmatrix} \\ \hat{\mathbf{r}} = \hat{\mathbf{R}}\mathbf{M} \begin{bmatrix} 0 \\ 0 \\ \lambda \end{bmatrix} + \text{diag}([0, 0, 1]^T) \mathbf{b}. \end{cases} \quad (4.25)$$

From the two possible solutions, the algorithm has to select the solution for which $[\hat{\mathbf{r}}]_3 \leq [\mathbf{b}]_3$, implying that the z coordinate of the estimated position must be smaller than the boundary in the z direction.

The remaining problem is to find a method to estimate the intersection point \mathbf{q}'_j . The idea to achieve this is based on the observation that typically the relative distance between PDs within a PD array is very small compared with the distance between the receiver and LEDs. Hence, for each LED we can select the PD within the array that receives the largest power from this LED. Due to the channel characteristics, this selected PD is, in the absence of noise, the one with the smallest incident angle for that LED. Following the idea above, we could find a set of LEDs, for which the j^{th} PD has the smallest incident angle. The spatial average (weighted by associated received power) of the positions of the LEDs within this set can be seen as an approximation to \mathbf{q}'_j .

A second initial point, $\{\mathbf{b}/2, \mathbf{I}_3\}$ (the receiver pointing upwards and located at the center the area) is also considered in this chapter to ensure that the iterative algorithm converges to the global optimum and to serve as a valid initial point when the DLT algorithm fails, i.e., when less than 4 pairs of $(\mathbf{q}'_j, \mathbf{q}_j)$ are obtained or three out of four of the obtained intersection points \mathbf{q}'_j are collinear [65].

4.3 The Theoretical Lower Bound

We first define the measure of the estimation error in the estimated position and orientation. The estimation error in position is straightforwardly measured by the relative distance between $\hat{\mathbf{r}}$ and \mathbf{r} , i.e. $\mathbf{r}_e = \hat{\mathbf{r}} - \mathbf{r}$, while the estimation error in orientation is measured by the rotation error projected onto the Lie algebra, i.e. $\mathbf{u}_e = \log(\mathbf{R}_e)^\vee$, where the matrix logarithmic function $\log(\cdot)$ maps from $SO(3)$ into $\mathfrak{so}(3)$, and

$$\mathbf{R}_e = \hat{\mathbf{R}}\mathbf{R}^T \in SO(3) \quad (4.26)$$

is the error rotation matrix that physically measures how much $\hat{\mathbf{R}}$ must rotate to reach \mathbf{R} .

Since $\mathbf{y}|\Theta$ is multivariate Gaussian with its covariance being independent of Θ , the associated (classical) Fisher information matrix (FIM) $\mathbf{J}(\Theta)$ can be calculated as [66, eq. (3.31)]:

$$\mathbf{J} = \frac{1}{\sigma_w^2} (\nabla_{\Theta} \mathbf{g})^T (\nabla_{\Theta} \mathbf{g}) \quad (4.27)$$

To get the lower bounds on the error covariance matrices of \mathbf{r}_e and \mathbf{u}_e , respectively, we first rewrite the Fisher information matrix as a partitioned matrix,

$$\mathbf{J}(\Theta) = \begin{bmatrix} \mathbf{J}_{\mathbf{r},\mathbf{r}} & \mathbf{J}_{\mathbf{r},\mathbf{R}} \\ \mathbf{J}_{\mathbf{R},\mathbf{r}} & \mathbf{J}_{\mathbf{R},\mathbf{R}} \end{bmatrix}. \quad (4.28)$$

Consequently,

$$E\{\mathbf{r}_e \mathbf{r}_e^T\} \succeq \left[\mathbf{J}_{\mathbf{r},\mathbf{r}} - \mathbf{J}_{\mathbf{r},\mathbf{R}} \mathbf{J}_{\mathbf{R},\mathbf{R}}^{-1} \mathbf{J}_{\mathbf{R},\mathbf{r}} \right]^{-1}. \quad (4.29)$$

Similarly, the error covariance matrix of \mathbf{u}_e is lower bounded by

$$E\{\mathbf{u}_e \mathbf{u}_e^T\} \succeq \left[\mathbf{J}_{\mathbf{R},\mathbf{R}} - \mathbf{J}_{\mathbf{R},\mathbf{r}} \mathbf{J}_{\mathbf{r},\mathbf{r}}^{-1} \mathbf{J}_{\mathbf{r},\mathbf{R}} \right]^{-1}. \quad (4.30)$$

Taking into account [58], it follows that the orientation bound of (4.30) is actually the intrinsic CRB on $SO(3)$.

4.4 Numerical Results

In the evaluation of the estimator and the theoretical lower bound through computer simulations, we consider an $8 \text{ m} \times 6 \text{ m} \times 3 \text{ m}$ area ($\mathbf{b} = [8, 6, 3]^T$) with $N_L = 24$ LEDs. The LEDs are uniformly distributed over the ceiling, with the number of LEDs in the X direction $N_{L,X} = 6$ and in the Y direction $N_{L,Y} = 4$, i.e., the positions of the LEDs are given by $\left[\frac{[\mathbf{b}]_1(2i-1)}{2N_{L,X}}, \frac{[\mathbf{b}]_2(2j-1)}{2N_{L,Y}}, [\mathbf{b}]_3 \right]^T$, with $i \in \{1, \dots, N_{L,X}\}$ and $j \in \{1, \dots, N_{L,Y}\}$. All LEDs are assumed to have a transmit power of $P_t = 1 \text{ W}$, a Lambertian order $\gamma = 1$, an FOV of $\phi_{FOV} = \pi/2$ rad and point downwards ($\mathbf{n}_{L,i} = [0, 0, -1]^T$). The receiver consists of five

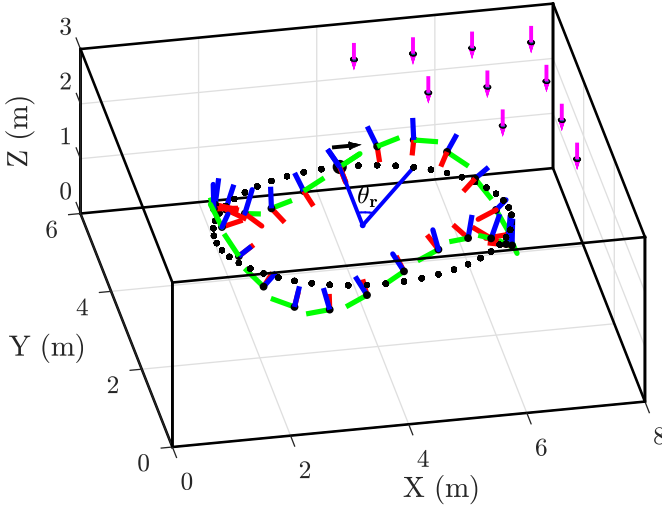


Figure 4.3: Simulation setup. The three orthonormal vectors in three different colors at each sample on the path represent the frame of the receiver (shown with $\theta_R = 0$ rad), where the red, green and blue vector represent the x -axis, y -axis and z -axis, respectively. The pink arrows represent the LEDs (only a fraction of them are shown) on the ceiling. θ_r indicates the traveled angle along the dotted ellipse in the XY plane.

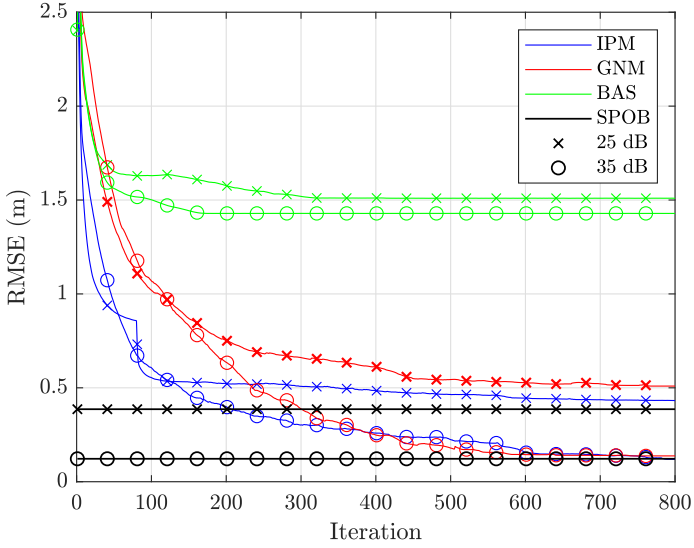
PDs, with four of them being symmetrically equipped around the centroid and tilted away from the center by $\theta_P = \pi/4$ rad. All PDs have a relative vector (the distance vector to the centroid) of $\mathbf{d}_{j,r} = d_j \mathbf{n}_{P,j,r}$, with $d_j = 0.02$ m (see Section 4.2.4 for the expression of $\mathbf{n}_{P,j,r}$). Each PD is assumed to have an FOV of $\theta_{FOV} = 4\pi/9$ rad, a unit responsivity $R_p = 0.3$ and an area of $A_R = \pi r_P^2$ with the radius $r_P = 1 \times 10^{-3}$ m. The above parameter settings for the physical properties of the LEDs and the PDs are similar to the ones used in [67]. To evaluate the performance of the estimators, we consider the path shown in Fig. 4.3. The path has an elliptical pattern in the XY plane and a sinusoidal pattern in the Z direction. The semi-major axis and the semi-minor axis of the ellipse are 2.5 m and 1.5 m, respectively. The ellipse (the dotted line) is centered at $[4.0, 3.0, 1.5]^T$ m, i.e. the center of the considered area. Starting at the coordinates $[4.0, 4.5, 1.5]^T$ m (the black arrow), the path oscillates sinusoidally in the Z direction and completes the path with three periods. The receiver follows the path clockwise, and at each sample point the orientation of the receiver is chosen such that the frame of the receiver is tangent to the path, more specifically, $\mathbf{R} = \exp((\theta_R \mathbf{n}_{R,y})^\wedge) \mathbf{R}_0$, where $\mathbf{R}_0 = [\mathbf{n}_{R,x}, \mathbf{n}_{R,y}, \mathbf{n}_{R,z}]$, $\mathbf{n}_{R,z} = \mathbf{n}_{R,x} \times \mathbf{n}_{R,y}$, $\mathbf{n}_{R,y}$ is the unit tangent vector of the path at the sample point, $\mathbf{n}_{R,x}$ is the unit vector that resides in the XY plane and satisfies $\mathbf{n}_{R,x}^T \mathbf{n}_{R,y} = 0$ and $[\mathbf{n}_{R,z}]_3 > 0$, and θ_R (the roll angle) controls how much \mathbf{R}_0 is rotated around

$\mathbf{n}_{R,y}$. The frame of the receiver (the column vectors of \mathbf{R}) along the path is illustrated in Fig. 4.3 (shown with $\theta_R = 0$ rad) by three orthonormal vectors in three different colors. Here we define a parameter θ_r to specify the sample point, where θ_r is the traveled angle along the ellipse pattern in the XY plane. In the following, the SNR is defined as $\text{SNR} \triangleq \left(\frac{(\gamma+1)A_R P_t R_p}{2\pi\sigma_w} \right)^2$. To the best of our knowledge, there is no algorithm that simultaneously estimates position and orientation for MLMP-based VLP systems. Therefore, for comparison, we will use as baseline method the algorithm from [68]³, which estimates the position of the receiver only. In this baseline method, we set the rotation matrix $\hat{\mathbf{R}}$ equal to the identity matrix, i.e., we assume the receiver points straight upwards.

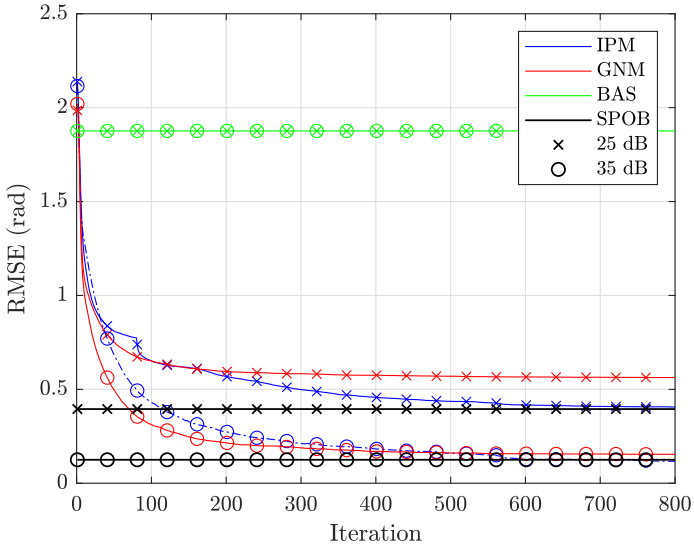
4.4.1 Performance of the Estimators

First, we consider the case of a roll angle $\theta_R = -\pi/3$ rad, implying the x -axis of the receiver frame stays $-\pi/3$ rad off the horizon in the system frame. The convergence behavior of the proposed methods is presented in Fig. 4.4, which gives the average RMSE over the entire path as a function of the number of iterations when $\text{SNR} = 25$ dB and $\text{SNR} = 35$ dB. First, we notice that, as expected, the baseline method (BAS) shows an improving performance as a function of the number of iterations for the position estimation, but a high, constant RMSE for the orientation estimation. This is explained as the baseline method estimates only the position but not the orientation. Because of this limitation, the gap between the RMSE of the baseline method and the root of the proposed CRB (SPOB) is the largest. On the other hand, the proposed algorithms based on the Gauss-Newton method (GNM) and the interior point method (IPM) converge to the SPOB for a SNR of 35 dB, and show only a small gap with the SPOB for a SNR of 25 dB. Hence, the proposed algorithms outperform the algorithm from [68]. Comparing the convergence rate, we see that the convergence for the orientation is similar for both the GNM and the IPM, whereas for the position estimation, the GNM shows a slower convergence. This is due to the absence of the boundary condition in the GNM, implying outliers can occur where the algorithm returns a position estimate outside the considered area, resulting in large errors that slow down the convergence. In Figs. 4.5 and 4.6, the RMSE of the estimate of the position and orientation for the proposed estimators are shown as a function of θ_r for the same SNRs as used in Fig 4.4. Taking into account that the path we consider has a sinusoidal pattern in the Z direction, there is a relatively larger distance between the receiver and the LED in the valleys of the path. At the same time, since the path has an elliptical pattern in the XY plane, the largest distance between the receiver and the LED occurs at the vertex of the ellipse lying in a valley. Since the channel gain is inversely proportional to the distance between the

³Note that the estimator [68] is originally designed for a receiver with a single PD and under the assumption that the receiver is parallel to the ceiling. In this chapter, we extend it to a receiver with multiple PDs and under the assumption that the receiver is parallel to the ceiling.

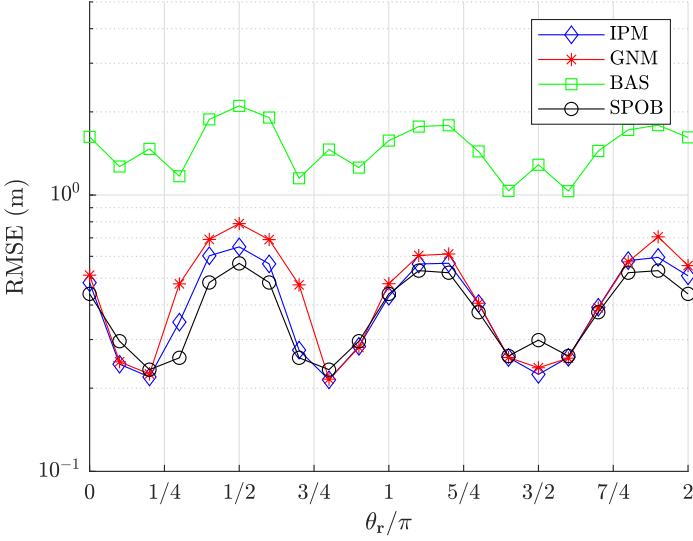


(a)

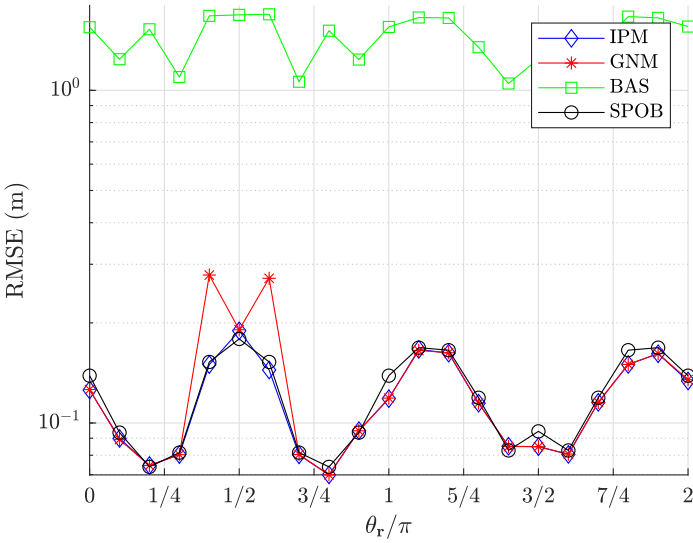


(b)

Figure 4.4: RMSE versus iteration for SNR= 25 dB and SNR= 35 dB. (a) Position estimation errors, (b) Orientation estimation errors.

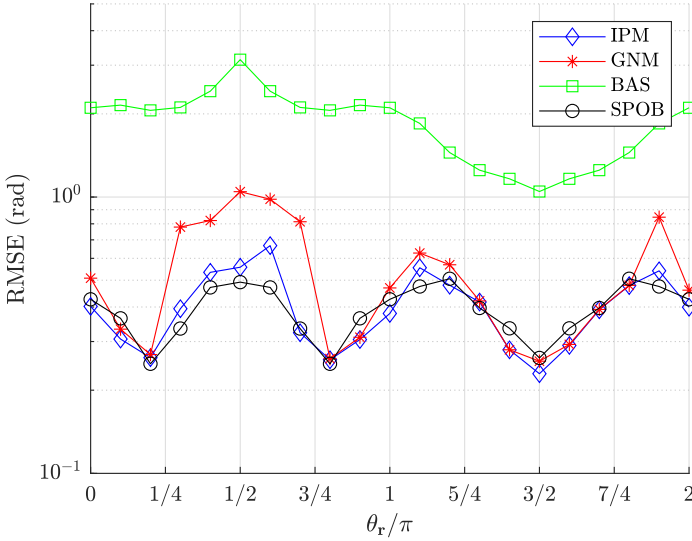


(a)

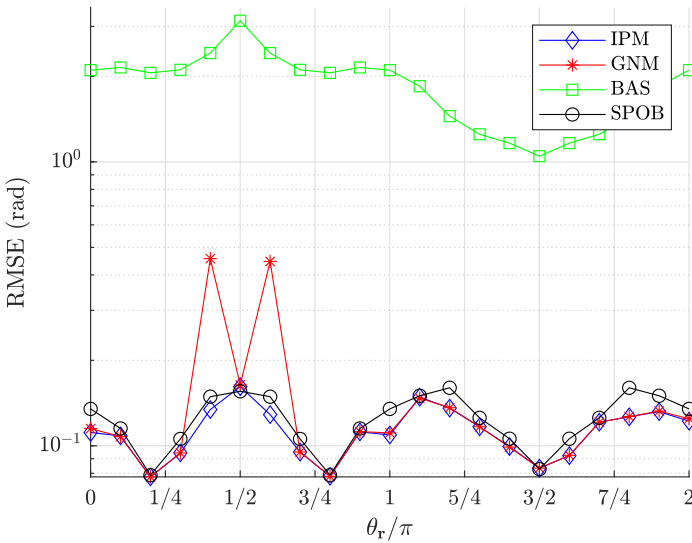


(b)

Figure 4.5: RMSE of the position estimate and the theoretical bound for $\theta_R = -\pi/3$ rad with (a) SNR = 25 dB and (b) SNR = 35 dB.



(a)



(b)

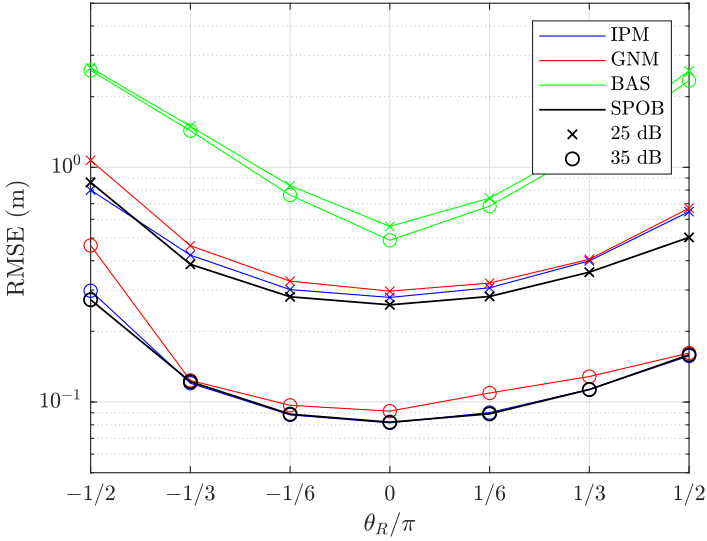
Figure 4.6: RMSE of the orientation estimate and the theoretical bound for $\theta_R = -\pi/3$ rad with (a) SNR = 25 dB and (b) SNR = 35 dB.

receiver and the LED, a higher RMSE is expected at those points in the path that have a larger distance between the receiver and the LEDs. This can be observed in Figs. 4.5 and 4.6, where the performance along the path shows a sinusoid-like pattern with three peaks and valleys appearing in the RMSEs, corresponding to the valleys and peaks in the path. The largest RMSE is obtained around $\theta_r = \pi/2$ rad, which corresponds to the largest distance point (the vertex in the valley). Comparing the performances for different SNRs, we can see that for SNR = 35 dB, both proposed estimators reach the theoretical bound, while for SNR = 25 dB, the IPM outperforms the GNM. As can be observed, the RMSE of the baseline method for both position and orientation estimation is (approximately) the same for 25 dB and 35 dB SNR. Hence, due to the absence of orientation estimation in the baseline method, the position estimate suffers from a bias. The baseline's RMSE for the orientation is due to the difference between the true orientation, specified by the path, and the reference orientation used in the baseline method, i.e., the identity matrix. As can be seen in Figs. 4.5 and 4.6, the baseline method generally performs worse since the true orientation \mathbf{R} is not the identity matrix. In Figs. 4.4, 4.5 and 4.6, we observe that at SNR = 25 dB, there is a gap between the performance of the proposed methods (GNM and IPM) and the SPOB. This gap is caused by the threshold phenomenon of the CRB, which will be discussed in the following subsection.

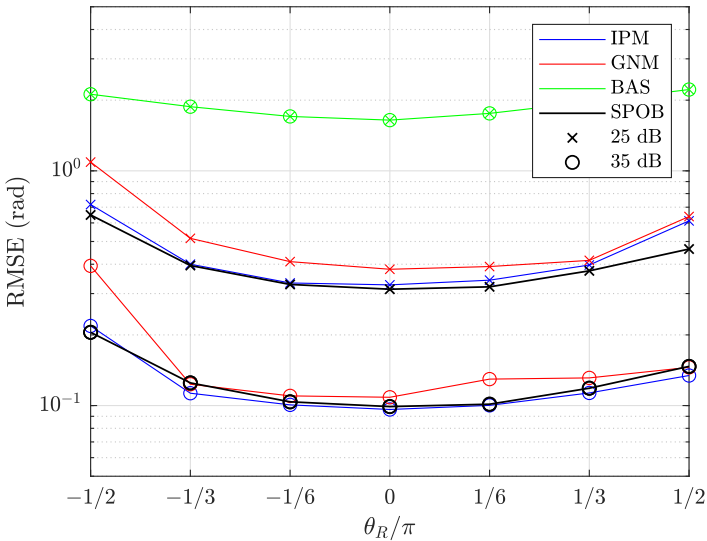
Next, we will investigate the effect of the receiver orientation on the performance. Fig. 4.7 gives the average RMSE over the entire path as a function of the roll angle θ_R when SNR = 25 dB and SNR = 35 dB. Because all LEDs are attached to the ceiling, the receiver will sense fewer LEDs when θ_R is increased. This can be observed in Fig. 4.7, as the RMSE increases when $|\theta_R|$ increases. Further, from the figure, it follows that the performance is worse when $\theta_R < 0$ rad. This can be explained as when $\theta_R < 0$ rad, the receiver is tilted towards the side boundary of the area, implying fewer LEDs will be visible compared to the case with $\theta_R > 0$ rad. It also can be seen in Fig. 4.7 that when the magnitude of θ_R increases, the estimators' performance degrades, and $\theta_R = 0$ rad corresponds to the best performance. Comparing the proposed estimators, we observe that the IPM outperforms the GNM. Especially when $\theta_R < 0$ rad, the GNM fails to converge properly, as the number of LEDs seen by the receiver is too low.

4.4.2 Asymptotic Tightness

In this section, to investigate the asymptotic tightness of the theoretical bound, the estimators are simulated for various values of SNR and numbers of LEDs. The configuration is the same as in Fig. 4.3. In Figs. 4.8 and 4.9, we show the RMSE averaged over the path for two roll angles (Case 1: $\theta_R = 0$ rad, Case 2: $\theta_R = -\pi/3$ rad) as a function of the SNR (Fig. 4.8a and 4.8b), and as a function of the number N_L of LEDs (Fig. 4.9a and 4.9b). As expected, increasing the SNR or N_L leads to a lower RMSE, and we observe an asymptotic tightness of both proposed estimators to the lower bound. Due to the introduced bias,



(a)



(b)

Figure 4.7: RMSE versus θ_R for SNR= 25 dB and SNR= 35 dB. (a) Position estimation errors, (b) Orientation estimation errors.

the performance of the baseline method shows an error floor when SNR or N_L is large. At low SNR or low N_L , the RMSE deviates from the SPOB. This is explained as for these cases, the bias in the position and orientation estimates becomes non-negligible. Taking into account that the CRB only can serve as a lower bound for unbiased estimators, this implies that, below a threshold for the SNR or N_L , no asymptotic tightness can be reached between the RMSE of the proposed estimators and the SPOB.

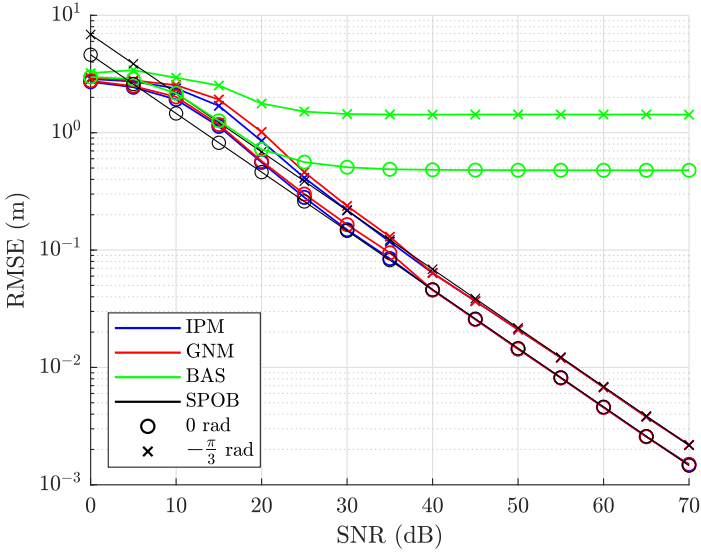
4.4.3 Impact of Location of the Receiver

In this section, we investigate the CRB as a function of the position of the receiver. Considering the setup illustrated in Fig. 4.3, the averaged SPOBs on the position vector and the orientation matrix are shown in Fig. 4.10 and 4.11, respectively. The SPOB for SNR = 35 dB is shown in Fig. 4.10a and Fig. 4.11a for the XY plane fixed at $z = 1.5$ m, while in Fig. 4.10b and Fig. 4.11b the SPOB averaged over the XY plane is plot as a function of the height for SNR = {25, 35, 45} dB. The spatial sample points are evenly distributed in the area with an interval of 0.2 m, and at each sample point, multiple random orientations of the receiver are generated. Considering that in reality the receiver will be placed roughly upwards, the zenith angle of the generated orientation is uniformly distributed within the interval $[-\pi/3, \pi/3]$ rad. The corresponding random rotation matrix can be generated using the fast algorithm given in [69].

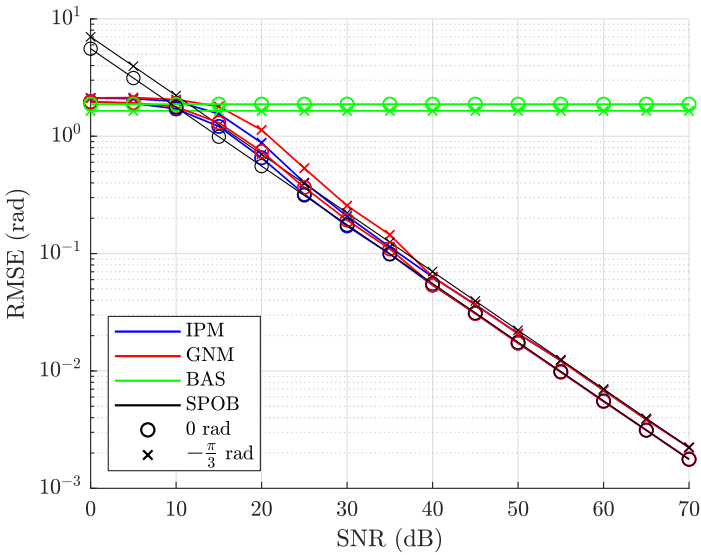
Due to the limited FOV of the receiver, the closer the receiver is to the side boundary of the area, the lesser LEDs it will sense. This explains the inverted dome shape of the SPOB in Fig. 4.10a and Fig. 4.11a, where the lowest point is obtained near the center of the XY plane, while the largest values locate around the four corners. The limited FOV also explains the results of Fig. 4.10b and Fig. 4.11b, where the SPOB is shown as a function of the height of the receiver. While the SPOB first improves for increasing height, as the distance between the LEDs and the receiver reduces, for larger heights, the SPOB degrades again, because the angle between the receiver and the LEDs increases, and the LEDs start to fall outside the FOV of the receiver.

4.4.4 Configuration of the Receiver

In this section, we investigate the impact of the diversity angle θ_P , i.e., the tilt angle between the PDs and the centroid of the receiver, on the position and orientation estimation accuracy. By increasing θ_P , we increase the FOV of the receiver, as the receiver array will be able to sense LEDs that are at larger incident angle. However, at the same time, each PD of the receiver will sense fewer LEDs because of the larger tilt angle, so the diversity of the receiver reduces. To find the optimal configuration, we use the theoretical lower bound as an indicator to find the optimal configuration that achieves the lowest possible value of the indicator. In order to obtain an indicator taking into account both the position and orientation, here, we define a unified estimation error vector $\boldsymbol{\theta}_e$ measuring the overall error, with $\boldsymbol{\theta}_e = [\mathbf{r}_e^T, \zeta \mathbf{u}_e^T]^T$, where $\zeta > 0$

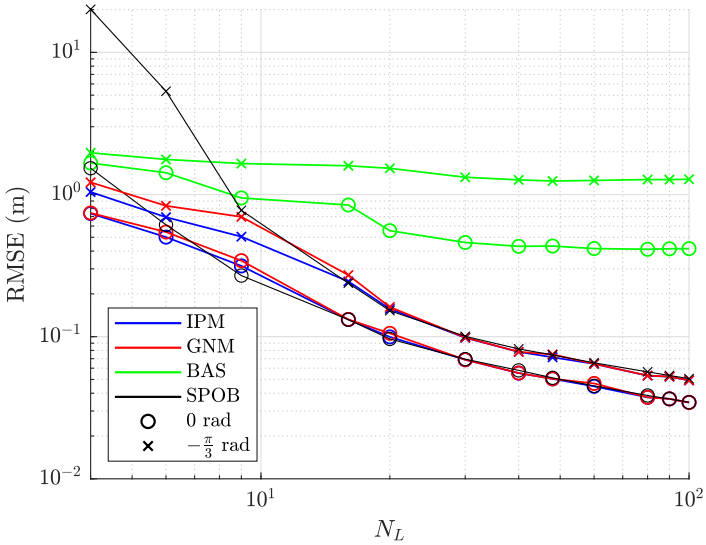


(a)

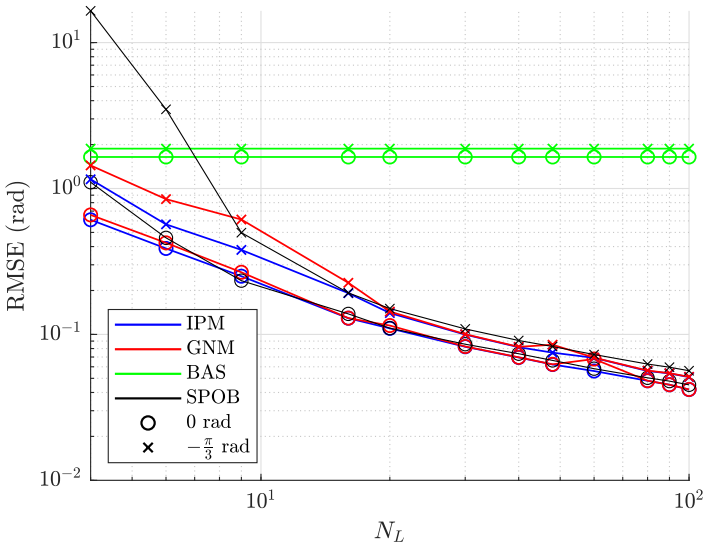


(b)

Figure 4.8: RMSEs of estimating position and orientation parameters as a function of SNR when $N_L = 24$ for Case 1: $\theta_R = 0$ rad and Case 2: $\theta_R = -\pi/3$ rad. (a) position estimation errors, bottom row, (b) orientation estimation errors.

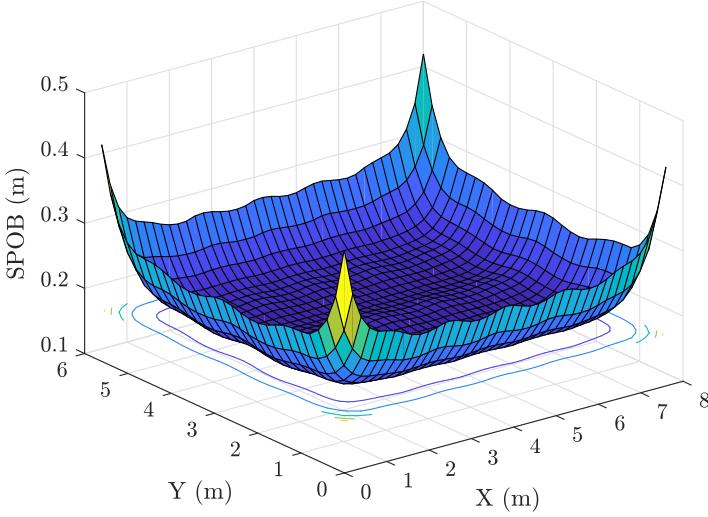


(a)

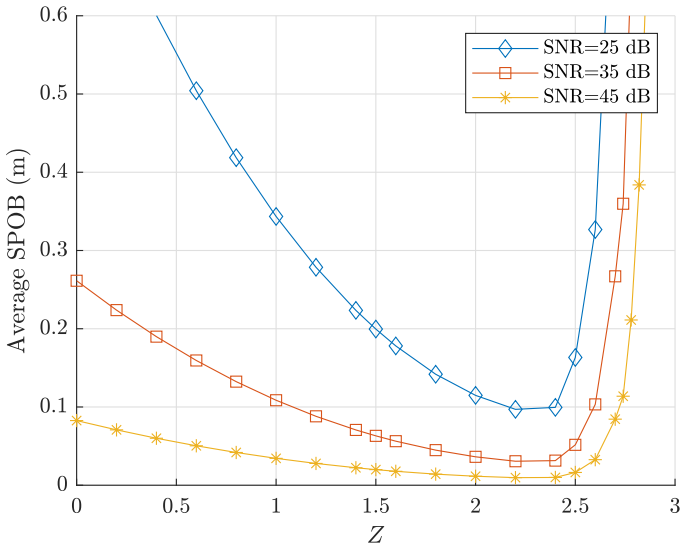


(b)

Figure 4.9: RMSEs of estimating position and orientation parameters and as a function of the number of LEDs when SNR = 35 dB for Case 1: $\theta_R = 0$ rad and Case 2: $\theta_R = -\pi/3$ rad. (a) position estimation errors, (b) orientation estimation errors.

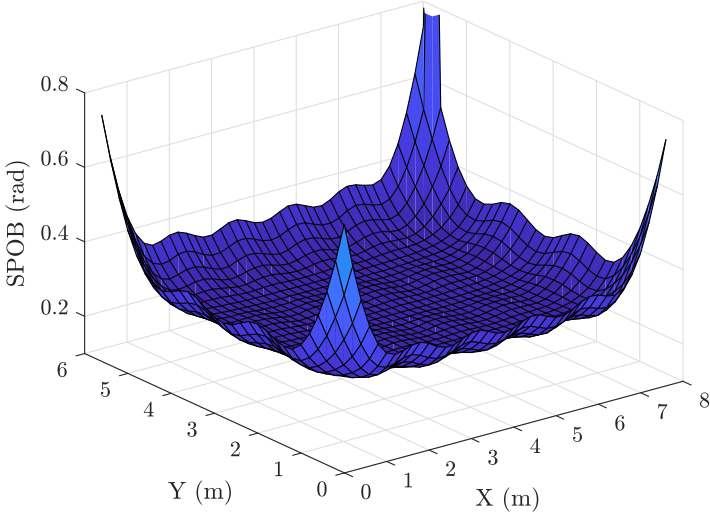


(a)

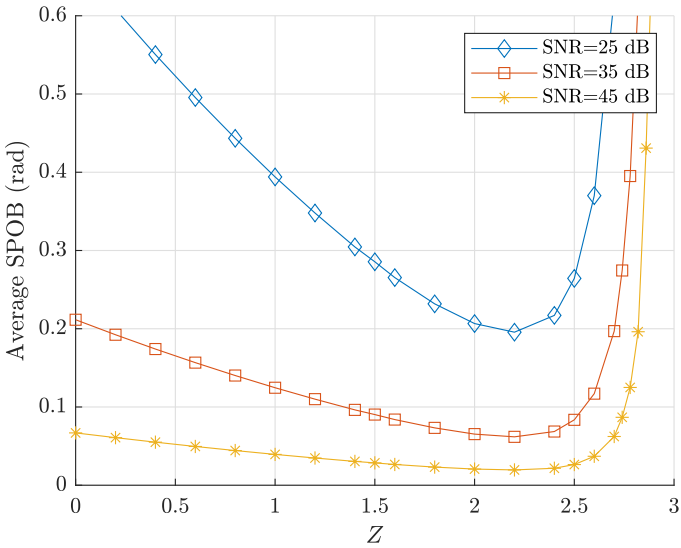


(b)

Figure 4.10: Averaged SPOB on the position vector (a) as a function of the position in the XY plane fixed at 1.5 m in z-axis, (b) as a function of the height.

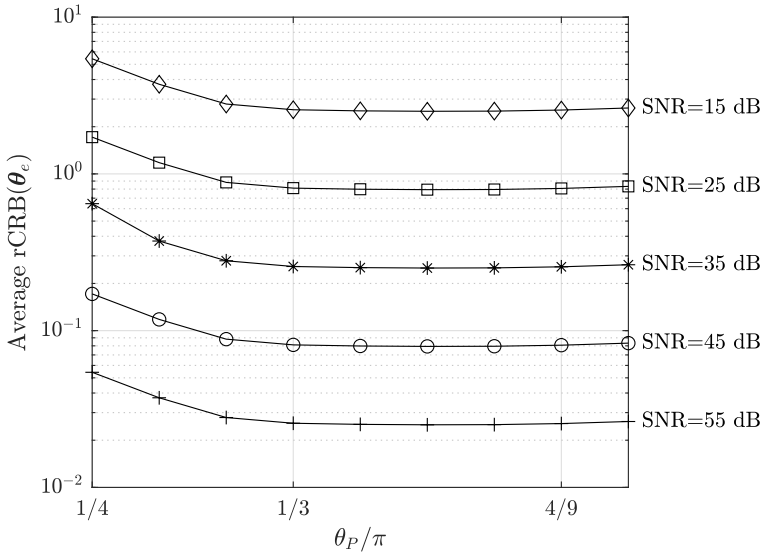


(a)

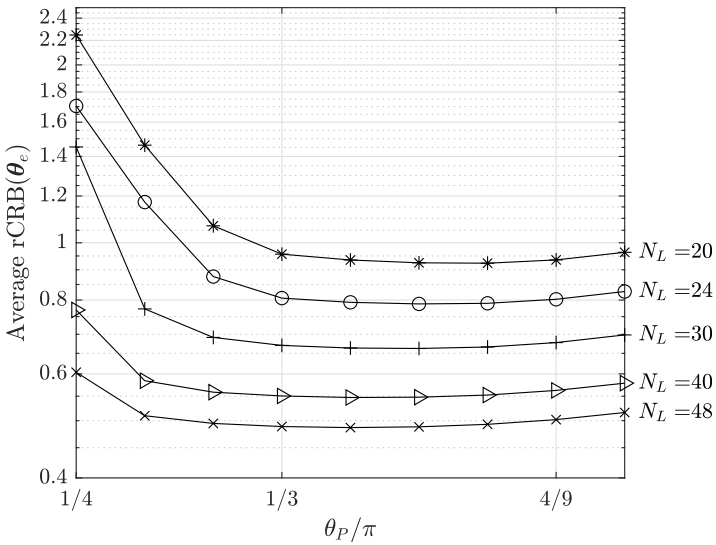


(b)

Figure 4.11: Averaged SPOB on the orientation matrix (a) as a function of the position in the XY plane fixed at 1.5 m in z -axis, (b) as a function of the height.



(a)



(b)

Figure 4.12: The averaged indicator as a function of θ_P . (a) Indicator for different SNRs (b) Indicator for different N_L s.

reflects the scale order on the orientation error compared to the position error. Then using the CRB for vector parameter transformation [66, eq. (3.30)], the error covariance matrix of \mathbf{g}_e is lower bounded by

$$E\{\boldsymbol{\theta}_e \boldsymbol{\theta}_e^T\} \succeq \text{diag}([\mathbf{1}^T, \zeta \mathbf{1}^T]) \mathbf{J}^{-1} \text{diag}([\mathbf{1}^T, \zeta \mathbf{1}^T]). \quad (4.31)$$

The square root of this bound on the unified estimation error vector $\boldsymbol{\theta}_e$ is used as an indicator.

The system setup and the sampling method used in Subsection 4.4.3 are considered. From the previous results, we found that the SPOBs on the position and orientation errors are of the same magnitude. Therefore, we set the scale factor $\zeta = 1$. As can be seen from the previous analysis, the SPOB significantly degrades when the height is larger than 2.5 m, and considering that in many cases, the user's main active area is in the lower middle area, samples with a height larger than 2.5 m are discarded. The spatial averaged indicator is first plotted in Fig. 4.12a for different SNR and is then plotted in Fig. 4.12b for different N_L . From Fig. 4.12a, it follows that the minimum of the indicator is obtained at $\theta_P = \pi/3$ rad for all SNR values. However, it can also be observed that the minimum is very broad, indicating that the performance will be rather insensitive to the value of the tilt angle for given SNR. When changing the number N_L of LEDs, we see a larger dependency on θ_P , especially for small values of N_L (see Fig. 4.12b). When N_P is sufficiently large, again the optimal tilt angle equals $\theta_P = \pi/3$ rad. However, when $N_L \leq 30$, the performance rapidly degrades when $\theta_P \leq 11\pi/36$ rad, and the optimal value of the tilt angle increases. This can be explained as when fewer LEDs are available, a larger FOV is required to capture more LEDs at the receiver.

4.5 Conclusion

In this study, we design two RSS-based simultaneous position and orientation estimation algorithms for a visible light system. Both algorithms exploit the principle of optimization on manifolds, which alleviates the constraints imposed by the restrictions on the rotation matrix, and increases the robustness of estimation. As the proposed algorithms are iterative and need a proper initialization to converge, we propose a coarse estimator that uses the direct linear transformation. To theoretically analyze the proposed estimators, we evaluate the CRB for simultaneous position and orientation estimation. The part of the CRB corresponding to the orientation errors is the intrinsic CRB, and is used to measure errors in the estimated rotation matrix in a physically meaningful way.

The proposed estimators show asymptotic convergence to the CRB, indicating the proposed estimators have excellent performance. Comparing the results of both algorithms before convergence, we show that the interior point method outperforms the Gauss-Newton method, but at the cost of complexity.

Based on the CRB, we also investigated the performance of the simultaneous position and orientation estimation as a function of the position of the receiver

and the parameters of the system. Based on these results, we can conclude that the optimal configuration of the receiver consists of PDs that are tilted over $\pi/3$ rad with respect to the normal of the receiver, to obtain a good trade-off between the FOV and diversity of the receiver.

The research mentioned in this chapter was published in [70].

5

Hybrid Position and Orientation Estimation in the Presence of Prior Information on Orientation

In many cases, the orientation of the receiver is estimated with an external orientation estimation device. However, these devices generally suffer from drift and misalignment, causing an uncertainty in the orientation presented to the receiver. Hence, the external device can only provide a coarse estimate of the orientation to the position estimator, of which its probability distribution can be used as prior information for the position estimation. Since the orientation of a receiver greatly affects the performance of a visible light system, the orientation uncertainty will degrade the performance of standard positioning algorithms, implying it should be taken into account when designing a robust positioning algorithm. Existing positioning algorithms extracting the orientation information from an external device often neglect the uncertainty generated by the external device and assume the orientation is perfectly estimated. In such a situation, the maximum likelihood estimator tries to estimate the position based on a misspecified model, i.e. in which the orientation is considered as uncertainty-free instead of satisfying some random process. In the following, we refer to this type of estimator as the misspecified maximum likelihood (MML) estimator [43]. For example, the algorithm from [68]¹, which in this chapter is used to compare with the proposed estimator, and therefore is evaluated subject to the orientation uncertainty, can be considered as a MML estimator.

In this chapter, we design an RSS-based hybrid position and orientation estimation algorithm using the hybrid maximum likelihood (ML)/maximum a

¹Note that the estimator [68] is originally designed for a receiver with a single PD and under the assumption that the receiver is parallel to the ceiling. However, the extension to a receiver with multiple PDs and perfectly known orientation is straightforward.

posteriori (MAP) (HMM) principle for the angular diversity receiver to take into account the presence of prior information on the orientation. The proposed HMM estimator is compared with three existing estimators, i.e., the simultaneous position and orientation (SPO) estimator, the misspecified maximum likelihood (MML) estimator and the first-order-approximation-based positioning algorithm (AP1st), subject to the orientation uncertainty. Further, in order to analytically assess the performance of the proposed estimator, the theoretical lower bound on the mean squared error (MSE), i.e. the hybrid Cramér-Rao bound (HCRB) for HMM is derived. In the last part of this chapter, numerical results comparing the proposed algorithm with state-of-the-art algorithms, and the comparison with the theoretical lower bound, are given.

5.1 Problem Statement

In this chapter, we consider the same system containing N_L LEDs and a VLP receiver containing N_P bare PDs mounted on the receiver, as shown in Fig. 2.7. Hence, recalling the discussion in previous chapters, we have the $N_L N_P \times 1$ observation vector $\mathbf{y} = [\mathbf{y}_1^T, \dots, \mathbf{y}_{N_P}^T]^T$, with $\mathbf{y}_j = [y_{1,j}, \dots, y_{N_L,j}]^T$. Assuming the LOS component dominates the received signal, we have

$$\mathbf{y} = \mathbf{g} + \mathbf{w}, \quad (5.1)$$

where the $N_L N_P \times 1$ vector \mathbf{g} is given by $\mathbf{g} = [\mathbf{g}_1^T, \dots, \mathbf{g}_{N_P}^T]^T$ with $\mathbf{g}_j = R_{p,j} [P_{t,1} h_{1,j}, \dots, P_{t,N_L} h_{N_L,j}]^T$, $h_{i,j}$ is given in (2.17), $P_{t,i}$ is the power transmitted by the i^{th} LED and $R_{p,j}$ is the responsivity of the j^{th} PD. The $N_L N_P \times 1$ vector \mathbf{w} models the shot and thermal noise, which is represented by a zero-mean multivariate Gaussian random variable with covariance matrix $\Sigma_{\mathbf{w}} = \sigma_w^2 \mathbf{I}_{N_L N_P}$. Additionally, it is assumed that an external orientation estimation device is available, and the estimate $\tilde{\mathbf{R}} \in SO(3)$ of the rotation matrix \mathbf{R} , obtained with the external device, is modeled by $\tilde{\mathbf{R}} = \mathbf{R}_{\epsilon} \cdot \mathbf{R}$, where $\tilde{\mathbf{R}}_{\epsilon} \in SO(3)$ represents the random error component contained in the estimation.

Based on the observation (5.1), the designed estimator should estimate the position vector \mathbf{r} and the rotation matrix \mathbf{R} from the incoming light in the optical receiver, assuming $\tilde{\mathbf{R}}$ and $p(\mathbf{R}_{\epsilon})$ are known. In the next subsection, we will discuss the model that will be used for the orientation uncertainty.

5.1.1 Model of Orientation Uncertainty

According to Euler's rotation theorem [50], the random rotation can be expressed as

$$\begin{aligned} \mathbf{R}_{\epsilon} &= \exp(\epsilon^{\wedge}) \\ &= \exp \begin{pmatrix} 0 & -\epsilon_z & \epsilon_y \\ \epsilon_z & 0 & -\epsilon_x \\ -\epsilon_y & \epsilon_x & 0 \end{pmatrix} \end{aligned} \quad (5.2)$$

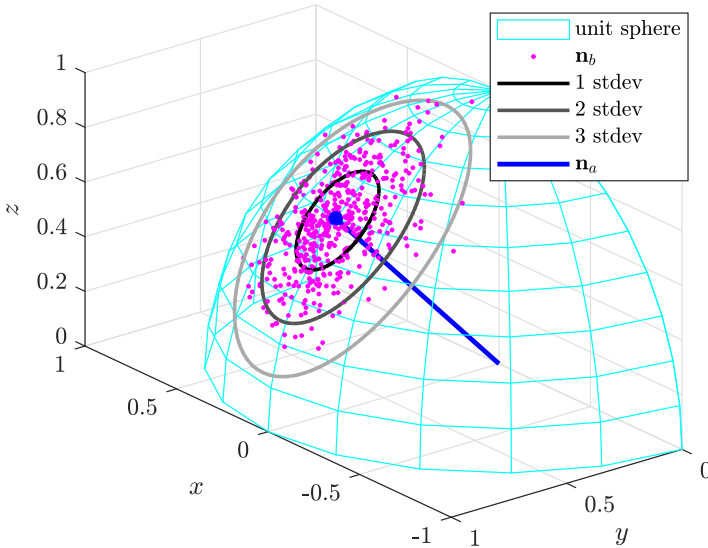


Figure 5.1: Distribution of $\mathbf{n}_b = \mathbf{R}_\epsilon \mathbf{n}_a$.

where the skew-symmetric matrix ϵ^\wedge is constructed from the vector $\epsilon = [\epsilon_x \ \epsilon_y \ \epsilon_z]^\top$ using the operator $(\cdot)^\wedge$. Physically, ϵ is the axis-angle representation of \mathbf{R}_ϵ and equation (5.2) is equivalent to Rodrigues' rotation formula that converts the axis-angle representation to the rotation matrix representation. Consequently, \mathbf{R}_ϵ realizes the rotation that rotates the rigid object around the unit axis of $\epsilon/\|\epsilon\|$ by an angle $\|\epsilon\|$. The distribution of \mathbf{R}_ϵ is specified by the rotation vector ϵ (see Chapter 3.2.3), which is assumed to be zero-mean Gaussian [26]. To illustrate the effect of a random rotation \mathbf{R}_ϵ , Fig. 5.1 shows the impact of \mathbf{R}_ϵ on a unit vector $\mathbf{n}_b = \mathbf{R}_\epsilon \mathbf{n}_a$, where \mathbf{n}_a is constant. The sampled \mathbf{n}_b (magenta dots) are concentrated around \mathbf{n}_a (the blue dot) and distributed on the unit sphere (the cyan mesh). The contours show the first 3 standard deviations of ϵ mapped to \mathbf{n}_b .

By left multiplying $\tilde{\mathbf{R}}$ with \mathbf{R}_ϵ^\top , we have $\mathbf{R} = \mathbf{R}_\epsilon^\top \tilde{\mathbf{R}}$, which induces the PDF $p(\mathbf{R}|\tilde{\mathbf{R}})$ of \mathbf{R} conditioned on $\tilde{\mathbf{R}}$. This PDF gives the probability distribution of true orientation \mathbf{R} given an estimate $\tilde{\mathbf{R}}$, and \mathbf{R}_ϵ^\top models the uncertainty in the orientation estimate $\tilde{\mathbf{R}}$. Therefore, $p(\mathbf{R}|\tilde{\mathbf{R}})$ will serve as prior information about the orientation in the position estimator that uses the light signal. It can be seen that $p(\mathbf{R}|\tilde{\mathbf{R}})$ is specified by $p(\mathbf{R}_\epsilon^\top)$, which is coupled with $p(\mathbf{R}_\epsilon)$ and determined by the PDF $p(\epsilon)$ as well, since $\mathbf{R}_\epsilon^\top = \exp((-\epsilon)^\wedge)$.

5.1.2 Approximation to the Orientation Uncertainty Model

It can be seen that the \mathbf{R}_ϵ depends on ϵ in a nonlinear manner. In a bid to simplify the model, heuristically, we can have the linear approximation to the orientation uncertainty model by discarding the second and higher order terms in (3.35). Now, we evaluate the resulting RSS for a given estimate $\tilde{\mathbf{R}}$ using the approximation through simulations. To this end, we consider a simple case of a single LED-PD link. The cosine of the incidence angle (2.16) can be approximated by

$$\begin{aligned} \cos(\theta) &\approx -\frac{((\mathbf{I} - \epsilon^\wedge) \tilde{\mathbf{n}}_P)^\top \mathbf{v}}{\|\mathbf{v}\|} \\ &= -\frac{\tilde{\mathbf{n}}_P^\top \mathbf{v}}{\|\mathbf{v}\|} + \frac{(\tilde{\mathbf{n}}_P \times \mathbf{v})^\top \epsilon}{\|\mathbf{v}\|}, \end{aligned} \quad (5.3)$$

where $\tilde{\mathbf{n}}_P = \tilde{\mathbf{R}}\mathbf{n}_P$, $\mathbf{a} \times \mathbf{b}$ is the cross product of the vectors \mathbf{a} and \mathbf{b} . As a result, the channel gain (2.7) can be approximated by

$$h^{(1)} = \frac{K \cos^\gamma(\phi)}{\|\mathbf{v}\|^3} \left(\tilde{\mathbf{n}}_R^\top \mathbf{v} - (\tilde{\mathbf{n}}_R \times \mathbf{v})^\top \epsilon \right). \quad (5.4)$$

Using this first-order approximation, we find the approximated observation $y^{(1)} = R_p P_t h^{(1)} + w$. Taking into account that both ϵ and w are zero-mean Gaussian distributed, and the approximated gain and observation $y^{(1)}$ and $h^{(1)}$ are Gaussian distributed.

For evaluation, we assume the position and the normal of the LED are given by $\mathbf{r}_L = [0, 0, 3]^\top$ and $\mathbf{n}_L = [0, 0, -1]^\top$, i.e. the LED points straight downwards. Further, the LED transmits a power $P_t = 1$ W and has Lambertian order $\gamma = 1$. For the receiver, we consider a PD with area $A_R = \pi r_p^2$, $r_p = 1$ mm and FOV $\theta_{FOV} = 4\pi/9$ rad. The receiver is placed below the LED, i.e. $\mathbf{r} = [0, 0, 1.5]^\top$. The covariance matrix Σ_ϵ of the orientation uncertainty is assumed to be $\Sigma_\epsilon = \sigma_\epsilon^2 \mathbf{I}_{3 \times 3}$, where $\sigma_\epsilon^2 \in \{1.0 \times 10^{-1}, 1.0 \times 10^{-2}\}$ rad².

In order to numerically measure similarity of probability distributions, the Bhattacharyya distance is used, which is

$$D_B(p, q) = -\ln(BC(p, q)), \quad (5.5)$$

where $BC(p, q) = \sum_{i=1}^n \sqrt{p_i q_i}$ is the Bhattacharyya coefficient. We consider $D_B(y, y^{(1)})$ – the distance between the PDF of the RSSs y and $y^{(1)}$ – and $D_B(h, h^{(1)})$ – the distance between the PDF of the channel gains h and $h^{(1)}$ – as functions of the incidence angle $\tilde{\theta}$ of the VLP receiver.

As shown in Fig. 5.2, both distances $D_B(y, y^{(1)})$ and $D_B(h, h^{(1)})$ decrease as $\tilde{\theta}$ increases, implying that the first-order approximation achieves a better accuracy for a larger $\tilde{\theta}$. In addition, contrary to $D_B(h, h^{(1)})$, even if $\tilde{\theta}$ is small, $D_B(y, y^{(1)})$ is closer to zero, which means that the distribution of $y^{(1)}$ approximates the true distribution of y with a higher accuracy, although $h^{(1)}$ only

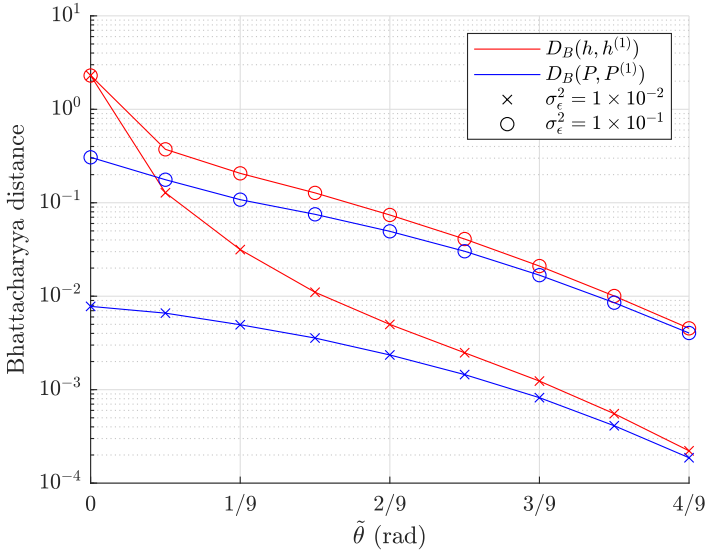


Figure 5.2: Bhattacharyya distance between received power and approximated ones.

approximates h accurately when $\tilde{\theta}$ is large. However, the accuracy degrades when σ_ϵ^2 increases.

Although, extending this first-order approximation to the receiver with multiple PDs, we can obtain an RSS-based position estimator using the maximum likelihood principle, which we call the first-order-approximation-based positioning (AP1st), its performance degrades when the accuracy of the approximation decreases according to the above analysis. Therefore, in the next section, we will propose a different method to incorporate the prior information on orientation.

5.2 RSS-Based Hybrid ML/MAP Estimation

In this section, we propose the hybrid ML/MAP (HMM) estimator, which takes into account the prior information on the orientation $p(\mathbf{R}|\tilde{\mathbf{R}})$, for the receiver with a PD array, and compare it with two state-of-the-art estimators.

In the previous chapter, we introduced a SPO algorithm that estimates the position and orientation of the receiver using the received light signal only, i.e. no prior information is available on the orientation. In this chapter, we assume prior information is available on the orientation, as described in the previous section. Prior information on a parameter to be estimated can be included by considering the maximum *a posteriori* (MAP) principle, using the joint PDF $p(\mathbf{y}, \Theta)$, where $\Theta = \{\mathbf{r}, \mathbf{R}\}$ consisting of the position vector \mathbf{r} and the rotation matrix \mathbf{R} , is the parameter set to be estimated. However, only for

the orientation \mathbf{R} , prior information is available, implying the MAP principle cannot be applied on the position estimation. Another approach to include the orientation uncertainty is to consider the orientation as a nuisance parameter and use the maximum likelihood (ML) principle to estimate the position only, using the likelihood function $p(\mathbf{y}|\tilde{\mathbf{R}}; \mathbf{r}) = \int_{\mathbf{R}} p(\mathbf{y}, \mathbf{R}|\tilde{\mathbf{R}}; \mathbf{r}) d\mathbf{R}$. However, although the distribution of ϵ is Gaussian, the rotation matrix \mathbf{R}_ϵ is not Gaussian distributed, as it is a non-linear transformation of ϵ . As a consequence, $\int_{\mathbf{R}} p(\mathbf{y}, \mathbf{R}|\tilde{\mathbf{R}}; \mathbf{r}) d\mathbf{R}$ becomes analytically intractable. To overcome the issues in the above mentioned approaches, we use as alternative the hybrid ML/MAP (HMM) principle (see Section 3.1.3) to jointly estimate the position and orientation of the receiver. In a hybrid ML/MAP estimator, the parameter set to be estimated is a combination of parameters with and without prior information. In this chapter, the hybrid parameter set Θ is defined as $\Theta = \{\mathbf{r}, \mathbf{R}\}$, where \mathbf{r} is the position vector without prior information and \mathbf{R} is the rotation matrix with prior information. The HMM estimator then jointly estimates \mathbf{r} and \mathbf{R} based on the joint PDF:

$$\begin{aligned} p(\mathbf{y}, \mathbf{R}|\tilde{\mathbf{R}}; \mathbf{r}) &= p(\mathbf{y}|\mathbf{R}; \mathbf{r})p(\mathbf{R}|\tilde{\mathbf{R}}) \\ &= p(\mathbf{y}|\Theta)p(\epsilon) \left| \det(\nabla_{\mathbf{R}}\epsilon|_{-\epsilon}) \right| \end{aligned} \quad (5.6)$$

where $p(\mathbf{y}|\Theta)$ is Gaussian distributed with $\mathbf{y}|\Theta \sim \mathcal{N}(\mathbf{g}(\Theta), \Sigma_{\mathbf{w}})$, and the conditional PDF $p(\mathbf{R}|\tilde{\mathbf{R}})$ giving the prior information about \mathbf{R} is specified by $p(\mathbf{R}_\epsilon^T)$. In (5.6), the distribution of \mathbf{R}_ϵ^T is represented in terms of ϵ , which is Gaussian, using the relation $\epsilon = \log(\mathbf{R}_\epsilon)^V \sim \mathcal{N}(\mathbf{0}, \Sigma_\epsilon)$, where the operator of $(\cdot)^V$ converts $\mathbf{a}^\wedge \in \mathfrak{so}(3)$ into the vector \mathbf{a} , i.e the inverse operator of $(\cdot)^\wedge$, and the last factor in the last equality of (5.6) comes from the change of variables, where (see equations (3.46) and (3.47))

$$\nabla_{\mathbf{R}}\epsilon = \frac{\|\epsilon\|}{2} \cot \frac{\|\epsilon\|}{2} \mathbf{I}_3 + \left(1 - \frac{\|\epsilon\|}{2} \cot \frac{\|\epsilon\|}{2}\right) \frac{\epsilon\epsilon^T}{\|\epsilon\|^2} - \frac{\epsilon^\wedge}{2}, \quad (5.7)$$

$$\left| \det(\nabla_{\mathbf{R}}\epsilon) \right| = \frac{\|\epsilon\|^2}{2(1 - \cos \|\epsilon\|)}, \quad (5.8)$$

and where we took into account that (5.8) is an even function, i.e. $\left| \det(\nabla_{\mathbf{R}}\epsilon|_{-\epsilon}) \right| = \left| \det(\nabla_{\mathbf{R}}\epsilon) \right|$.

Based on (5.6), the HMM principle yields the estimate $\hat{\Theta} = \{\hat{\mathbf{r}}, \hat{\mathbf{R}}_\epsilon\}$ that maximizes the hybrid log-likelihood function:

$$\hat{\Theta} = \arg \max_{\Theta} \mathcal{L}_H(\Theta; \mathbf{y}), \quad (5.9)$$

and

$$\begin{aligned} \mathcal{L}_H(\Theta; \mathbf{y}) &= \ln p(\mathbf{y}|\Theta) + \ln p(\epsilon) + \ln \left| \det(\nabla_{\mathbf{R}}\epsilon) \right| \\ &\approx \text{const} - \frac{1}{2} \|\mathbf{y} - \mathbf{g}\|_{\Sigma_{\mathbf{w}}}^2 - \frac{1}{2} \|\epsilon\|_{\Sigma_\epsilon}^2, \end{aligned} \quad (5.10)$$

where $\|\mathbf{x}\|_{\Sigma}^2 = \mathbf{x}^T \Sigma^{-1} \mathbf{x}$ is the squared Mahalanobis distance with respect to covariance matrix Σ . In (5.10), we neglected the effect of the determinant (5.8), because in most practical situations ϵ is small so that $|\det(\nabla_{\mathbf{R}} \epsilon)|$ approaches 1, and neglecting this factor will result in an estimator with lower computational complexity. Next, we introduce two expanded vectors,

$$\check{\mathbf{y}} = [\mathbf{y}^T \mathbf{0}_{1 \times 3}]^T \in \mathbb{R}^{(N_L N_P + 3) \times 1}, \quad (5.11)$$

$$\check{\mathbf{g}} = \left[\mathbf{g}^T \sigma_w \epsilon^T \Sigma_{\epsilon}^{-\frac{1}{2}} \right]^T \in \mathbb{R}^{(N_L N_P + 3) \times 1}, \quad (5.12)$$

with $\Sigma_{\epsilon}^{-\frac{1}{2}}$ the matrix square root of Σ_{ϵ}^{-1} , and combine the last two terms in (5.10) to obtain

$$\mathcal{L}_H(\Theta; \mathbf{y}) = \text{const} - \frac{1}{2\sigma_w^2} (\check{\mathbf{y}} - \check{\mathbf{g}})^T (\check{\mathbf{y}} - \check{\mathbf{g}}). \quad (5.13)$$

In this way, (5.9) is turned into a constrained non-linear least squares (NLS) problem given by

$$\begin{aligned} \hat{\Theta} &= \arg \min_{\Theta} (\|\check{\mathbf{y}} - \check{\mathbf{g}}\|^2) \\ \text{s.t. } \mathbf{R}^T \mathbf{R} &= \mathbf{R} \mathbf{R}^T = \mathbf{I}, \\ \det(\mathbf{R}) &= +1, \end{aligned} \quad (5.14)$$

where the constraints impose that \mathbf{R} must be a member of $SO(3)$. Unfortunately, this constrained optimization problem has no closed-form solution, implying we need to resort to constrained non-linear optimization algorithms, which are complex, time consuming and non-robust. However, since $SO(3)$ is an embedded submanifold of $\mathbb{R}^{3 \times 3}$, we can estimate \mathbf{R} using the Gauss-Newton algorithm on the manifold $SO(3)$. In this algorithm, we iteratively update the estimates of $\Theta = \{\mathbf{r}, \mathbf{R}\}$ using

$$\mathbf{r}^{t+1} = \mathbf{r}^t + \Delta_{\mathbf{r}} \quad \text{and} \quad \mathbf{R}^{t+1} = \exp((\Delta_{\mathbf{R}})^{\wedge}) \mathbf{R}^t \quad (5.15)$$

where the incremental step $\Delta_{\Theta} = [\Delta_{\mathbf{r}}^T, \Delta_{\mathbf{R}}^T]^T$ is calculated by

$$\Delta_{\Theta} = -\eta (\nabla_{\Theta} \check{\mathbf{g}})^{\dagger} (\check{\mathbf{g}} - \check{\mathbf{y}}), \quad (5.16)$$

with η the step size, $(\cdot)^{\dagger}$ the Moore-Penrose pseudoinverse, and

$$\nabla_{\Theta} \check{\mathbf{g}} = \begin{bmatrix} \nabla_{\Theta} \mathbf{g} \\ \mathbf{0}_{3 \times 3} \quad \sigma_w \Sigma_{\epsilon}^{-\frac{1}{2}} \nabla_{\mathbf{R}} \epsilon \end{bmatrix} \in \mathbb{R}^{(N_L N_P + 3) \times 6} \quad (5.17)$$

the expanded Jacobian matrix with respect to Θ . The Jacobian matrix $\nabla_{\Theta} \mathbf{g}$ of \mathbf{g} with respect to Θ is the $N_L N_P \times 6$ matrix $\nabla_{\Theta} \mathbf{g} = [\nabla_{\Theta} \mathbf{g}_1, \dots, \nabla_{\Theta} \mathbf{g}_{N_P}]^T$ with $\nabla_{\Theta} \mathbf{g}_j = R_{p,j} [P_{t,1} \nabla_{\Theta} h_{1,j}, \dots, P_{t,N_L} \nabla_{\Theta} h_{N_L,j}]^T$, and (see Chapter 4)

$$\nabla_{\Theta} h_{i,j} = C_{i,j}.$$

$$\begin{bmatrix} \frac{\gamma(\mathbf{n}_i^T \mathbf{v}_{i,j})^{\gamma-1} (\mathbf{n}_{P,j}^T \mathbf{v}_i)}{\|\mathbf{v}_{i,j}\|^{\gamma+3}} \\ \frac{(\mathbf{n}_i^T \mathbf{v}_{i,j})^\gamma}{\|\mathbf{v}_{i,j}\|^{\gamma+3}} \\ -\frac{(\gamma+3)(\mathbf{n}_i^T \mathbf{v}_{i,j})^\gamma (\mathbf{n}_{P,j}^T \mathbf{v}_i)}{\|\mathbf{v}_{i,j}\|^{\gamma+5}} \end{bmatrix}^T \cdot \begin{bmatrix} \mathbf{n}_{L,i}^T & \mathbf{n}_{L,i}^T (\mathbf{d}_j^\wedge)^T \\ \mathbf{n}_{P,j}^T & \boldsymbol{\nu}_i^T (\mathbf{n}^\wedge)^T \\ \mathbf{v}_{i,j}^T & \boldsymbol{\nu}_i^T (\mathbf{d}_j^\wedge)^T \end{bmatrix}. \quad (5.18)$$

In this chapter, we compare the performance of the proposed HMM estimator with the performance of the SPO, the MML and the AP1st estimators. To better understand the results for these algorithms, we briefly compare the objective functions used by these algorithms with that of HMM estimator. In the SPO estimator, the algorithm fully distrusts the available orientation estimate $\tilde{\mathbf{R}}$ from the external device and assumes that no reliable information about $p(\mathbf{R}_\epsilon)$ is available, implying it has to estimate Θ from the observed vector \mathbf{y} only. Consequently, the log-likelihood equals $\mathcal{L}(\Theta; \mathbf{y}) = \ln p(\mathbf{y}|\Theta)$. In the MML estimator, the algorithm fully trusts the estimate of the orientation $\tilde{\mathbf{R}}$ and neglects the orientation uncertainty, i.e. the estimator misspecifies $\mathbf{R}_\epsilon = \mathbf{I}_3$ as a constant, implying the distribution of the vector of observed light signals is modeled as $\mathbf{y}|\mathbf{r}; \tilde{\mathbf{R}} \sim \mathcal{N}(\mathbf{g}(\mathbf{r}, \tilde{\mathbf{R}}), \Sigma_{\mathbf{w}})$. From the resulting misspecified distribution $p_m(\mathbf{y}|\mathbf{r}; \tilde{\mathbf{R}})$, the MML estimator obtains the estimate through the maximization of the likelihood function $\mathcal{L}_M(\mathbf{r}; \mathbf{y}) = \ln p_m(\mathbf{y}|\mathbf{r}; \tilde{\mathbf{R}})$. Finally, the AP1st algorithm approximates the likelihood function of \mathbf{r} with the PDF $p_a(\mathbf{y}|\mathbf{r}; \tilde{\mathbf{R}})$ corresponding to $\mathbf{y}|\mathbf{r} \sim \mathcal{N}(\mathbf{h}(\mathbf{r}, \tilde{\mathbf{R}}), \Sigma_{\mathbf{y}})$, where $\Sigma_{\mathbf{y}} = (\nabla_{\mathbf{R}}|_{\tilde{\mathbf{R}}} \mathbf{h}) \Sigma_\epsilon (\nabla_{\mathbf{R}}|_{\tilde{\mathbf{R}}} \mathbf{h})^T + \Sigma_{\mathbf{w}}$ with the Jacobian matrix $\nabla_{\mathbf{R}}|_{\tilde{\mathbf{R}}} \mathbf{h}$ of \mathbf{h} with respect to \mathbf{R} evaluated at $\tilde{\mathbf{R}}$. Based on the approximated distribution $p_a(\mathbf{y}|\mathbf{r}; \tilde{\mathbf{R}})$, the AP1st algorithm obtains the estimate through the maximization of the likelihood function $\mathcal{L}_A(\mathbf{r}; \mathbf{y}) = \ln p_a(\mathbf{y}|\mathbf{r}; \tilde{\mathbf{R}})$. Notice that the AP1st algorithm does not estimate the orientation, i.e., it is a positioning algorithm.

Besides the performance of the algorithms, which will be discussed in Section 5.4, we are also interested in their complexity. All algorithms except AP1st can be converted into a NLS problem, which can be solved with the Gauss-Newton method. In the Gauss-Newton method, the complexity during each iteration is dominated by the computation of the Moore-Penrose pseudoinverse. As a consequence, the HMM, SPO and MML algorithm, respectively, have a complexity of $\mathcal{O}(6(N_L N_P + 3)^2)$, $\mathcal{O}(6(N_L N_P)^2)$ and $\mathcal{O}(3(N_L N_P)^2)$ flops per iteration. On the other hand, the complexity of the AP1st algorithm is dominated by the matrix inversion of $\Sigma_{\mathbf{y}}$ required to obtain the gradient in each inner iteration. Therefore, the AP1st algorithm has a complexity of $\mathcal{O}((N_L N_P)^3)$ flops per iteration. Hence, it is clear that the complexity of the HMM algorithm is lower than that of the AP1st algorithm but roughly equivalent to the complexity of the rest algorithms.

5.3 The Theoretical Lower Bound

In the numerical results section, we will use the mean squared error (MSE)

to compare the performance of the proposed HMM estimator with the performance of the SPO estimator and MML estimator. As no closed-form solution is available for the estimators, we will determine the performance through simulations. To obtain insight into the optimality of the proposed estimator, in this section, we derive the hybrid Cramér-Rao lower bound (HCRB), which is the theoretical lower bound on the MSE for the HMM estimator.

Using this HCRB, we can evaluate the estimation errors on the position, which is expressed by the Euclidean distance between $\hat{\mathbf{r}}$ and \mathbf{r} , i.e. $\mathbf{r}_e = \hat{\mathbf{r}} - \mathbf{r}$, and on the axis-angle vector between $\hat{\mathbf{R}}$ and \mathbf{R} , i.e. $\mathbf{u}_e = \log(\hat{\mathbf{R}}\mathbf{R}^T)^\vee$. In order to obtain the HCRB, first we need to calculate the hybrid information matrix (HIM) \mathbf{J}_H , which is given by [71, eq. (4.461)]

$$\begin{aligned}\mathbf{J}_H &= -E_{\mathbf{y}, \mathbf{R}|\tilde{\mathbf{R}}, \mathbf{r}} \left\{ \Delta_{\Theta}^{\ominus} \ln p(\mathbf{y}, \mathbf{R}|\tilde{\mathbf{R}}, \mathbf{r}) \right\} \\ &= \mathbf{J}_D + \mathbf{J}_P.\end{aligned}\quad (5.19)$$

where $E_{\mathbf{x}}\{f\}$ is the expectation of f with respect to the PDF of \mathbf{x} , $\Delta_{\mathbf{x}}^z = \nabla_{\mathbf{z}} \nabla_{\mathbf{x}}^T$ denotes the Hessian operator, and $\mathbf{J}_D = -E_{\mathbf{y}, \mathbf{R}|\tilde{\mathbf{R}}, \mathbf{r}} \left\{ \Delta_{\Theta}^{\ominus} \ln p(\mathbf{y}|\Theta) \right\}$ represents the contribution of the data (observed light signal), $\mathbf{J}_P = -E_{\mathbf{R}|\tilde{\mathbf{R}}} \left\{ \Delta_{\Theta}^{\ominus} \ln p(\mathbf{R}|\tilde{\mathbf{R}}) \right\}$ represents the contribution of the prior information on the orientation:

$$\mathbf{J}_D = E_{\mathbf{R}|\tilde{\mathbf{R}}} \left\{ \mathbf{J}_F(\Theta) \right\}, \quad (5.20)$$

$$\mathbf{J}_P = \begin{bmatrix} \mathbf{0} & \mathbf{0} \\ \mathbf{0} & \mathbf{J}_{\mathbf{R}} \end{bmatrix}. \quad (5.21)$$

Since $\mathbf{y}|\Theta$ is multivariate Gaussian with its covariance being independent of Θ , the associated Fisher information matrix (FIM) $\mathbf{J}_F(\Theta)$, i.e., the operand of the expectation in (5.20), can be calculated as [66, eq. (3.31)]:

$$\mathbf{J}_F(\Theta) = \frac{1}{\sigma_w^2} (\nabla_{\Theta} \mathbf{g})^T (\nabla_{\Theta} \mathbf{g}). \quad (5.22)$$

Further, the non-zero submatrix of (5.21) equals $\mathbf{J}_{\mathbf{R}} = E_{\mathbf{R}|\tilde{\mathbf{R}}} \left\{ (\nabla_{\mathbf{R}} \ln p(\mathbf{R}|\tilde{\mathbf{R}}))^T (\nabla_{\mathbf{R}} \ln p(\mathbf{R}|\tilde{\mathbf{R}})) \right\}$. Taking into account (3.44), (3.46) and (3.47), we have

$$\nabla_{\mathbf{R}} \ln p(\mathbf{R}|\tilde{\mathbf{R}}) = -\epsilon^T \left(\frac{\|\epsilon\| \sin \|\epsilon\| - 2(1 - \cos \|\epsilon\|)}{\|\epsilon\|^2 (1 - \cos \|\epsilon\|)} \mathbf{I}_3 + \Sigma_{\epsilon}^{-1} \right) \nabla_{\mathbf{R}} \epsilon. \quad (5.23)$$

Due to the complexity of $p(\mathbf{R}|\tilde{\mathbf{R}})$, the expectations for computing (5.20) and (5.21) are analytically intractable. Therefore, we calculate them numerically via Monte Carlo integration [72]:

$$\mathbf{J}_D \approx \frac{1}{N_M} \sum_{n=1}^{N_M} \mathbf{J}_F(\{\mathbf{r}, \mathbf{R}_n\}), \quad (5.24)$$

and

$$\mathbf{J}_{\mathbf{R}} \approx \frac{1}{N_M} \sum_{n=1}^{N_M} (\nabla_{\mathbf{R}} \ln p(\mathbf{R}|\tilde{\mathbf{R}}))^{\text{T}} (\nabla_{\mathbf{R}} \ln p(\mathbf{R}|\tilde{\mathbf{R}})) \Big|_{\mathbf{R}_n}, \quad (5.25)$$

where \mathbf{R}_n , $n = 1, \dots, N_M$ are i.i.d. samples generated from $p(\mathbf{R}|\tilde{\mathbf{R}})$. To get the lower bound on the error covariance matrices of \mathbf{r}_e and \mathbf{u}_e , we first rewrite the HIM \mathbf{J}_H as a partitioned matrix,

$$\mathbf{J}_H = \begin{bmatrix} \mathbf{J}_{H,r,r} & \mathbf{J}_{H,r,\mathbf{R}} \\ \mathbf{J}_{H,\mathbf{R},r} & \mathbf{J}_{H,\mathbf{R},\mathbf{R}} \end{bmatrix} \quad (5.26)$$

Consequently,

$$E\{\mathbf{r}_e \mathbf{r}_e^{\text{T}}\} \succeq \left[\mathbf{J}_{H,r,r} - \mathbf{J}_{H,r,\mathbf{R}} \mathbf{J}_{H,\mathbf{R},\mathbf{R}}^{-1} \mathbf{J}_{H,\mathbf{R},r} \right]^{-1}. \quad (5.27)$$

Similarly, the error covariance matrix of \mathbf{u}_e is lower bounded by

$$E\{\mathbf{u}_e \mathbf{u}_e^{\text{T}}\} \succeq \left[\mathbf{J}_{H,\mathbf{R},\mathbf{R}} - \mathbf{J}_{H,\mathbf{R},r} \mathbf{J}_{H,r,r}^{-1} \mathbf{J}_{H,r,\mathbf{R}} \right]^{-1}. \quad (5.28)$$

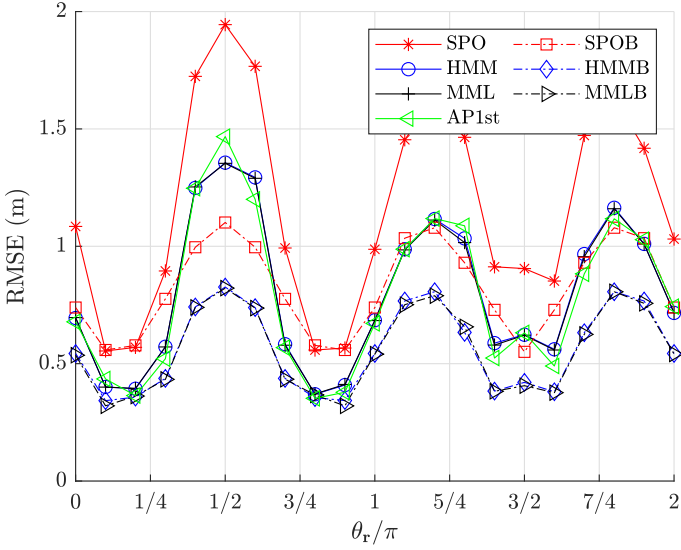
5.4 Numerical results

In the evaluation of the hybrid ML/MAP estimator and the theoretical lower bound in the presence of prior information on the orientation through computer simulations, we consider the same simulation setup (including the properties of environment, LEDs and the receiver) and the same path used in Chapter 4, as shown in Fig. 4.3.

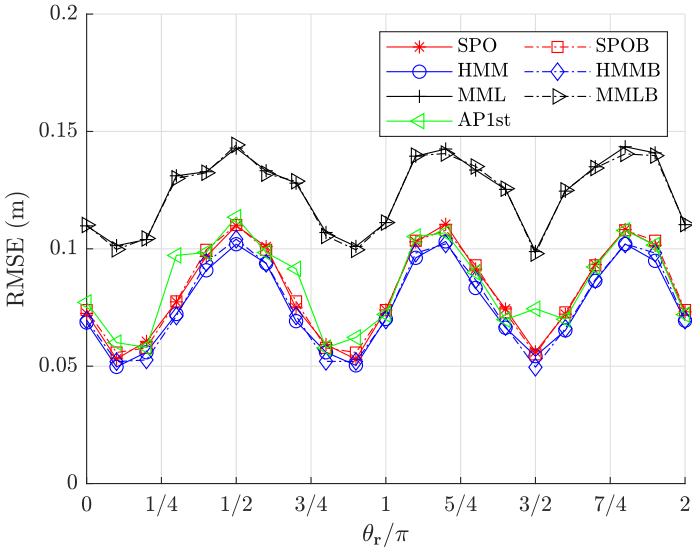
As the algorithms considered in this chapter require an iterative procedure, they need an initial estimate of the position and the orientation. For the HMM, MML and AP1st estimators, the initial estimate of the orientation comes from the external device, while for the position, we take as initial point the center of the area, i.e. $\hat{\Theta}^0 = \{\mathbf{b}/2, \tilde{\mathbf{R}}\}$. Similarly, the SPO algorithm considers as initial estimate of the position the center of the area. However, the SPO algorithm has no prior knowledge on the orientation. Therefore, we assume we have a coarse orientation estimator that estimates the orientation from the optical signal as e.g. described in the previous chapter. To have a fair comparison with the HMM and MML estimators, we assume this coarse estimator delivers a coarse estimate of the orientation that is Gaussian distributed around the true value of the orientation with variance $\sigma_0^2 = \sigma_e^2$, i.e., the SPO algorithm is initialized with $\hat{\Theta}^0 = \{\mathbf{b}/2, \hat{\mathbf{R}}^0\}$ with $\log(\hat{\mathbf{R}}^0 \mathbf{R}^{\text{T}})^{\vee} \sim \mathcal{N}(\mathbf{0}, \sigma_0^2 \mathbf{I}_3)$.

5.4.1 Performance of the hybrid ML/MAP Estimator

In Figs. 5.3 and 5.4, we show the root of the mean squared error (RMSE) of the position and orientation estimates of the proposed HMM estimator as a function of the position θ_r of the receiver in the elliptical path for SNR

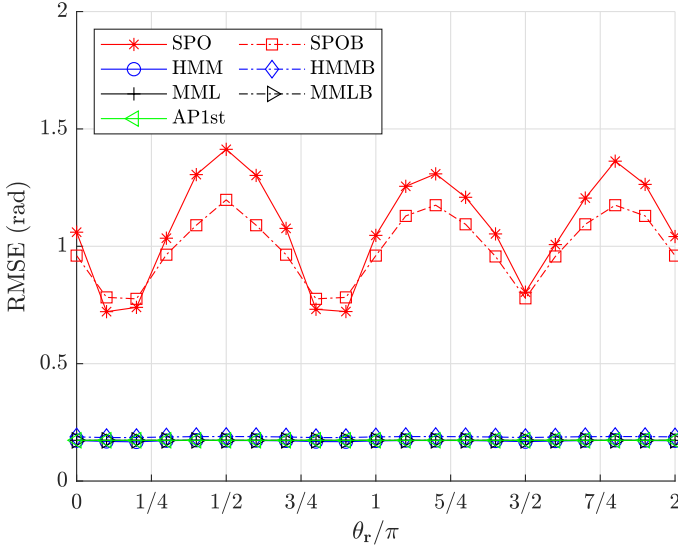


(a) Position estimation error, SNR = 15 dB

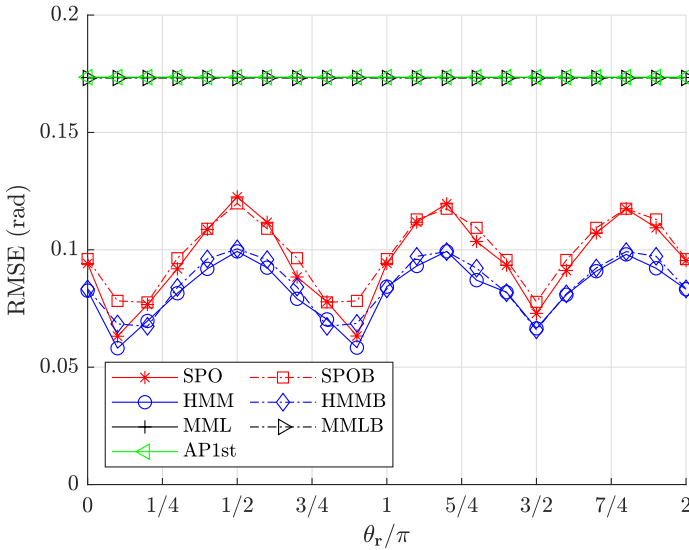


(b) Position estimation error, SNR = 35 dB

Figure 5.3: RMSE of the position as a function of the traveled angle θ_r along the elliptical path for $\sigma_\epsilon^2 = 1 \times 10^{-2} \text{ rad}^2$.



(a) Orientation estimation error, SNR = 15 dB



(b) Orientation estimation error, SNR = 35 dB

Figure 5.4: RMSE of the orientation as a function of the traveled angle θ_r along the elliptical path for $\sigma_\epsilon^2 = 1 \times 10^{-2} \text{ rad}^2$.

= 15 dB and SNR = 35 dB, respectively, and compare the resulting RMSE with the RMSE of the simultaneous position and orientation estimator (SPO), the misspecified maximum likelihood estimator (MML) and the first-order-approximation-based positioning algorithm (AP1st). Further, we show in the figure the root of the theoretical lower bound (HMMLB) from Section 5.3, and the root of the theoretical lower bounds for the SPO and MML estimators², denoted by SPOB and MMLB, respectively.

Let us first take a closer look at the behavior of the estimators and bounds as function of the traveled angle $\theta_{\mathbf{r}}$ along the elliptical path. The path we consider has a sinusoidal pattern in the Z direction, implying the distance between the receiver and the LED is relatively larger in the valleys of the path. At the same time, the path has an elliptical pattern in the XY plane. Taking into account the uniform distribution of the LEDs in the area, it is clear that the average distance between the LEDs and the receiver is the largest in the vertices. Hence, the largest average distance will occur at the vertex lying in a valley, i.e. for $\theta_{\mathbf{r}} = \pi/2$. Because the channel gain is inversely proportional to the distance between the receiver and the LEDs, a higher RMSE is expected at those points in the path that have a larger (average) distance between the receiver and the LEDs. This can be observed in Figs. 5.3 and 5.4, where the RMSE performance along the path shows a sinusoid-like pattern with three peaks and valleys, corresponding to the valleys and peaks in the path. As expected, the largest RMSE is obtained around $\theta_{\mathbf{r}} = \pi/2$, which corresponds to the vertex in the valley.

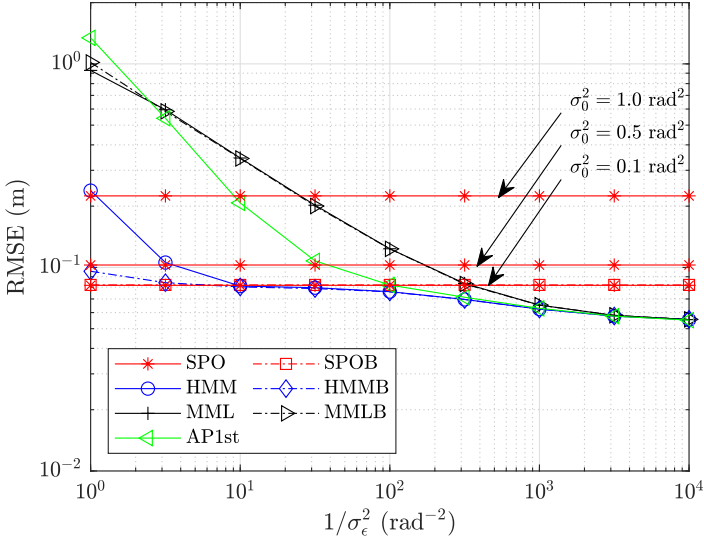
Next, we look at the performance of position estimation, as shown in Figs. 5.3a and 5.3b. As can be observed, for SNR = 15 dB, the MML, AP1st and HMM algorithms have similar positioning performance, while the SPO algorithm has a noticeable larger RMSE. On the other hand, when SNR = 35 dB, the HMM, AP1st and SPO algorithm have similar performance, and the MML algorithm has a noticeably larger RMSE. This can be explained as follows. On the one hand, when the SNR is low, it will be hard to extract reliable information about the position and orientation from the optical signal. A relatively accurate external estimate of the orientation, as available in the HMM and MML and AP1st estimators, can help to improve the position estimate. On the other hand, for larger SNR, reliable information about the position and orientation can be extracted from the optical signal, implying the performance will be less determined by the presence of a noisy prior estimate of the orientation. As the MML algorithm does not estimate the orientation from the optical signal, the effect of the misspecification of the orientation on the position estimate cannot be completely compensated by the reliable optical signal. In contrast, the SPO algorithm and HMM algorithm estimate the orientation both from the reliable optical signal, while the AP1st algorithm takes into account the orientation uncertainty. This explains the similar positioning performance of these latter algorithms. Comparing the RMSE performance of the algorithms

²The theoretical lower bound for the SPO estimator is given in the Chapter 4, while the bound for the MML estimator is discussed in Appendix C.

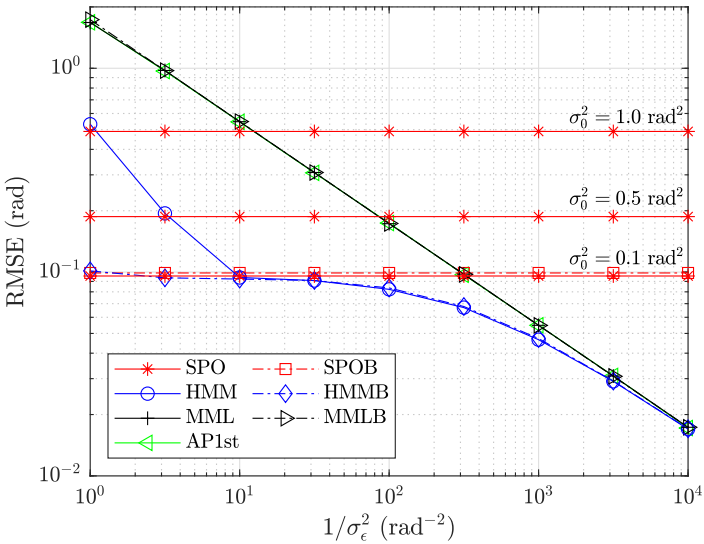
with their respective lower bounds, we see for $\text{SNR} = 15$ dB a gap between the RMSE and the lower bound, while for $\text{SNR} = 35$ dB, the RMSE is close to the lower bound. The reason for this is the asymptotic tightness of the CRB, i.e. the lower bound is tight when the SNR or the number of observations is sufficiently large.

Finally, we look at the performance of the orientation estimation, shown in Figs. 5.4a and 5.4b. As the performance of the external orientation estimator is independent of the position of the receiver and the optical signal, the RMSE of the MML and AP1st estimators will be constant over the whole path and independent of the SNR of the optical signal, i.e. the level of the RMSEs of MML and AP1st are the same for both Figs. 5.4a and 5.4b. Similarly, as for the position estimate, the RMSE of the HMM estimator is similar to that of the MML estimator for $\text{SNR} = 15$ dB and similar to that of the SPO estimator for $\text{SNR} = 35$ dB. For low SNR, the SPO estimator is not able to extract a reliable orientation estimate from the optical signal, yielding a worse RMSE than MML and HMM, while for larger SNR, the reliable optical signal allows the HMM and SPO estimator to obtain a more accurate orientation estimate than available with the external device, implying the MML and AP1st algorithms will have worse performance. Again, the explanation can be found in the reliability of the optical signal and the relative effect of the noisy prior estimate of the orientation at low and high SNR, similarly as for the position estimate. Also, for the orientation estimate, the lower bound is tight for sufficiently high SNR. As a conclusion, the proposed HMM estimator combines the best of both worlds: for low SNR as well as for high SNR, the RMSE of the proposed HMM estimator for both the position and orientation is at least as good or better than for the other algorithms, and operates close to optimal.

Now, we look at the effect of the variance σ_ϵ^2 of the orientation uncertainty. Fig. 5.5 shows the RMSE, averaged over the entire path, as a function of $1/\sigma_\epsilon^2$ for $\text{SNR} = 35$ dB. As the SPO algorithm does not use an orientation estimate from an external device, the performance of the SPO estimator is independent of σ_ϵ^2 , in contrast to the performance of the other estimators. The SPO performance only depends on the accuracy of the coarse orientation estimate, i.e., σ_0^2 . As can be observed in the figure, for large σ_0^2 , the SPO algorithm is not able to reach the theoretical lower bound. Due to the inaccuracy of the coarse estimate, the iterative algorithm in the SPO estimator is not able to converge properly to the correct position and orientation. From our simulations, we observed that the SPO algorithm converges correctly for a value of σ_0^2 up to 0.1 rad^2 . Let us now look closer at the dependency of the other estimators on the variance σ_ϵ^2 . First note that the MML and AP1st estimators do not estimate the orientation based on the optical signal. Hence, the RMSE of the orientation estimate is determined by the variance σ_ϵ^2 of the external orientation estimate. When the variance σ_ϵ^2 is large, i.e. $1/\sigma_\epsilon^2$ is small, the external orientation estimate is inaccurate. This will strongly reduce the positioning performance of the MML estimator, while the AP1st achieves a better positioning performance due to taking into account the orientation uncertainty. However, the inaccu-



(a) Position estimation error



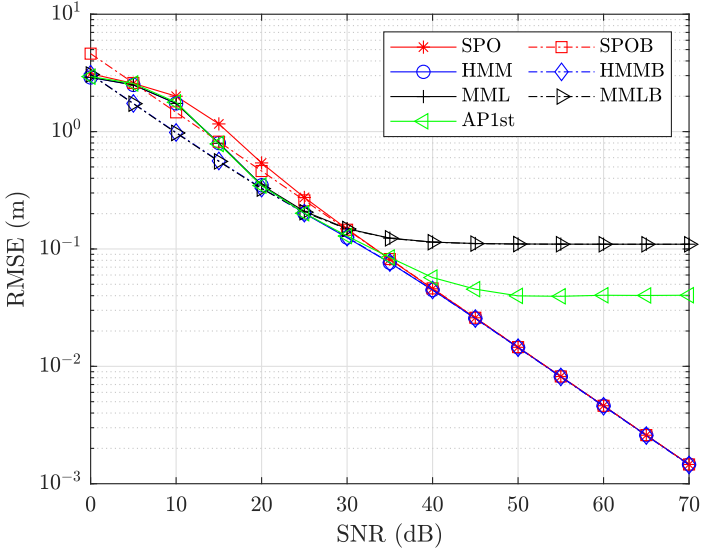
(b) Orientation estimation error

Figure 5.5: RMSE versus $1/\sigma_\epsilon^2$ for SNR = 35 dB.

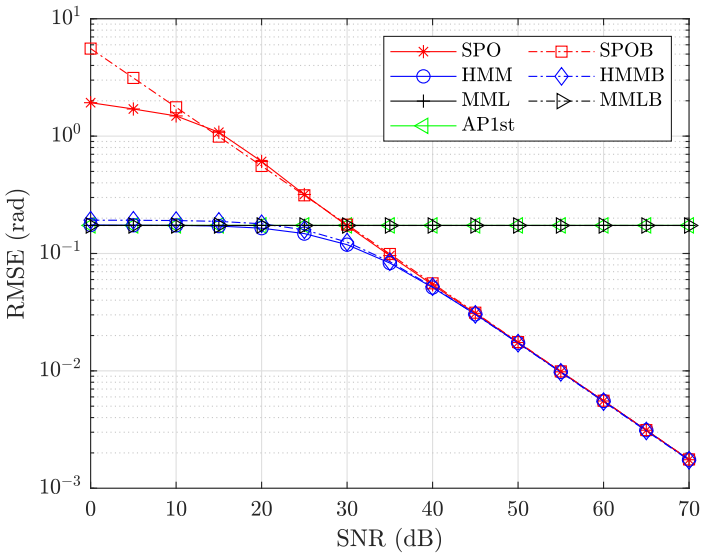
racy of the first-order approximation leads the AP1st to perform worse than HMM, and it even underperforms MML when σ_{ϵ}^2 becomes too large, implying the approximation becomes inaccurate and results in an incorrect position estimate. Comparing the lower bounds on the performance of the SPO and HMM algorithm, we observe that the theoretical performance of both estimators is similar. This could be expected as due to the unreliable external orientation estimate, the performance of the HMM estimator will be determined by the quality of the optical signal, similarly as for the SPO algorithm. On the other hand, when the variance σ_{ϵ}^2 is small, i.e. $1/\sigma_{\epsilon}^2$ is large, the external orientation estimate is accurate. In this case, the performance of the orientation estimate is mainly determined by the external estimator, implying the HMM, MML and AP1st estimators will have similar performance. The SPO algorithm is not able to achieve the same accuracy for the orientation based on the information contained in the optical signal, implying the performance of the SPO algorithm is degraded compared to other.

5.4.2 Asymptotic Tightness

In this section, we show that the proposed estimator is asymptotically tight with its lower bound for sufficiently large SNR or number of LEDs. In our simulations, we use the same path for the receiver as shown in Fig. 4.3, and the RMSE and associated root of the theoretical bound are averaged over the path. First, in Fig. 5.6, we show the averaged RMSE for the position and orientation, respectively, as a function of the SNR for $N_L = 24$ LEDs. The results show that the proposed HMM estimator is indeed asymptotically tight for large SNR. A similar asymptotic tightness is obtained with the SPO and MML estimators to their respective lower bounds. We observe that the MML and AP1st estimators show an error floor for large SNR. This is due to the presence of the bias mentioned in Appendix C, caused by the inaccurate external orientation estimate, while that of AP1st is due to the inaccuracy of the first-order approximation. On the other hand, the RMSE of the position and orientation errors for the SPO and HMM algorithms do not show an error floor. There, the RMSE for both types of errors reduces in inverse proportion to the SNR, i.e. the algorithms are able to estimate the position and orientation with high accuracy from the received optical signal. Next, we show in Fig. 5.7 the RMSE for positioning and orientation as a function of the number N_L of LEDs, for SNR = 35 dB. Also here, we see an asymptotic tightness between the RMSEs and their respective lower bounds. For a large number of LEDs, the RMSE and lower bound of the MML algorithm show an error floor, for the same reason as mentioned above. The results shown in Figs. 5.6 and 5.7 confirm that for large SNR or large N_L , the presence of the external estimate has no impact on the performance when the optical signal contains sufficient information to accurately estimate the position and orientation from the optical signal, i.e. SPO and HMM perform equally well. The improvement compared to the SPO algorithm is found when the optical signal is not sufficient to reliably estimate the orientation as well as the position, i.e. when there are not enough light

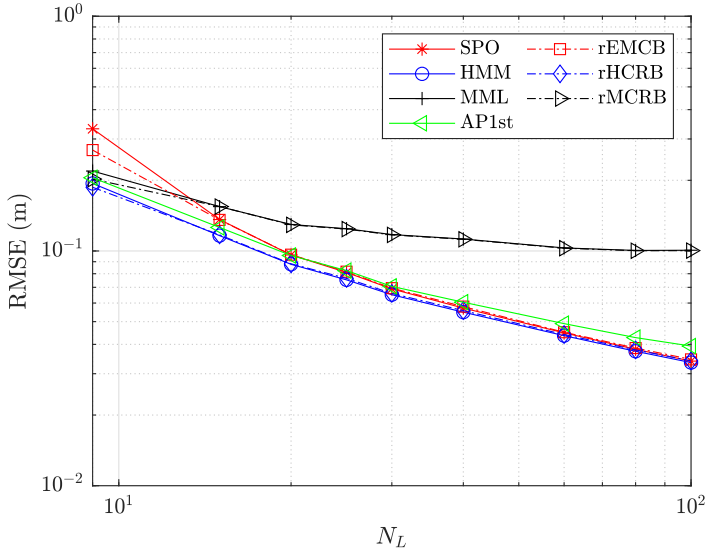


(a)

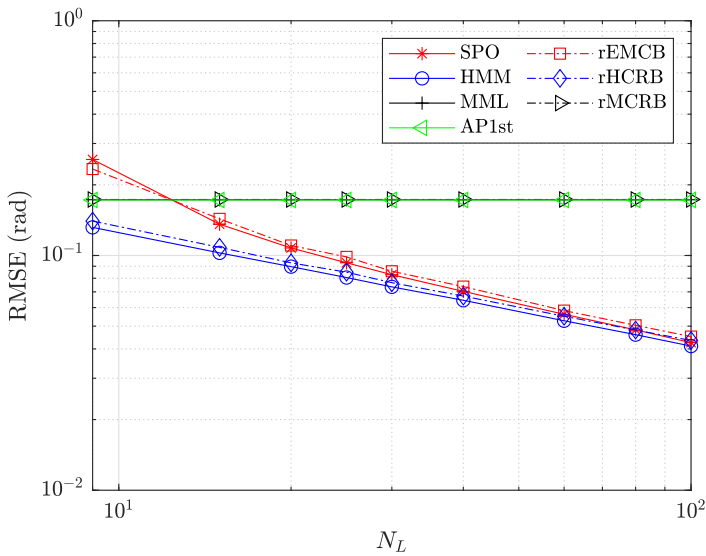


(b)

Figure 5.6: RMSE of position and orientation estimates versus SNR for $N_L = 24$.



(a)



(b)

Figure 5.7: RMSE of position and orientation estimates versus N_L for SNR = 35 dB.

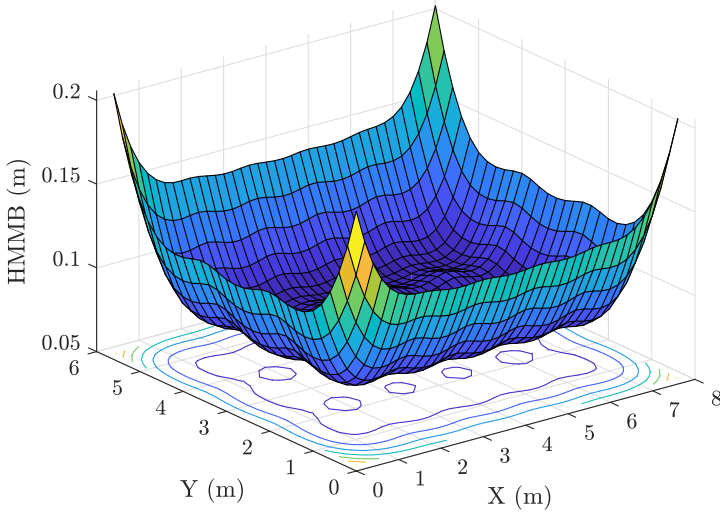
sources to cover the whole area, or when the SNR is too small.

5.4.3 Impact of Location of the Receiver

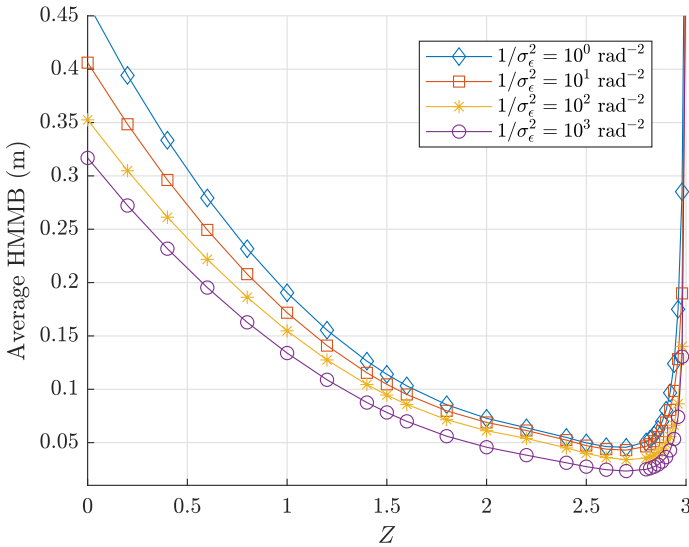
In this section, we investigate the performance of the proposed receiver as a function of the position of the receiver. We consider the same room setup as illustrated in Fig. 4.3. Further, we assume the receiver is pointing upwards, the variance $1/\sigma_{\epsilon}^2 = 1 \times 10^2 \text{ rad}^{-2}$ and $\text{SNR} = 35 \text{ dB}$. In the first simulation, we assume the height of the receiver is fixed at $z = 1.5 \text{ m}$, i.e. at a vertical distance of 1.5 m from the floor, and compute the HCRB as a function of the position of the receiver in the XY plane. Figs. 5.8a and 5.9a show the root of the HCRB, denoted as HMMB, for the position error and the orientation error, respectively. The HMMB has an inverted dome shape, where in the largest part of the area the HMMB is low and only shows some small fluctuations, and at the edges of the area, the HMMB is strongly degraded. This effect is due to the limited FOV of the receiver, as the closer the receiver is to the side boundary, the less LEDs it will sense. Next, we consider the effect of the vertical distance Z between the floor and the receiver. The root of the HRCB, i.e. HMMB, averaged over the XY plane, is shown as function of the vertical distance Z in Figs. 5.8b and 5.9b. As can be observed, when the height Z increases, the HMMB improves as the distance between the LEDs and the receiver reduces. However, because the incidence angles become relatively larger when the vertical distance between the LEDs and the receiver reduces, the incident angles may grow too large, implying the LEDs will start to fall out of the FOV of the receiver. This explains the strong increase of the HMMB when the height approaches the maximum height of 3 m, although the effect on the orientation HMMB is smaller, especially when more reliable prior information on the orientation is available.

5.5 Conclusion

In this chapter, we investigated RSS-based hybrid position and orientation estimation for a visible light system with multiple LEDs and multiple PDs in the presence of possibly unreliable prior information on the orientation. We first constructed the channel gain model of the multiple LEDs – multiple PDs system and discussed the model used for the orientation uncertainty. We designed a RSS-based position and orientation estimation algorithm based on the hybrid ML/MAP principle, converted the optimization problem into a NLS problem and solved it with an iterative algorithm based on the Gauss-Newton method on manifolds. To investigate the optimality of the proposed estimator, we derived the theoretical lower bound for the hybrid ML/MAP estimator. We verified that the RMSE of the proposed estimator asymptotically approaches this theoretical bound for sufficiently large SNR and number of LEDs. Further, we also compared the performance of the proposed estimator with two state-of-the-art estimators, i.e., the SPO, the MML and the AP1st

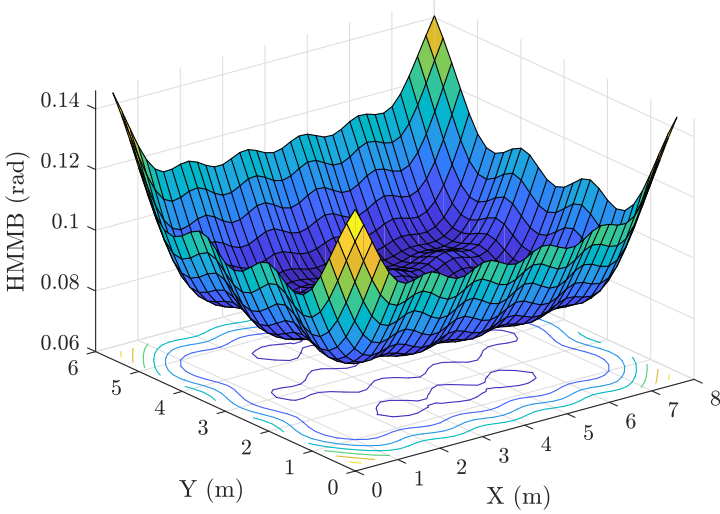


(a) Rooted bound on position error for the XY plane fixed at 1.5 m in z -axis

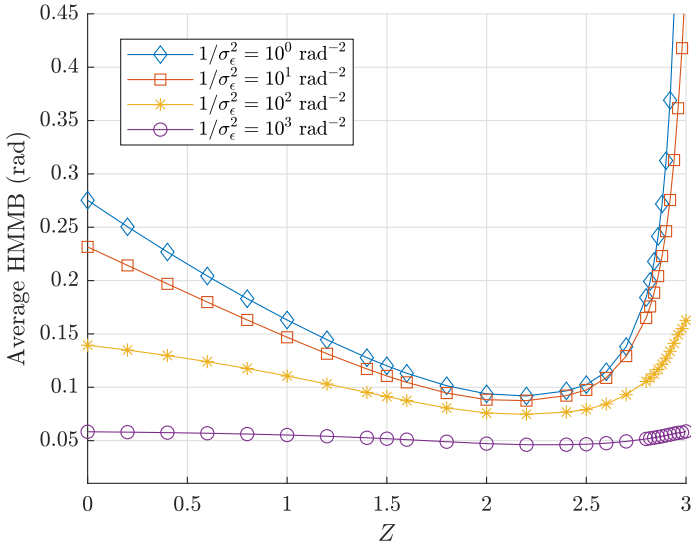


(b) The root of the bound on position error as a function of the height, averaged over the XY plane.

Figure 5.8: The root of theoretical lower bound as a function of the position of the receiver.



(a) Rooted bound on orientation error for the XY plane fixed at 1.5 m in z-axis



(b) The root of the bound on orientation error as a function of the height, averaged over the XY plane.

Figure 5.9: The root of theoretical lower bound as a function of the position of the receiver.

estimator, and found that the proposed estimator performs well over the whole range of the orientation uncertainty, in contrast to the other estimators. The studies mentioned in this chapter were published partly in [26] and presented partly in [73].

6

Simultaneous Position and Orientation Estimation for the Aperture-Combined Quadrant Photodiode

While in chapters 4 and 5, we considered the angular diversity receiver from Section 2.4.1, in this chapter we will use the aperture-combined receiver from Section 2.4.2 and investigate its SPO estimation. In this receiver, an aperture must be placed at a certain distance above the quadrant photodiode (QPD), and the center of the aperture must be aligned with the center of the QPD. However, in practice, perfect alignment between the aperture and quadrant photodiode is not possible. The resulting misalignment, if not dealt with properly, may cause significant errors in the PO estimate. Therefore, we also consider a procedure to calibrate the receiver. To this end, we first model the RSS of the aperture-combined quadrant photodiode (AQPD) as a function of the receiver's PO and misalignment. Then, we show that the commonly applied strategy of differencing and normalization to the RSS, claimed by most works to improve the robustness against RSS variation, results in a complex PDF, which makes an effective and efficient estimation hard to achieve. Therefore, we derive an approximated PDF in a simple closed-form, based on which the calibration and the SPO estimation algorithms using the least squares principle are proposed. The proposed calibration does not require any information about the PO of the receiver and is robust to the received power variation. We also derive the corresponding theoretical lower bound on the misalignment to benchmark the performance of the misalignment, and also to serve as an indicator to determine the required signal-to-noise ratio (SNR) or number of LEDs to obtain a desired accuracy. The calibration and SPO estimation are evaluated by means of Monte Carlo simulation and experimentally, and in both approaches, the effectiveness of the proposed algorithms is confirmed.

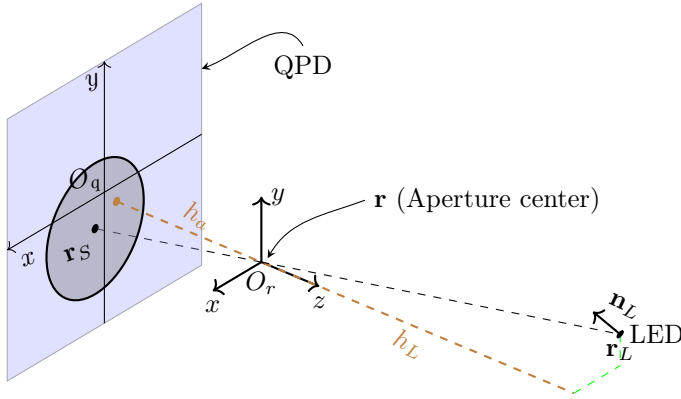


Figure 6.1: The channel link model of AQPd. The position of the LED and centers of the aperture and the light spot comply with the perspective projection model, while the shape and size of the light spot is determined by the aperture.

6.1 A New Look at the Channel Model

We note that the dependency of the RSS values on the PO is twofold. Firstly, the channel gain is determined by the radiation pattern of the LED and the irradiance attenuation, implying the incident power at the QPD (and thus the optical power in the light spot) depends on the relative position of the light spot with respect to the LED. Secondly, the RSS values in the quadrants are proportional to the overlap areas of the light spot with the quadrants of the QPD, which is determined by the position of this light spot with respect to the center of the QPD. In order to simplify the estimation, we assume that the light spot overlaps with all quadrants and completely falls within the active area of the QPD¹. To ensure that the first condition is fulfilled, we assume the receiver adopts a detection algorithm that only focuses on LEDs that lead all quadrants to produce a high RSS output. The second condition implies that the aperture diameter is upper limited by (roughly) the dimension of a quadrant, i.e. half the diameter of a circular QPD or half the side of a square QPD. This guarantees a simple unique relationship between the 4-tuple of RSS values generated by the QPD and the PO of the receiver, and by combining the information from different light sources satisfying the above conditions, the PO of the receiver can easily be determined.

To determine the overlap areas of the light spot and the QPD, we define a second coordinate system attached to the receiver (besides the receiver frame given in Section 2.4.2). The second receiver attached coordinate system is the

¹In case the light spot does not overlap with all quadrants, one or more of the RSS values will be zero. This will obstruct the strategy of differencing and normalization of the RSS values, which is used to make the estimation algorithm robust against variations in the transmitted optical power. In case the light spot partially falls off the QPD, the relationship between the RSS values and the PO of the receiver becomes very complex, implying the resulting estimation algorithm will have high complexity.

QPD frame, where the $x - y$ plane is the surface of the QPD, the origin O_q is placed in the center of the QPD, and the x and y axes are aligned with the gaps between the quadrants. In this chapter, we assume that the aperture plane is parallel to the plane of the QPD and the x - and y -axes of the QPD and receiver frames are aligned. This implies that the transformation of vectors in the aperture frame into vectors in the QPD frame is a simple translation. In the following, we will determine the coordinates of the light spot generated by a LED.

To calculate the position of the light spot in the QPD frame, we notice that the line going through the position \mathbf{r}_L of the LED and the centers \mathbf{r} of the aperture and $\mathbf{r}_S \in \mathbb{R}^{3 \times 1}$ of the light spot can be seen as a ray in the perspective projection model of a virtual pinhole located at the center of the aperture and having focal length equal to the aperture height $|h_a|$, i.e. the distance between the planes of the aperture and the QPD (see Fig. 6.1). In this virtual pinhole model, the LED can be seen as a virtual 'object' and the center of the light spot as the projected virtual 'image'. The perspective projection model allows us to relate the 3D coordinates of the LED – the 'object' – in the system frame to the 2D coordinates of the light spot – the 'image' – in the QPD frame². Taking this into account and using the projection principle, the position $\mathbf{r}_{S,q} \in \mathbb{R}^{2 \times 1}$ of the center of the light spot in the QPD frame is given by [65, eq. (6.5)]:

$$\mathbf{r}_{S,q} = \mathbf{k}_{m,q} + \underbrace{\left[\begin{array}{c} \mathbf{e}_1^T \\ \mathbf{e}_2^T \end{array} \right]}_{\text{C}} \underbrace{\left[\mathbf{I}_3, \mathbf{0} \right]}_{\text{B}} \underbrace{\frac{h_a}{\mathbf{e}_3^T \mathbf{T} \bar{\mathbf{r}}_L} \underbrace{\mathbf{T} \bar{\mathbf{r}}_L}_{\text{A}}}_{\text{A}}. \quad (6.1)$$

In (6.1), \mathbf{e}_i is a unit basis vector with its i^{th} element being 1, and the operator $\bar{\cdot}$ converts the Cartesian coordinates \mathbf{x} into the homogeneous coordinates $\bar{\mathbf{x}} = [\mathbf{x}^T, 1]^T$. The matrix $\mathbf{T} \in SE(3)$ belongs to the Special Euclidean group $SE(3)$, and is defined through its inverse

$$\mathbf{T}^{-1} = \begin{bmatrix} \mathbf{R} & \mathbf{r} \\ \mathbf{0}_{1 \times 3} & 1 \end{bmatrix} \in SE(3). \quad (6.2)$$

Further, the misalignment vector $\mathbf{k}_{m,q}$ expresses the errors in the alignment of the aperture with respect to the QPD. Due to construction errors, a small horizontal offset between the origins of the QPD frame and the receiver frame may occur. This is illustrated in Fig. 6.1, where the brown dot does not coincide with the center O_q of the QPD. The horizontal misalignment vector, which takes into account this offset in the transformation of the light spot coordinates in the receiver frame to the coordinates in the QPD frame, is defined as $\mathbf{k}_{m,q} \doteq [u_m, v_m]^T$, with u_m and v_m the misalignment in the x and y direction, respectively. Taking into account (6.1), we see that the projection principle consists of three steps:

²Note that the position of the light spot in the QPD frame is specified by the (x, y) coordinates only.

- Step A: This step converts the LED coordinates $\bar{\mathbf{r}}_L$ in the system frame to the coordinates $\bar{\mathbf{r}}_{L,r} = \mathbf{T}\bar{\mathbf{r}}_L$ in the receiver frame using the matrix \mathbf{T} .
- Step B: This scales $\bar{\mathbf{r}}_{L,r}$ along the projection line with the factor $\frac{h_a}{h_L}$ where $h_L = \mathbf{e}_3^T \mathbf{T}\bar{\mathbf{r}}_L$ and gets rid of the last component of the homogeneous coordinates through the 3×4 matrix $[\mathbf{I}_3, \mathbf{0}]$, consisting of the 3×3 identity matrix extended with a zero column, as this last component is irrelevant for the determination of the position of the light spot. This results in the position $\mathbf{r}_{S,r} = [\mathbf{I}_3, \mathbf{0}] \frac{h_a}{\mathbf{e}_3^T \mathbf{T}\bar{\mathbf{r}}_L} \bar{\mathbf{r}}_{L,r}$ of the light spot in the receiver frame.
- Step C: This transforms $\mathbf{r}_{S,r}$ into the 2D coordinates $\mathbf{r}_{S,q}$ by discarding the z coordinate through the mapping of $\mathbf{r}_{S,r}$ on the 2×3 matrix $\begin{bmatrix} \mathbf{e}_1^T \\ \mathbf{e}_2^T \end{bmatrix}$, and adds the misalignment vector $\mathbf{k}_{m,q}$.

Equation (6.1) can be rewritten the following compact form:

$$\mathbf{r}_{S,q} = \frac{\mathbf{K}\mathbf{T}\bar{\mathbf{r}}_L}{\mathbf{e}_3^T \mathbf{T}\bar{\mathbf{r}}_L}, \quad (6.3)$$

The matrix \mathbf{K} , which is used in the perspective projection model, is called the intrinsic parameter matrix and describes the internal properties of a receiver, i.e. that are independent of the PO. It only depends on the misalignment vector $\mathbf{k}_{m,q}$ and the aperture height h_a :

$$\mathbf{K} = \begin{bmatrix} h_a & 0 & u_m & 0 \\ 0 & h_a & v_m & 0 \end{bmatrix}, \quad (6.4)$$

On the other hand, the matrix \mathbf{T} contains the PO information of the receiver and is independent of the internal properties of the receiver. Therefore, it is called the extrinsic parameter matrix. Similarly, taking into account (6.1), we can write the position $\mathbf{r}_{S,r}$ of the center of the light spot in the receiver frame (in homogeneous coordinates) in the following compact form:

$$\bar{\mathbf{r}}_{S,r} = \frac{\mathbf{K}_0 \mathbf{T}\bar{\mathbf{r}}_L}{\mathbf{e}_3^T \mathbf{T}\bar{\mathbf{r}}_L} \quad \text{with} \quad \mathbf{K}_0 = \begin{bmatrix} h_a \mathbf{I}_3 & \mathbf{0} \\ \mathbf{e}_3^T & 0 \end{bmatrix}. \quad (6.5)$$

and the position $\bar{\mathbf{r}}_S$ of the light spot in the system frame (in homogeneous coordinates) is obtained through:

$$\bar{\mathbf{r}}_S = \mathbf{T}^{-1} \bar{\mathbf{r}}_{S,r} \quad (6.6)$$

To determine the RSS values in the quadrants of the QPD, we first need to compute the overlap area between the light spot and the quadrants of the QPD. Let us assume the aperture has radius l . Taking into account we already assumed that the light spot completely overlaps with the QPD, i.e. no part of the light spot falls outside the QPD, and that all quadrants overlap with the light spot, the overlap areas can easily be computed based on the position $\mathbf{r}_{S,q}$ of the center of the light spot in the frame of the QPD. Defining the overlap

area $A_i > 0$ of the i th quadrant, $i = 1, \dots, 4$ and the angles $\alpha_j \in [0, \pi]$ with $[\mathbf{r}_{S,q}]_j = l \cos \alpha_j$, $j = 1, 2$, and the operator $[\mathbf{r}_{S,q}]_j$ as the j th element of $\mathbf{r}_{S,q}$ (see Fig. 2.12), we obtain the overlap areas by solving the following set of equations:

- The light spot has area πl^2 , implying $A_1 + A_2 + A_3 + A_4 = \pi l^2$.
- Taking into account that the area of a circular segment with central angle 2α , $\alpha \in [0, \pi]$ equals $\frac{l^2}{2}(2\alpha - \sin 2\alpha)$, we find that $A_2 + A_3 = (\alpha_1 - \sin \alpha_1 \cos \alpha_1)l^2$ and $A_3 + A_4 = (\alpha_2 - \sin \alpha_2 \cos \alpha_2)l^2$.
- The overlap area A_1 with the first quadrant is a combination of a circle sector with central angle $\frac{3\pi}{2} - (\alpha_1 + \alpha_2)$ having an area $(\frac{3\pi}{2} - (\alpha_1 + \alpha_2)) \frac{l^2}{2}$, a rectangle with area $[\mathbf{r}_{S,q}]_1 [\mathbf{r}_{S,q}]_2 = l^2 \cos \alpha_1 \cos \alpha_2$ and two triangles with areas $\frac{l^2}{2} \cos \alpha_j \sin \alpha_j$, $j \in \{1, 2\}$.

Note that, depending whether $\cos \alpha_j > 0$ (if $\alpha_j \in [0, \frac{\pi}{2}]$) or $\cos \alpha_j < 0$ (if $\alpha_j \in [\frac{\pi}{2}, \pi]$), the above contributions will combine positively or negatively, resulting in the wanted overlap area A_i . Hence, the overlap area vector $\mathbf{A} = [A_1, \dots, A_4]^T$ is the solution of $\mathbf{M}_a \mathbf{A} = \mathbf{s}$ with

$$\mathbf{M}_a = \begin{bmatrix} 1 & 0 & 0 & 0 \\ 0 & 1 & 1 & 0 \\ 0 & 0 & 1 & 1 \\ 1 & 1 & 1 & 1 \end{bmatrix} \quad (6.7)$$

and

$$\mathbf{s} = l^2 \begin{bmatrix} \frac{3\pi}{4} - \frac{\alpha_1 + \alpha_2}{2} + \frac{\sin 2\alpha_1 + \sin 2\alpha_2}{4} + \cos \alpha_1 \cos \alpha_2 \\ (\alpha_1 - \sin \alpha_1 \cos \alpha_1) \\ (\alpha_2 - \sin \alpha_2 \cos \alpha_2) \\ \pi \end{bmatrix}. \quad (6.8)$$

Now that we obtained the overlap areas of the light spot with the PDs of the QPD, and related them to the PO of the receiver, the RSS values in the different PDs can be determined. Taking in account the equalities $[\mathbf{n}_Q^T, 0]^T = \mathbf{T}^{-1} \mathbf{e}_3$, obtained from (6.2), the channel gain vector (2.21) can be rewritten as

$$\mathbf{h}(\mathbf{k}, \mathbf{T}) = -\frac{(\gamma + 1) \Pi_{\phi, \theta} (\mathbf{n}_L^T \mathbf{v})^\gamma (\mathbf{T}^{-1} \mathbf{e}_3)^T \bar{\mathbf{v}}}{2\pi \|\mathbf{v}\|^{\gamma+3}} \mathbf{A}, \quad (6.9)$$

and is a function of the intrinsic parameter vector $\mathbf{k} \doteq [u_m, v_m, h_a]^T$ and the PO \mathbf{T} . From this channel gain, we obtain the RSS output vector $\mathbf{y} = [y_1, \dots, y_4]^T$ in the four PDs:

$$\mathbf{y} = \mathbf{g} + \boldsymbol{\eta} \quad (6.10)$$

where $\mathbf{g} = R_p P_t \mathbf{h}$, with R_p the responsivity of the QPD, and P_t the transmitted power. Due to coupling between the quadrants, the noise components are correlated Gaussian distributed random variables $\boldsymbol{\eta} \sim \mathcal{N}(\mathbf{0}, \sigma_\eta^2 \mathbf{C})$, where \mathbf{C} is the correlation matrix with $\mathbf{C}_{i,i} = 1$ and $\mathbf{C}_{i,j} = \rho$ if $i \neq j$, ρ is the correlation between the noise of different quadrants, and σ_η^2 is the noise variance.

In the derivation of \mathbf{g} in (6.10), it is assumed that the transmitted optical power is perfectly known and the LED is a perfect Lambertian radiator. However, directly estimating the intrinsic and/or extrinsic parameters from the RSS output vector will result in inaccurate estimates. To make the estimator more robust to changes in the incident power, [41, 74] proposed to use the normalized differences between the RSS values along the two axes to detect laser beams:

$$\begin{cases} t_x = \frac{(y_1+y_4)-(y_2+y_3)}{y_1+y_2+y_3+y_4} \\ t_y = \frac{(y_1+y_2)-(y_3+y_4)}{y_1+y_2+y_3+y_4} \end{cases}, \quad (6.11)$$

and the same idea is followed by [34] for VLP. The approach (6.11) will make the observations insensitive to variations in the transmitted optical power and radiation pattern provided that the RSS values are noise-free, so that the normalized differences of (6.11) is a noiseless observation. While this noise-free assumption is approximately true in the laser application, the noise induced by ambient light in visible light systems is non-negligible. The presence of the noise will have an impact on the distribution of t_x and t_y . As the estimation of the intrinsic and extrinsic parameters relies on proper knowledge of this distribution, we need to evaluate the effect of the noise on the distribution to see if the observations (6.11) are still insensitive to variations in the transmitted power when noise is present. Therefore, in the following section, we will analyze the distribution of the normalized differences t_x and t_y .

6.1.1 Approximating the PDF of the Observation

In order to find the distribution of the normalized differences, we first rewrite the numerator and denominator of t_x and t_y in a more compact form by introducing $\mathbf{m} \doteq [m_1, m_2, m_3]^T = \mathbf{M}_y \mathbf{g}$ and $\mathbf{w} \doteq [w_1, w_2, w_3]^T = \mathbf{M}_y \boldsymbol{\eta}$ with

$$\mathbf{M}_y = \begin{bmatrix} 1 & -1 & -1 & 1 \\ 1 & 1 & -1 & -1 \\ 1 & 1 & 1 & 1 \end{bmatrix}, \quad (6.12)$$

implying (6.11) can be rewritten as $\mathbf{t} = \begin{bmatrix} m_1+w_1 & m_2+w_2 \\ m_3+w_3 & m_3+w_3 \end{bmatrix}^T$. Taking into account that the components of \mathbf{w} are linear combinations of Gaussian distributed random variables, \mathbf{w} has a multivariate normal distribution, i.e. $\mathbf{w} \sim \mathcal{N}(\mathbf{0}, \boldsymbol{\Sigma}_w)$ with

$$\boldsymbol{\Sigma}_w = 4\sigma_\eta^2 \begin{bmatrix} 1-\rho & 0 & 0 \\ 0 & 1-\rho & 0 \\ 0 & 0 & 1+3\rho \end{bmatrix}. \quad (6.13)$$

Note that the numerator $(m_3 + w_3) = \sum_i y_i$ corresponds to the sum of the RSS values in the different quadrants. Hence, m_3 and $\sigma_{w_3}^2 \doteq 4(1 + 3\rho)\sigma_\eta^2$ are the average and variance of the total received signal strength, which implies we can define $\xi \doteq m_3^2/\sigma_{w_3}^2$ as the received signal-to-noise ratio (SNR) at the receiver. Further, we define

$$\boldsymbol{\mu} \doteq \begin{bmatrix} m_1 & m_2 \\ m_3 & m_3 \end{bmatrix}^T, \quad (6.14)$$

i.e. the ratio of the averages of the denominator and numerator of \mathbf{t} . Obviously, in the absence of noise, the observation equals $\mathbf{t} = \boldsymbol{\mu}$. We will show that:

- $\boldsymbol{\mu}$ is independent of the channel gain parameters and the transmitted power.
- At high SNR, the distribution of \mathbf{t} is given by $\mathbf{t} \sim \mathcal{N}(\boldsymbol{\mu}, \boldsymbol{\Sigma})$ with

$$\boldsymbol{\Sigma} = \xi^{-1} \left(\frac{1-\rho}{1+3\rho} \mathbf{I}_2 + \boldsymbol{\mu} \cdot \boldsymbol{\mu}^T \right). \quad (6.15)$$

Let us first take a closer look at the dependency of $\boldsymbol{\mu}$ on the channel gain and the transmitted power. Defining $\mathbf{h}(\mathbf{k}, \mathbf{T}) = \lambda \mathbf{A}$, and taking into account that the factor λ is independent of the considered quadrant, it follows that $\boldsymbol{\mu}$ is independent of the channel gain parameters and the transmit power contained in the factor λ , but only depends on \mathbf{A} . Substituting the solution of $\mathbf{M}_a \mathbf{A} = \mathbf{s}$ in (6.14), we find after some straightforward computations that

$$[\boldsymbol{\mu}]_i = \left(1 - \frac{2(\alpha_i - \cos \alpha_i \sin \alpha_i)}{\pi} \right). \quad (6.16)$$

Hence, the vector $\boldsymbol{\mu}$ solely depends on the angles α_i that are determined by the coordinates of the center of the light spot in the QPD frame. These coordinates, and therefore also $\boldsymbol{\mu}$, only depend on the intrinsic and extrinsic parameters through (6.3) but not on the channel gain parameters nor the transmit power.

To obtain the distribution of \mathbf{t} at high SNR, we first notice that $t_x = \frac{m_1+w_1}{m_3+w_3}$ and $t_y = \frac{m_2+w_2}{m_3+w_3}$ are both a ratio of two independent normal variables with non-zero means, and as they share the same denominator, they are correlated. The distribution of a single ratio of normal variables has been investigated in the literature, e.g., [75, 76, 77]. In these works, it is shown that a closed-form expression for the PDF in the general case for such a ratio is very complex as its shape differs significantly with its parameters, i.e. in some cases it resembles the Cauchy distribution, in other cases a normal distribution or a bimodal distribution. Several closed-form approximations were discussed in the literature, e.g. the approximate normal distribution. In this chapter, we need the distribution of two correlated ratios of normal variables. As this is an even more complicated situation compared to the single ratio case, it is clear that the closed-form expression for the PDF will be even more complex. To simplify the analysis, we first notice that at high SNR, $\frac{w_i}{m_3} \ll 1$. Expanding \mathbf{t} with respect to \mathbf{w} using the Taylor series, keeping up to the linear terms in \mathbf{w} , we obtain:

$$\mathbf{t} \approx \boldsymbol{\mu} + \mathbf{M}_w \mathbf{w} \quad \text{with} \quad \mathbf{M}_w = \begin{bmatrix} \frac{1}{m_3} & 0 & -\frac{m_1}{m_3} \\ 0 & \frac{1}{m_3} & -\frac{m_2}{m_3} \end{bmatrix}. \quad (6.17)$$

This first-order approximation directly leads to the distribution $\mathbf{t} \sim \mathcal{N}(\boldsymbol{\mu}, \boldsymbol{\Sigma})$ with $\boldsymbol{\Sigma} = \mathbf{M}_w \boldsymbol{\Sigma}_w \mathbf{M}_w^T$. Substituting \mathbf{M}_w and $\boldsymbol{\Sigma}_w$ (6.13) in $\boldsymbol{\Sigma}$, and using the definition of the SNR ξ , it follows that the covariance matrix $\boldsymbol{\Sigma}$ reduces to (6.15).

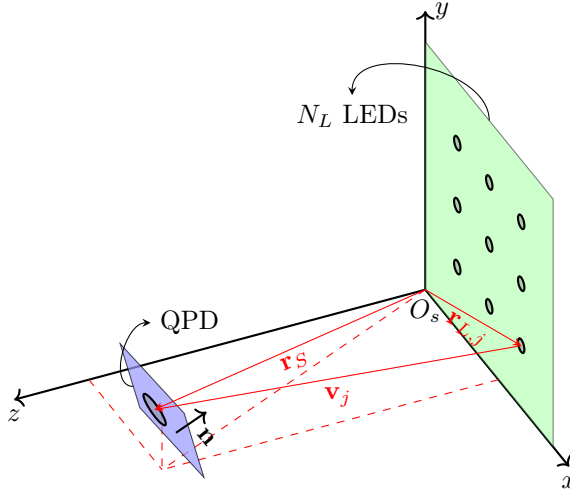


Figure 6.2: System frame for calibration.

6.2 Calibration System and SPO Estimation

Using the approximate PDF of the normalized differences, derived in the previous section, we can now estimate the PO of the receiver taking into account the relations (6.14) and (6.16). When the intrinsic parameters are known, the estimation of the PO, i.e. the extrinsic parameters, is straightforward. However, in practice, the intrinsic parameters are not prior known, and need to be estimated because inaccurate knowledge of the misalignment parameters may result in significant biases in the PO estimates. As these intrinsic parameters can be considered fixed once the receiver is assembled, the intrinsic parameters can be determined once during a calibration process. The standard approach is to determine the intrinsic parameters assuming the PO of the receiver is known. However, this approach requires accurate knowledge of the PO of the receiver. Although it is possible to accurately determine the PO of the receiver, this requires costly equipment, in particular to determine the orientation of the receiver, and a laborious procedure to determine the PO of the receiver before each measurement. Therefore, we propose in this section a method to estimate the intrinsic parameters not requiring the knowledge of the PO, making it simpler and less costly than the standard calibration procedure.

6.2.1 Calibration Procedure

The calibration procedure proposed in this chapter makes use of the setup shown in Fig. 6.2, where N_L LEDs are installed on a plane in the system frame $xO_s y$ and the positions of these LEDs are fixed and known. The receiver observes these LEDs at N_T different POs. Hence, the receiver observes for each

LED N_T 4-tuples of RSS values. The resulting observations are arranged in the $4N_T N_L \times 1$ vector $\check{\mathbf{y}} \in \mathbb{R}^{4N_T N_L \times 1}$:

$$\check{\mathbf{y}} = \check{\mathbf{g}} + \check{\boldsymbol{\eta}} \quad (6.18)$$

where the vector $\check{\boldsymbol{\eta}} \sim \mathcal{N}(\mathbf{0}, \check{\boldsymbol{\Sigma}}_{\boldsymbol{\eta}})$ collects the noise, and $\check{\boldsymbol{\Sigma}}_{\boldsymbol{\eta}} = \sigma_{\boldsymbol{\eta}}^2 \mathbf{I}_{N_T N_L} \otimes \mathbf{C}$ (see Section 6.1 for the definition of the noise correlation matrix \mathbf{C}). The vector $\check{\mathbf{g}}$ can be rewritten as $\check{\mathbf{g}} = R_p [P_{t,1} \mathbf{g}_{1,1}^T, P_{t,2} \mathbf{g}_{1,2}^T, \dots, P_{t,N_L} \mathbf{g}_{N_T, N_L}^T]^T$, where $\mathbf{g}_{i,j} \in \mathbb{R}^{4 \times 1}$ is the channel gain between the j^{th} LED and the receiver at the i^{th} PO \mathbf{T}_i^{-1} , and $P_{t,j}$ is the transmitted power of the j^{th} LED. For each LED and each PO, we compute the normalized differences and arrange them in the $2N_T N_L \times 1$ vector $\check{\mathbf{t}} \in \mathbb{R}^{2N_T N_L \times 1}$. Taking into account that the noise in the different observations is statistically independent, we can write the Gaussian approximation of the PDF of $\check{\mathbf{t}}$ as:

$$p_m(\check{\mathbf{t}}) = \frac{1}{\sqrt{\det(2\pi\check{\boldsymbol{\Sigma}})}} \exp\left(-\frac{1}{2} \|\check{\mathbf{t}} - \check{\boldsymbol{\mu}}\|_{\check{\boldsymbol{\Sigma}}}^2\right) \quad (6.19)$$

where $\|\mathbf{x}\|_{\check{\boldsymbol{\Sigma}}}^2 = \mathbf{x}^T \check{\boldsymbol{\Sigma}}^{-1} \mathbf{x}$ is the squared Mahalanobis distance with respect to covariance matrix $\check{\boldsymbol{\Sigma}}$, and $\check{\boldsymbol{\mu}} = [\boldsymbol{\mu}_{1,1}^T, \boldsymbol{\mu}_{1,2}^T, \dots, \boldsymbol{\mu}_{N_T, N_L}^T]^T$. The components $\boldsymbol{\mu}_{i,j}$ correspond to the j^{th} LED and the i^{th} PO, and are defined through (6.14), while the covariance matrix $\check{\boldsymbol{\Sigma}}$ is given by

$$\check{\boldsymbol{\Sigma}} = \begin{bmatrix} \boldsymbol{\Sigma}_{1,1} & \mathbf{0} & \mathbf{0} \\ \mathbf{0} & \ddots & \mathbf{0} \\ \mathbf{0} & \mathbf{0} & \boldsymbol{\Sigma}_{N_T N_L, N_T N_L} \end{bmatrix}. \quad (6.20)$$

In this covariance matrix, $\boldsymbol{\Sigma}_{i,j}$ is the covariance matrix for the noise of $\mathbf{t}_{i,j}$ (see (6.15)). These covariance matrices $\boldsymbol{\Sigma}_{i,j}$ are a function of $\boldsymbol{\mu}_{i,j}$, which in turn depend on the parameters to be estimated. As a consequence, maximum likelihood estimation will be complex. Therefore, we will use the least squares (LS) method to estimate the intrinsic and extrinsic parameters. Let us define the parameter set $\boldsymbol{\Theta} = \{\mathbf{k}, \mathbf{T}_1, \dots, \mathbf{T}_{N_T}\}$, then the LS estimate is given by:

$$\hat{\boldsymbol{\Theta}} = \arg \min_{\boldsymbol{\Theta}} \frac{1}{2} \|\check{\mathbf{t}} - \check{\boldsymbol{\mu}}\|^2, \quad \text{s.t. } \mathbf{R}^T \mathbf{R} = \mathbf{I}, \quad \det(\mathbf{R}) = +1. \quad (6.21)$$

The constraint $\mathbf{R}_i^T \mathbf{R}_i = \mathbf{I}$ implies that \mathbf{R}_i , which defines the orientation of the receiver at PO i and is enclosed in the transform matrix $\mathbf{T}_i^{-1} \in SE(3)$ (see (6.2)), should be a member of $SO(3)$. Unfortunately, (6.21) has no closed-form solution, implying we need to resort to an iterative algorithm to estimate $\boldsymbol{\Theta}$. As the solution of the above (iterative) constrained optimization problem is complex and cumbersome in Euclidean space, we first notice that $SE(3)$ is a manifold and convert the above optimization problem into an unconstrained

optimization problem on manifolds [44]. In what follows, we use the Gauss-Newton method on manifold $SE(3)$ to solve (6.21). At each iteration, the update direction is calculated by

$$\left[\Delta_{\mathbf{k}}, \Delta_{\mathbf{T}_1}, \dots, \Delta_{\mathbf{T}_{N_T}} \right]^T = (\nabla_{\Theta} \check{\boldsymbol{\mu}})^\dagger (\check{\mathbf{t}} - \check{\boldsymbol{\mu}}) \quad (6.22)$$

where $\nabla_{\Theta} \check{\boldsymbol{\mu}} = [\nabla_{\Theta} \boldsymbol{\mu}_{1,1}, \nabla_{\Theta} \boldsymbol{\mu}_{1,2}, \dots, \nabla_{\Theta} \boldsymbol{\mu}_{N_T, N_L}]^T \in \mathbb{R}^{2N_T N_L \times (6N_T + 3)}$ is the gradient of $\check{\boldsymbol{\mu}}$ with respect to Θ .

Based on the chain rule, $\nabla_{\Theta} \boldsymbol{\mu}_{i,j} = \nabla_{\mathbf{r}_{I,i,j}} \boldsymbol{\mu}_{i,j} \nabla_{\Theta} \mathbf{r}_{I,i,j} \in \mathbb{R}^{2 \times (6N_T + 3)}$, where $\nabla_{\mathbf{r}_{I,i,j}} \boldsymbol{\mu}_{i,j}$ is the gradient of $\boldsymbol{\mu}_{i,j}$ with respect to $\mathbf{r}_{I,i,j}$, and $\nabla_{\Theta} \mathbf{r}_{I,i,j}$ is the gradient of $\mathbf{r}_{I,i,j}$ with respect to Θ . $\nabla_{\mathbf{r}_{I,i,j}} \boldsymbol{\mu}_{i,j}$ is determined by its k^{th} component

$$\left[\nabla_{\mathbf{r}_{I,i,j}} \boldsymbol{\mu}_{i,j} \right]_k = \frac{(2 - 2 \cos 2\alpha_k) \mathbf{e}_k^T}{l\pi \sqrt{1 - (\mathbf{e}_k^T \mathbf{r}_{I,i,j} / l)^2}}, \quad (6.23)$$

while $\nabla_{\Theta} \mathbf{r}_{I,i,j} = [\nabla_{\mathbf{k}} \mathbf{r}_{I,i,j}, \nabla_{\mathbf{T}_1} \mathbf{r}_{I,i,j}, \dots, \nabla_{\mathbf{T}_{N_T}} \mathbf{r}_{I,i,j}] \in \mathbb{R}^{2 \times (6N_T + 3)}$ is given by

$$\nabla_{\mathbf{k}} \mathbf{r}_{I,i,j} = \frac{(\mathbf{T}_i \bar{\mathbf{r}}_{L,j})^{\odot}}{\mathbf{e}_3^T \mathbf{T}_i \bar{\mathbf{r}}_{L,j}} \quad (6.24)$$

and

$$\nabla_{\mathbf{T}_k} \mathbf{r}_{I,i,j} = \begin{cases} \left(\frac{\mathbf{K}}{\mathbf{e}_3^T \mathbf{T}_i \bar{\mathbf{r}}_{L,j}} - \frac{\mathbf{K} \mathbf{T}_i \bar{\mathbf{r}}_{L,j} \mathbf{e}_3^T}{(\mathbf{e}_3^T \mathbf{T}_i \bar{\mathbf{r}}_{L,j})^2} \right) (\mathbf{T}_i \bar{\mathbf{r}}_{L,j})^{\odot} & \text{if } k = i \\ \mathbf{0} \in \mathbb{R}^{2 \times 6} & \text{if } k \neq i \end{cases}, \quad (6.25)$$

where the gradient of $\mathbf{r}_{I,i,j}$ with respect to \mathbf{T}_k (6.25) is calculated with the infinitesimal perturbation, and the operators \cdot^{\odot} and \cdot^{\wedge} are defined as

$$\left([a_1, a_2, a_3, a_4]^T \right)^{\odot} = \begin{bmatrix} a_3 & 0 & a_1 \\ 0 & a_3 & a_2 \end{bmatrix}, \quad (6.26)$$

and

$$\left([\boldsymbol{\xi}^T, \eta]^T \right)^{\wedge} = \begin{bmatrix} \eta \mathbf{I}_3 & -\boldsymbol{\xi}^{\wedge} \\ \mathbf{0}^T & \mathbf{0}^T \end{bmatrix}, \quad (6.27)$$

respectively.

As the update directions (6.22) depend on \mathbf{k} and all \mathbf{T}_i , the intrinsic parameters and the POs need to be estimated jointly:

$$\begin{cases} \mathbf{k}^{t+1} = \mathbf{k}^t + \tau_{\mathbf{k}} \Delta_{\mathbf{k}}(\mathbf{k}^t, \mathbf{T}_1^t, \dots, \mathbf{T}_{N_T}^t) \\ \mathbf{T}_i^{t+1} = \exp \left((\tau_{\mathbf{T}} \Delta_{\mathbf{T}_i}(\mathbf{k}^t, \mathbf{T}_1^t, \dots, \mathbf{T}_{N_T}^t))^{\wedge} \right) \mathbf{T}_i^t, \quad i \in \{1, \dots, N_T\} \end{cases} \quad (6.28)$$

where $\tau_{\mathbf{k}}$ and $\tau_{\mathbf{T}}$ control the incremental step size for \mathbf{k} and \mathbf{T}_i , respectively.

The Gauss-Newton method needs an initialization Θ^0 to start the iterative estimation process. To obtain this initial estimate, we consider the direct linear transformation method [78]. Assuming the positions of at least four LEDs and

the positions of the light spots for these LEDs are known, the direct linear transformation method gives a closed-form coarse estimate for Θ^0 . Although in our problem, the positions of the light spots are not known, we can estimate them from the normalized differences $\mathbf{t}_{i,j}$, which is a noisy version of $\boldsymbol{\mu}_{i,j}$ (6.17). This $\boldsymbol{\mu}_{i,j}$ is a function of the angles α_ℓ , $\ell = 1, 2$ (6.16), which in turn are related to the position $\mathbf{r}_{S,q,i,j}$ of the light spot, i.e. we can write $\boldsymbol{\mu}_{i,j}$ as a function of $\mathbf{r}_{S,q,i,j}$: $\boldsymbol{\mu}_{i,j}(\mathbf{r}_{S,q,i,j})$. In many situations, the noise is relatively small, implying we can neglect the presence of the noise, i.e. $\mathbf{t}_{i,j} \approx \boldsymbol{\mu}_{i,j}$. Inverting the function $\boldsymbol{\mu}_{i,j}(\mathbf{r}_{S,q,i,j})$, we obtain the coarse estimate $\hat{\mathbf{r}}_{S,q,i,j} \in \mathbb{R}^{2 \times 1}$ of the light spot for the j^{th} LED and the i^{th} PO:

$$\hat{\mathbf{r}}_{I,i,j} = \boldsymbol{\varphi}^{-1}(\mathbf{t}_{i,j}), \quad (6.29)$$

where $(\cdot)^{(-1)}$ is the inversion operator.

6.2.2 The Theoretical Lower Bound

In order to get insight into the optimality of the designed calibration algorithm and to investigate how the SNR, N_L or N_T would effect the accuracy of the estimator, we derive in this section the theoretical lower bound for the mean squared errors of h_a and $\mathbf{k}_{m,q}$. Since the estimation includes the unwanted parameter \mathbf{T}_i and since the estimator is designed based on an approximated PDF, we will derive the misspecified Cramér-Rao bound (MCRB) for the whole parameter set Θ and keep the left upper 3×3 submatrix corresponding to the intrinsic parameters. The MCRB for the whole parameter set Θ is given by Θ is given by

$$\text{MCRB}(\Theta) = (\mathbf{M}_1(\hat{\Theta}))^{-1} \mathbf{M}_2(\hat{\Theta}) (\mathbf{M}_1(\hat{\Theta}))^{-1} + \text{Bias}(\hat{\Theta}, \Theta). \quad (6.30)$$

In (6.30) $\hat{\Theta}$ is the parameter set to which the estimation converges due to the PDF approximation assumed by the estimator, given by

$$\hat{\Theta} = \arg \min_{\Theta} D(p(\check{\mathbf{t}}) || p_m(\check{\mathbf{t}}|\Theta)), \quad (6.31)$$

where $D(p(\check{\mathbf{t}}) || p_m(\check{\mathbf{t}}|\Theta))$ is the Kullback-Leibler divergence (KLD) between the true $(p(\check{\mathbf{t}}))$ and the approximated $(p_m(\check{\mathbf{t}}|\Theta))$ PDFs. The matrices \mathbf{M}_1 , \mathbf{M}_2 , and $\text{Bias}(\hat{\Theta}, \Theta)$ are respectively given by

$$\mathbf{M}_1 = E_{\check{\mathbf{t}}} \{ \Delta_{\Theta}^{\Theta} \ln p_m(\check{\mathbf{t}}|\Theta), \} \quad (6.32)$$

$$\mathbf{M}_2 = E_{\check{\mathbf{t}}} \{ \nabla_{\Theta}^T \ln p_m(\check{\mathbf{t}}|\Theta) \nabla_{\Theta} \ln p_m(\check{\mathbf{t}}|\Theta), \} \quad (6.33)$$

$$\text{Bias}(\hat{\Theta}, \Theta) = \boldsymbol{\epsilon}(\hat{\Theta}, \Theta) \boldsymbol{\epsilon}(\hat{\Theta}, \Theta)^T, \quad (6.34)$$

where $\boldsymbol{\epsilon}(\hat{\Theta}, \Theta)$ is the error vector between $\hat{\Theta}$ and Θ . The error vector is defined as $\boldsymbol{\epsilon}(\hat{\Theta}, \Theta) = [\boldsymbol{\epsilon}_{\mathbf{k}}^T, \boldsymbol{\epsilon}_{\mathbf{T}_1}^T, \dots, \boldsymbol{\epsilon}_{\mathbf{T}_{N_T}}^T]^T$ with $\boldsymbol{\epsilon}_{\mathbf{k}} = \hat{\mathbf{k}} - \mathbf{k}$ and $\boldsymbol{\epsilon}_{\mathbf{T}_i} = \log(\mathbf{T}_i \hat{\mathbf{T}}_i^{-1})^{\vee}$, and \cdot^{\vee} is the inverse operator of \cdot^{\wedge} . Since the designed estimator neglects

the effect of covariance matrix, the dependency of the covariance matrix on the parameter set is neglected for the derivative in (6.32) and (6.33). After a few rearrangements, it can be seen that the expectations in (6.32) and (6.33) depend on $p(\check{\mathbf{t}})$ through its mean and covariance only, which can be calculated numerically via Monte Carlo integration.

In order to analyze the effect of N_T , N_L and SNR, we take into account that since $p_m(\check{\mathbf{t}}|\Theta)$ is Gaussian the minimum of the KLD (6.31) is obtained when the first two moments of the true and the approximated PDFs are matched [79] and that when the SNR is high, $p_m(\check{\mathbf{t}}|\Theta)$ approximates the true PDF with a high accuracy so that the first two moments of the approximated PDF approach these of the true PDF. As a result, the estimator is asymptotically unbiased, i.e., $\text{Bias}(\hat{\Theta}, \Theta) \approx \mathbf{0}$ for $\text{SNR} \gg 1$, so that $\mathbf{M}_1 \approx \mathbf{M}_2$, $\text{MCRB}(\Theta) \approx \mathbf{M}_2^{-1}$ and

$$\mathbf{M}_2 \approx \sum_i^{N_T} \sum_j^{N_L} \nabla_{\Theta}^T \mu_{i,j} \Sigma_{i,j}^{-1} \nabla_{\Theta} \mu_{i,j}. \quad (6.35)$$

It can be seen that when N_T or N_L increases, the number of terms in (6.35) increases. As the matrices being summed in (6.35) are symmetric and positive-semidefinite, this implies that \mathbf{M}_2 is non-decreasing in the sense of Loewner order. Further, as $\Sigma_{i,j}^{-1}$ is proportional to the SNR, increasing the SNR also enlarges the Loewner order of these matrices being summed and thus leads the partial order of \mathbf{M}_2 to enhance. As a result, the MCRB is a non-increasing function of N_T , N_L or SNR. While increasing N_T , N_L or SNR increases the robustness of the estimator against noise, these parameters do not have an impact on the feasibility of the estimation. The number of observations required to make proper estimation feasible follows from the analysis from [78] dealing with intrinsic parameter estimation for cameras. Translating the results of that paper to the problem at hand, it follows that observations at two different POs provide sufficient constraints to avoid depth ambiguity, and at each PO, at least four LEDs should be observed to have enough information for the calibration.

In this paper, we estimated the intrinsic parameters from the normalized differences instead of the quad-tuple of RSS values, where the PDF of the normalized differences was approximated by a Gaussian distribution. To evaluate the effect of both the approximation and normalized differencing, we compare the misspecified Cramér-Rao bound $\text{MCRB}(\Theta)$ (6.30) with the Cramér-Rao bound for the quad-tuple of RSS values $\check{\mathbf{y}}$ observed by the QPD, i.e. $\text{CRB}(\Theta)$, corresponding to the true PDF $p(\check{\mathbf{y}})$. As $\check{\mathbf{y}}$ is Gaussian distributed, the derivation of the Fisher information matrix $\mathbf{J}(\Theta)$ and thus $\text{CRB}(\Theta) = \mathbf{J}^{-1}(\Theta)$ [66] is straightforward, and yields

$$\mathbf{J}(\Theta) = (\nabla_{\Theta} \check{\mathbf{g}})^T \check{\Sigma}_{\check{\mathbf{g}}}^{-1} (\nabla_{\Theta} \check{\mathbf{g}}), \quad (6.36)$$

where $\nabla_{\Theta} \check{\mathbf{g}} = [\nabla_{\Theta} \mathbf{g}_{1,1}, \nabla_{\Theta} \mathbf{g}_{1,2}, \dots, \nabla_{\Theta} \mathbf{g}_{N_T, N_L}]^T \in \mathbb{R}^{(4N_T N_L) \times (6N_T + 3)}$ denotes the gradient of $\check{\mathbf{g}}$ with respect to Θ with component $\nabla_{\Theta} \mathbf{g}_{i,j} = R_p P_t \nabla_{\Theta} \mathbf{g}_{i,j}$, and the gradient of $\mathbf{h}_{i,j}$ with respect to Θ is specified by its k^{th} component,

i.e.,

$$[\nabla_{\Theta} \mathbf{h}_{i,j}]_k = C_{i,j} \cdot \left[\begin{array}{c} \frac{\gamma A_{i,j,k} (\mathbf{n}_{L,j}^T \mathbf{v}_{i,j})^{\gamma-1} (\mathbf{n}_P^T \mathbf{v}_{i,j})}{\|\mathbf{v}_{i,j}\|^{\gamma+3}} \\ \frac{A_{i,j,k} (\mathbf{n}_{L,i}^T \mathbf{v}_{i,j})^\gamma}{\|\mathbf{v}_{i,j}\|^{\gamma+3}} \\ - \frac{(\gamma+3) A_{i,j,k} (\mathbf{n}_{L,j}^T \mathbf{v}_{i,j})^\gamma (\mathbf{n}_P^T \mathbf{v}_{i,j})}{(\mathbf{n}_{L,j}^T \mathbf{v}_{i,j}) \|\mathbf{v}_{i,j}\|^{\gamma+5}} \\ \frac{(\mathbf{n}_{L,j}^T \mathbf{v}_{i,j}) (\mathbf{n}_P^T \mathbf{v}_{i,j})}{\|\mathbf{v}_{i,j}\|^{\gamma+3}} \end{array} \right]^T \cdot \left[\begin{array}{c} \bar{\mathbf{n}}_{L,j}^T \cdot \nabla_{\Theta} \bar{\mathbf{v}}_{i,j} \\ \bar{\mathbf{n}}_P^T \cdot \nabla_{\Theta} \bar{\mathbf{v}}_{i,j} \\ \bar{\mathbf{v}}_{i,j}^T \cdot \nabla_{\Theta} \bar{\mathbf{v}}_{i,j} \\ [\nabla_{\Theta} \mathbf{A}_{i,j}]_k \end{array} \right], \quad (6.37)$$

where $\nabla_{\Theta} \bar{\mathbf{v}}_{i,j} = [\nabla_{\mathbf{k}} \bar{\mathbf{v}}_{i,j}, \nabla_{\mathbf{T}_1} \bar{\mathbf{v}}_{i,j}, \dots, \nabla_{\mathbf{T}_{N_T}} \bar{\mathbf{v}}_{i,j}] \in \mathbb{R}^{4 \times (6N_T+3)}$ with

$$\nabla_{\mathbf{k}} \bar{\mathbf{v}}_{i,j} = \mathbf{T}_i^{-1} \left[\mathbf{0}_{4 \times 2}, \text{diag} \left(\begin{bmatrix} 1 \\ 1 \\ 1 \\ 0 \end{bmatrix} \right) \frac{\mathbf{T}_i \bar{\mathbf{r}}_{L,j}}{\mathbf{e}_3^T \mathbf{T}_i \bar{\mathbf{r}}_{L,j}} \right], \quad (6.38)$$

and

$$\nabla_{\mathbf{T}_k} \bar{\mathbf{v}}_{i,j} = \begin{cases} \mathbf{T}_i^{-1} \left(\frac{\mathbf{K}_0 (\mathbf{T}_i \bar{\mathbf{r}}_{L,j})^\odot}{\mathbf{e}_3^T \mathbf{T}_i \bar{\mathbf{r}}_{L,j}} - \left(\frac{\mathbf{K}_0 \mathbf{T}_i \bar{\mathbf{r}}_{L,j}}{\mathbf{e}_3^T \mathbf{T}_i \bar{\mathbf{r}}_{L,j}} \right)^\odot - \frac{\mathbf{K}_0 \mathbf{T}_i \bar{\mathbf{r}}_{L,j} \mathbf{e}_3^T (\mathbf{T}_i \bar{\mathbf{r}}_{L,j})^\odot}{(\mathbf{e}_3^T \mathbf{T}_i \bar{\mathbf{r}}_{L,j})^2} \right) & \text{if } k = i \\ \mathbf{0} \in \mathbb{R}^{4 \times 6} & \text{if } k \neq i \end{cases} \quad (6.39)$$

Based on the chain rule, we have $\nabla_{\Theta} \mathbf{A}_{i,j} = \mathbf{M}_a^{-1} \nabla_{\mathbf{r}_{I,i,j}} \mathbf{s} \nabla_{\Theta} \mathbf{r}_{I,i,j} \in \mathbb{R}^{4 \times (6N_T+3)}$, where

$$\nabla_{\mathbf{r}_{I,i,j}} \mathbf{s} = l \begin{bmatrix} \sin \alpha_{1,i,j} + \cos \alpha_{2,i,j}, & \cos \alpha_{1,i,j} + \sin \alpha_{2,i,j} \\ -2 \sin \alpha_{1,i,j}, & 0 \\ 0, & -2 \sin \alpha_{2,i,j} \\ 0, & 0 \end{bmatrix} \quad (6.40)$$

and \mathbf{M}_a is defined in (6.7).

6.2.3 SPO Estimation

Once the intrinsic parameters are estimated during the calibration process, the estimated parameters can be used for accurate SPO estimation of the receiver. To estimate the PO, a similar procedure can be used as for the calibration, by means of the Gauss-Newton method, except that now it is assumed that the intrinsic parameters \mathbf{k} are known. At i^{th} PO, the observation \mathbf{t}_i only depends on the PO \mathbf{T}_i , and is independent of other POs. Therefore, we can estimate the POs independently, in contrast to the calibration procedure that needed to consider the observations of multiple POs due to the presence of the unknown intrinsic parameters. Again, the estimation is obtained with an iterative procedure, of which the update step is the same as in (6.28):

$$\mathbf{T}_i^{t+1} = \exp((\tau_{\mathbf{T}} \Delta_{\mathbf{T}_i})^\wedge) \mathbf{T}_i^t \quad (6.41)$$

Similarly as in the calibration procedure, we can obtain a coarse estimate by means of the direct linear transformation method together with (6.29) to initialize the Gauss-Newton method for SPO estimation.

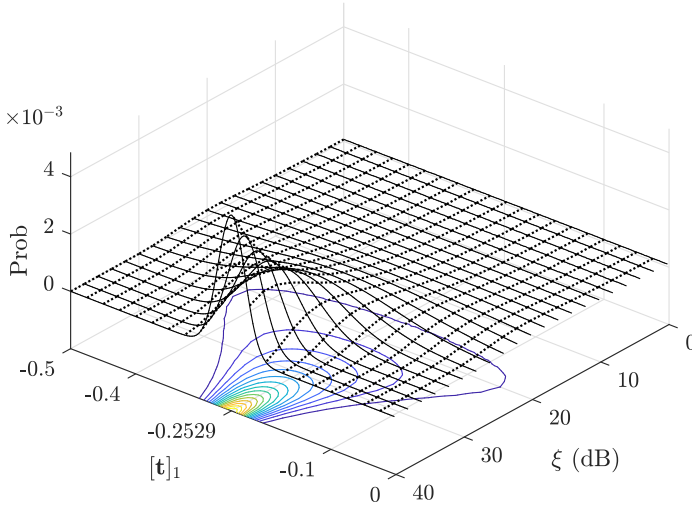
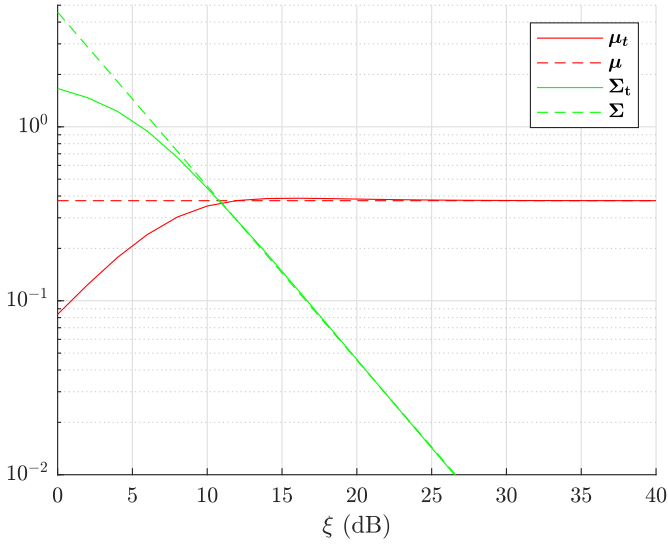


Figure 6.3: Histogram of $[t]_1$ as a function of ξ .

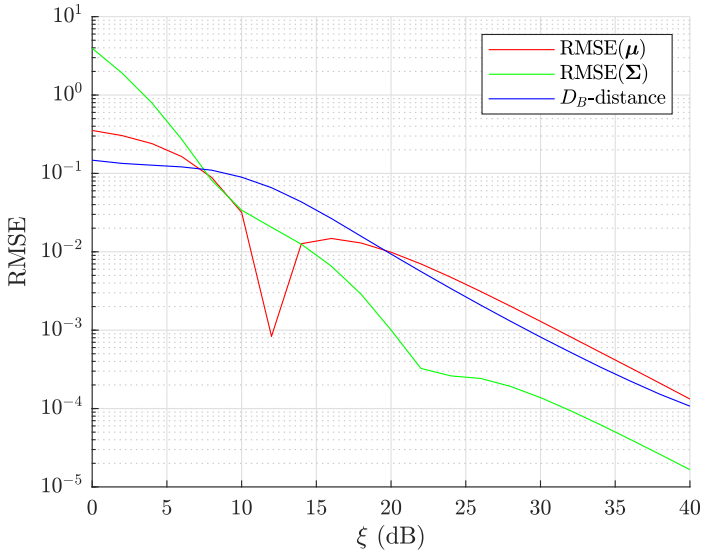
6.3 Numerical Assessment and Experiment

In this section, we first evaluate the normalized differencing and its approximation. Later, we verify the performance of the proposed calibration algorithm and compare the mean squared error with the theoretical bound based on simulations. Then, the calibration procedure is used to determine the intrinsic parameters in an experimental setup, after which the PO is estimated from the measurements.

Now, we will evaluate the approximation (6.17) by a comparison with respect to the true PDF of \mathbf{t} . To this end, we assume $\frac{\mathbf{r}}{r} = [0.2, -0.3]^T$, which leads to $\boldsymbol{\mu} = [0.2529, -0.3762]^T$. The true PDF is obtained by the histogram of \mathbf{t} trails generated with Monte Carlo method through (6.10) and (6.11). The histogram of $[t]_1$ as a function of $\xi \in [0, 40]$ dB and corresponding contours are given in Fig. 6.3. It can be seen that the PDF of $[t]_1$ appears Gaussian and is centered at $[\boldsymbol{\mu}]_1$ when ξ is large while it is very flat when ξ is small. Next, we quantitatively evaluate the mismatch between the approximated and the true parameters. The residual error of mean is measured by the L_2 -norm $\text{RMSE}(\boldsymbol{\mu}) = \|\boldsymbol{\mu}_t - \boldsymbol{\mu}\|_2$, while that of covariance is measured by the Frobenius norm $\text{RMSE}(\boldsymbol{\Sigma}) = \|\boldsymbol{\Sigma}_t - \boldsymbol{\Sigma}\|_F$. The Bhattacharyya distance is adopted to measure the similarity between the approximated and the true PDFs. Fig. 6.4a shows the comparison, while Fig. 6.4b gives the residual error. It can be seen that the mean becomes constant and the variance decreases linearly with respect to ξ when the received SNR is large, while the approximated mean and variance approach the true values asymptotically with respect to the received



(a)



(b)

Figure 6.4: Evaluation of approximated mean and covariance. (a) Approximated values as a function of ξ . (b) RMSE as a function of ξ .

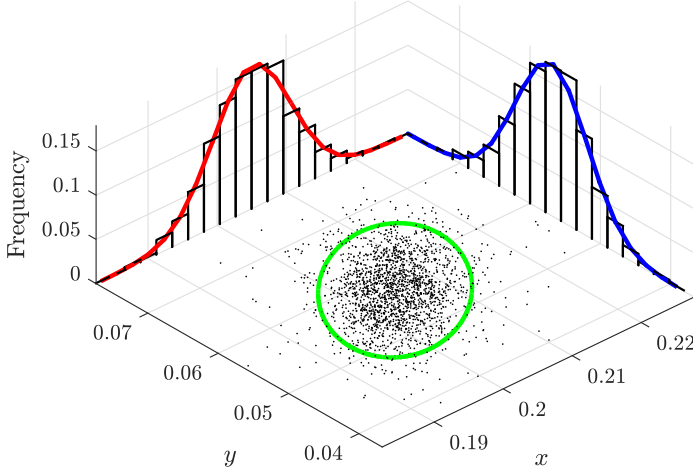


Figure 6.5: Histograms of the empirical observation along with fitted Gaussian curves.

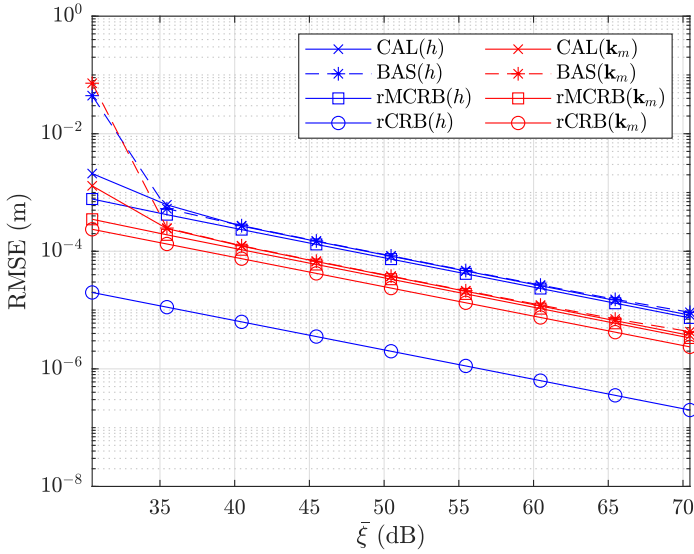
SNR. The Bhattacharyya distance (denoted by D_B -distance) in Fig. 6.4b indicates that the approximation (6.17) achieves a better accuracy as the received SNR increases.

Here, we also give an experimental result to verify the analysis. Fig. 6.5 illustrates the histogram of \mathbf{t} sampled in an experiment (the setting will be given in details in Section 6.3) along with the fitted Gaussian curves, which confirms that \mathbf{t} complies with a bivariate normal distribution.

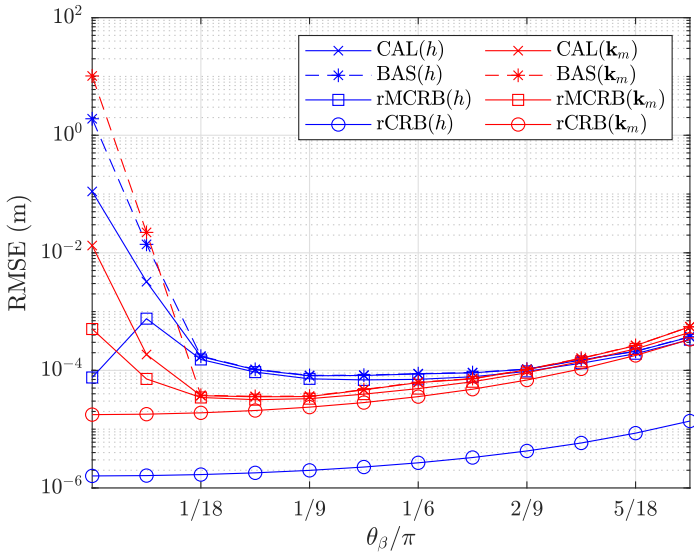
6.3.1 Numerical Assessment of Calibration Algorithm

For the simulations, we consider the following setup. All LEDs are assumed to have a transmit power $P_t = 1$ W, and Lambertian order $\gamma = 1$. We set the origin of the system frame as the center of the LED plane. We assume $N_L = N_{L,r}^2$ LEDs are placed in a square grid with an area of 400 cm^2 , where the LED in the i^{th} row and j^{th} column has position $\mathbf{r}_L = \left(\frac{20}{N_{L,r}-1} \begin{bmatrix} i-1 \\ j-1 \end{bmatrix} - \begin{bmatrix} 10 \\ 10 \end{bmatrix} \right)$ cm, $i, j \in \{1, \dots, N_{L,r}\}$. We set the vertical distance between the LEDs plane and the receiver equal to $z = 0.65$ m.

The receiver consists of a circular QPD with radius $r_p = 5$ mm, resulting in an active area $A_p = \pi r_p^2$, and responsivity $R_p = 0.4$ A/W. Above the QPD, we place at a height $|h_a| = 3.0$ mm a circular aperture with radius of $l = 2.5$ mm. In our simulations, we set the misalignment between the centers of the aperture and the QPD equal to $\mathbf{k}_{m,q} = [0.5, -0.3]$ mm. The noise in



(a)



(b)

Figure 6.6: RMSE of the estimator (a) as a function of $\bar{\xi}$, where $N_L = 25$, $N_T = 4$, and $\theta_\beta = \pi/9$ rad, (b) as a function of θ_β , where $\text{SNR} = 45$ dB, $N_L = 25$, and $N_T = 4$.

the different quadrants of the QPD is assumed to have correlation coefficient $\rho = 0.7$. The orientation \mathbf{R} of the receiver is defined with the ZXZ Euler angles $[\theta_\alpha, \theta_\beta, \theta_\gamma]$. We assume the azimuth and roll angles, i.e., θ_α and θ_γ , are uniformly distributed over $[0, 2\pi)$, and we set the elevation angle θ_β as a variable. In this way, the receiver has a random orientation but a controlled tilt angle of θ_β . To ensure that most LEDs are observed, we select the position of the receiver so that it is pointing towards the center of the LEDs plane: $\mathbf{r} = \frac{z\mathbf{R}\mathbf{e}_3}{e_3^T\mathbf{R}\mathbf{e}_3}$.

In the simulations, we use (6.18) to generate the observations. We assume the shot noise has power spectral density $N_0 = 2.10 \times 10^{-22} \text{A}^2/\text{Hz}$, which corresponds to a background spectral irradiance $p_n = 5.8 \times 10^{-6} \text{ W}/(\text{cm}^2 \cdot \text{nm})$ and a visible light bandwidth $\Delta\lambda = 360 \text{ nm}$ [14]. Suppose the electrical bandwidth equals $B = 1 \text{ MHz}$ [34], the noise variance σ_{w3}^2 can be computed with $\sigma_{w3}^2 = N_0 B$. Simulation results will be given in terms of the effective³ SNR = $\left(\frac{(\gamma+1)A_a R_t P_t}{2\pi\sigma_{w3}}\right)^2$ with $A_a = \pi l^2$. Given the optical transmit power $P_t = 1 \text{ W}$, we obtain the effective SNR = 44.73 dB. In our simulations, we will use the range SNR $\in [25, 65]$ dB to take into account variations of the system parameters.

First, we evaluate the performance of the designed calibration estimator as a function of SNR. As a baseline method, we consider the calibration algorithm for cameras [80]. Because the algorithm of [80] takes the image of an object as input, which in this case corresponds to the observation of the light spot's position, we use (6.29) prior to this algorithm to convert the observation \mathbf{t} to the estimated center of the light spot. The number of LEDs in the LED plane is set to $N_L = 25$, and the receiver observes the plane from $N_T = 4$ randomly generated POs with $\theta_\beta = \pi/9$ rad. We vary the SNR from 25 to 65 dB and plot in Fig. 6.6a the resulting RMSE (denoted by CAL) versus $\bar{\xi}$, i.e., the received SNR averaged over the four POs. The root of the MCRB and CRB (denoted by rMCRB and rCRB) from Section 6.2.2 and the performance of the baseline method (denoted by BAS) are also plotted for comparison. As we can see from Fig. 6.6a, at high $\bar{\xi}$, the two calibration methods perform close to optimal, while at low $\bar{\xi}$, the proposed calibration algorithm outperforms the baseline method. This can be explained as the bias in (6.29) for the baseline method is larger than for the proposed calibration method when $\bar{\xi}$ is low. The gap between MCRB and CRB reflects the net performance cost of the followed strategy where we use the normalized differences instead of the RSS values and the approximated PDF. The gap shows that the robustness to imperfect knowledge of the transmit power and radiation pattern of the LEDs, obtained by this strategy, is achieved at the cost of accuracy. The performance loss for the estimation of h_a is larger than for the estimation of \mathbf{k}_m .

Next, we evaluate the effect of the number N_L of LEDs and the number N_T of POs. We set SNR = 45 dB and $\theta_\beta = \pi/9$ rad. Both variables influence

³As the received SNR depends on the receiver PO, a fixed received SNR will limit the parameter space of the receiver PO. As this will complicate the simulation, we chose to fix the effective SNR.

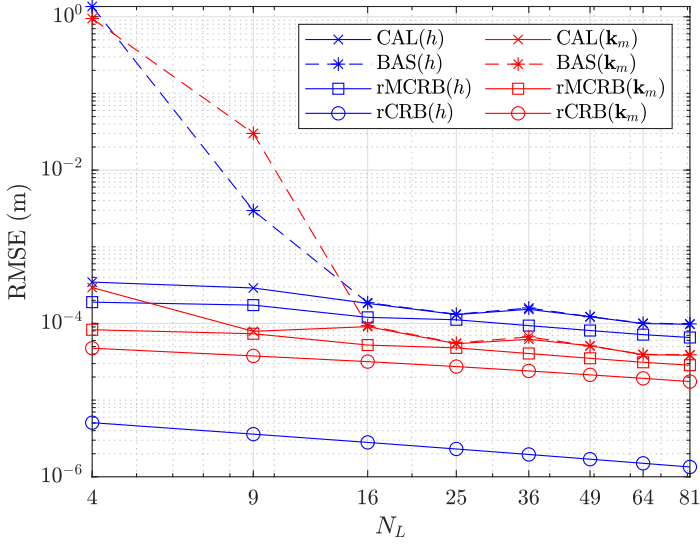
the number of observations, so we expect that increasing either N_L or N_T will improve the performance of the calibration. In Fig. 6.7a, we show the performance for $N_{L,r} = \sqrt{N_L} = \{2, 3, \dots, 9\}$ with $N_T = 3$, and in Fig. 6.7b for $N_T = \{2, 4, \dots, 16\}$ with $N_L = 25$. The figures show that the lower bound is reached for both the proposed calibration method and the baseline method when N_L or N_T is sufficiently large. In that case, the performance improves logarithmically with N_L and N_T . When N_L or N_T are small, i.e. when the number of observations is small, the proposed method outperforms the baseline method.

Finally, we evaluate the effect of the orientation θ_β of the receiver with respect to the LED plane. We set SNR= 45 dB, $N_L = 25$, and $N_T = 4$. The calibration performance for θ_β varying from 0 rad to $5\pi/18$ rad is shown in Fig. 6.6b. When θ_β is small, the performance first improves by increasing θ_β . This can be explained as for small θ_β , the randomly generated poses are very close to each other implying the solution set is loosely constrained and thus more susceptible to the noise. For large θ_β , the performance starts to degrade, as in our assumptions we assumed that the receiver is pointing to the center of the LEDs plane, implying large θ_β corresponds to placing the receiver far from the center of the LEDs plane. As a consequence, the RSS values will experience lower SNR values, causing the slight degradation of the performance. The optimal performance will therefore occur at intermediate values of θ_β .

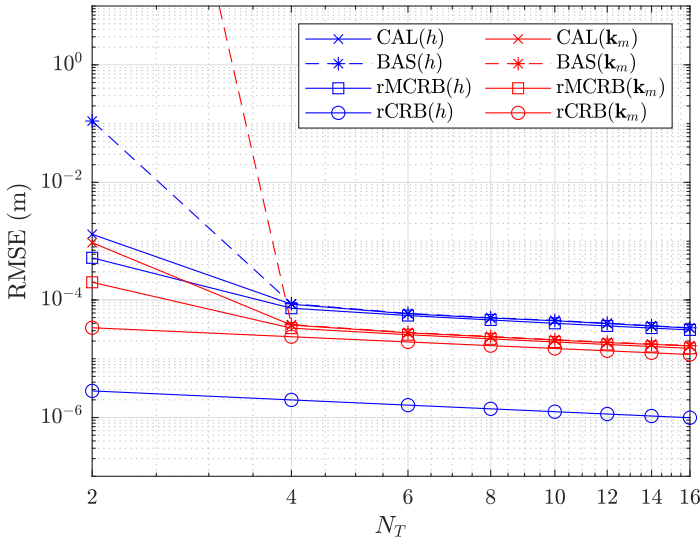
6.3.2 Numerical Assessment of SPO Estimator

In the evaluation of the estimator through computer simulations, we consider a setup similar to the one shown in Fig. 4.3 in Chapter 4, except that $N_L = 36$ LEDs are mounted at the ceiling of a $5 \text{ m} \times 5 \text{ m} \times 3 \text{ m}$ area. We also consider a path similar to the one shown in Fig. 4.3. However, the path used here has a circular pattern in the XY plane and the radius of the circle is 1.5 m, and the amplitude of the sinusoidal pattern is 0.2 m. The circle is centered at $[2.5, 2.5, 1.5]^T$ m, i.e. the center of the considered area. Starting at the coordinates $[4.0, 2.5, 1.5]^T$ m, the path oscillates sinusoidally in the Z direction and completes the path in three periods. A detection algorithm is assumed so that the estimation is based on those LEDs that have a light spot overlapping all quadrants of the photodiode only.

In Fig. 6.8, we show the RMSE of the PO estimates of the proposed estimator with calibration (assuming a known \mathbf{k}_m) as a function of the position θ_r of the receiver in the path for $P_t = 1 \text{ W}$, and compare the resulting RMSE with that of the estimator without calibration (assuming $\mathbf{k}_m = \mathbf{0}$). The mean received SNR $\bar{\xi}$ at each position is also plotted for comparison. It can be observed in Fig. 6.8 that the RMSE performance changes reversely with respect to $\bar{\xi}$. This is expected, since the RMSE has a negative correlation with the received SNR, that is, a large RMSE is obtained when the received SNR is small, and vice versa. Comparing the performance between the estimators with and without calibration, we can see that the misspecified intrinsic parameters degrade the estimator's performance, especially the positioning performance.



(a)



(b)

Figure 6.7: RMSE of the estimator (a) as a function of N_L , where $\text{SNR} = 45$ dB, $N_T = 4$, and $\theta_\beta = \pi/9$ rad, (b) as a function of N_T , $\text{SNR} = 45$ dB, $N_L = 25$, and $\theta_\beta = \pi/9$ rad.

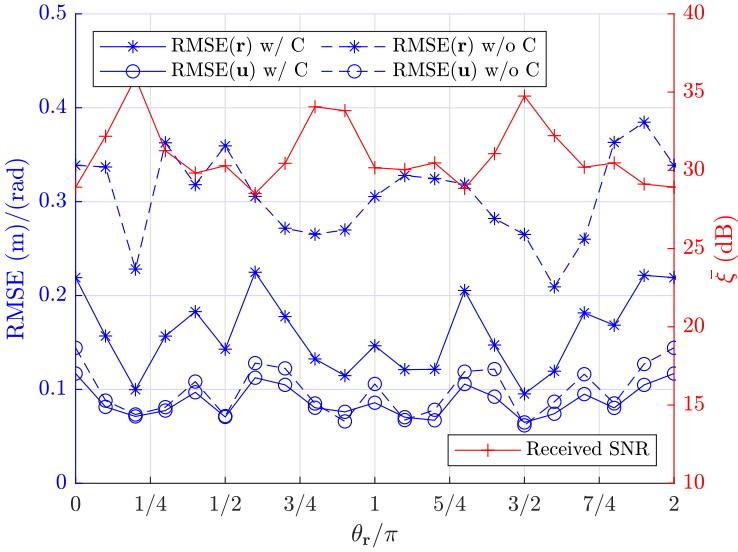


Figure 6.8: RMSE for position and orientation estimates as a function of θ_r , compared with the mean received SNR $\bar{\xi}$.

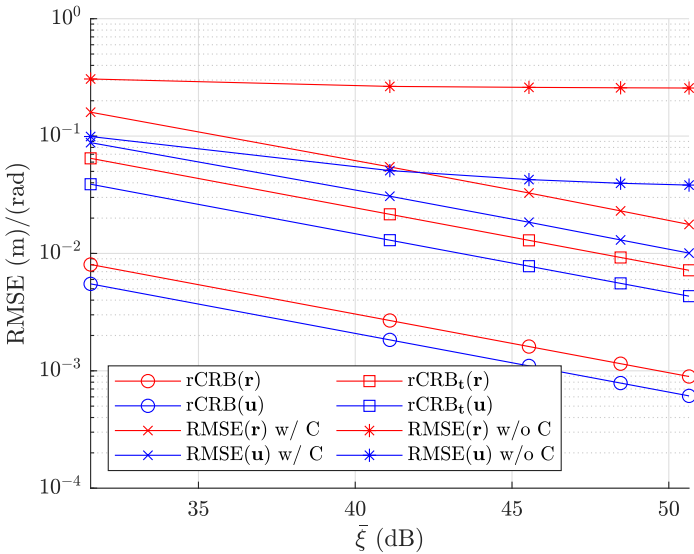


Figure 6.9: RMSE for position and orientation estimates as a function of the mean received SNR $\bar{\xi}$.

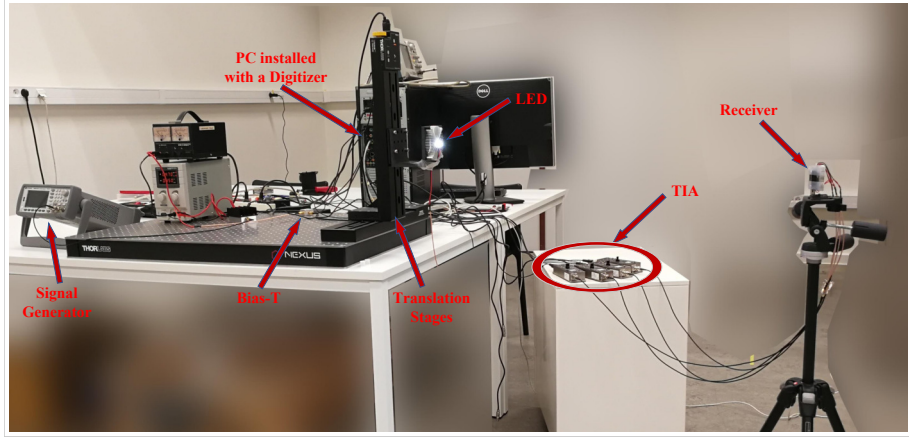


Figure 6.10: Experiment setup.

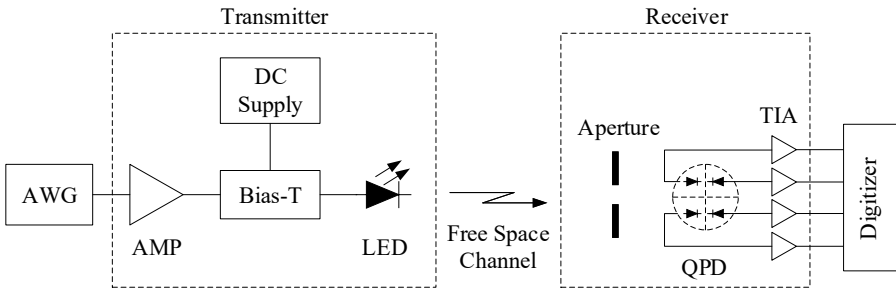


Figure 6.11: Block diagram of the experiment setup.

Next, we evaluate the proposed estimator with respect to the transmitted power. In this simulation, the RMSE is first evaluated with the transmitted power $P_t = \{1, 3, \dots, 9\}$ W and then averaged over the path. In Fig. 6.9, we show the averaged RMSE and the associated root of the theoretical bound as a function of the mean received SNR ξ . The results show that when the calibration is applied (assuming a known \mathbf{k}_m), the performance of the proposed estimator (denoted by RMSE w/ C) improves linearly with respect to the received SNR. However, when no calibration is used (assuming $\mathbf{k}_m = \mathbf{0}$), we observe that the estimator (denoted by RMSE w/o C) shows an error floor for large SNR.

6.3.3 Experiment Results

In the experiment, we use the setup as shown in Figs. 6.10 and 6.11. More specifically, a signal generator (Keysight 33622A) generates a 0.8 MHz sinusoidal signal with amplitude 0.3 V, which is the maximum amplitude that

Table 6.1: Experiment specification.

Component/Parameter	Model/Value
Arbitrary Waveform Generator	Keysight 33622A
Amplifier	Mini-circuits ZHL-32A-S
Biase-T	Mini-circuits ZFBT-4R2GW
LED	Luxeon LXML-PWC2
Quadrant Photodiode	OSI SPOT-9DMI
Transimpedance Amplifier	Femto DHPCA-100
Digitizer	GaGe CSE8389
Iron Aperture Plate	Thickness: 0.05 mm, Black Painted
Aperture Size	Radius: $l = 5$ mm
Aperture Height	$ h_a = 2.9$ mm

allows us to operate in the linear range of the LED. This signal is coupled into the the LED (LXML-PWC2) using a bias-T (ZFBT-4R2GW) that adds a 0.45 A DC current. This LED is mounted on a 2D motorized translation stage. For the receiver, we use a circular QPD (SPOT-9DMI) with radius $r_p = 5$ mm. This QPD is placed in a 3D-printed black box, and a black iron plate with thickness 0.05 mm and containing a laser drilled aperture of radius $l = 5$ mm is mounted at a height $h_a = 2.9$ mm above the QPD. The output of each quadrant of QPD is amplified by a TIA (DHPCA-100), and fed to a digitizer (CSE8389). The resulting outputs are sent to a PC where we perform power spectral analysis in order to extract the RSS values. The experiment specification is summarized in Tab. 6.1. The experiment consists of two phases. In the first phase, the misalignment is estimated using the proposed calibration algorithm, and in the second phase the SPO estimation is performed given the already estimated misalignment. With this setup, in the first phase of the experiment, we estimate the misalignment using the calibration procedure, and in the second phase, we determine the PO of the receiver, given the misalignment parameters estimated in the first phase.

In our system model, we used an idealized model for the RSS values for the different quadrants of the QPD. In a real QPD, however, there are some physical effects causing distortions. A first effect is the cross-talk between two segments [81], which is the phenomenon where excitement of one segment will result in a coupled response in another segment. A second effect is the spatial non-uniformity of the responsivity [82], causing the region closer to the boundary to have lower responsivity. These effects introduce deviations in the RSS vector, and consequently in μ (6.14). Therefore, in practice, the distortion induced by these effects should be modeled, estimated, and then compensated. As modeling and estimating these distortions separately would require sophisticated equipment, often only the joint effect of such distortions is considered. This joint effect is represented by an additive term that is a non-linear function of the light spot's position [83]. This implies that the coefficients of the polynomial can be determined without knowing the exact PO of the

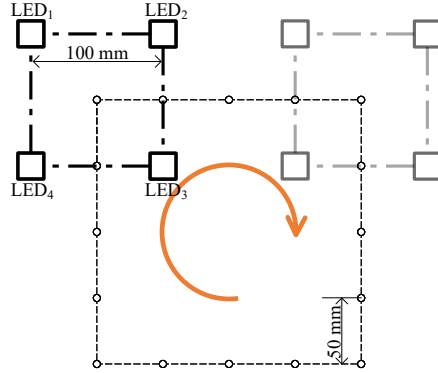


Figure 6.12: The square with four LEDs and the trajectory for the square.

receiver. A similar problem occurs for cameras, where the additive term models radial and tangential distortions of the lens [84] and the skewness of the axes of the image sensor [78]. In these works, the authors use a polynomial function to model the non-linear distortion. In this thesis, we will use a similar approach to model the distortions of the QPD, and heuristically determine the parameters of the polynomial model using the measured RSS values. This will allow us to subtract the additive distortion term from the measured RSS values. Our experiment will show that this distortion compensation will noticeably improve the performance of our estimators.

To determine the misalignment parameters in the calibration phase, we position the LED with the translation stage at $N_L = 25$ predefined positions belonging to a 5×5 square grid with spacing 100 mm between two LED positions. The receiver observes the LED at these $N_L = 25$ positions at $N_T = 12$ different randomly chosen POs with a tilt angle $\theta_\beta \approx \pi/6$ rad and a 'vertical' distance $z \approx 0.5$ m. Based on the resulting observations, we determine the misalignment parameters.

In the second phase, we estimate the receiver's PO. To this end, we mimic a scenario with 4 LEDs (the minimum required to estimate the PO), where our LED is moved by the translation stage to the corners of a square with side 100 mm. The receiver PO remains fixed for the 4 LED positions and separately measures the RSS values for the different positions, to estimate the PO of the receiver. We repeat this experiment for 16 different relative positions of the LEDs compared to the receiver, while keeping the PO of the receiver fixed. The 16 observation points belong to a trajectory that forms a square, where the distance between the observation points is 50 mm, as shown in Fig. 6.12. This square trajectory lies in the $x - y$ plane and is aligned with $x-$ and $y-$ axes. Each observation point corresponds to the center of the 4-LED positions needed for one PO estimate. The receiver is placed in front of the center of the square trajectory, at a 'vertical' distance z from the trajectory plane. The trajectory for the LEDs is repeated four times, for four different receiver's POs,

i.e. for $z \in \{\sim 0.65, \sim 1\}$ m and $\theta_\beta \in \{\sim 0, \sim \pi/6\}$ rad. Note that moving the center of the 4-LEDs along this trajectory is equivalent with keeping the positions of the 4 LEDs fixed and moving the receiver with fixed orientation. The "moving" receiver follows a new trajectory that is linked to the observation trajectory by $\mathbf{r} - \mathbf{r}_o$, where \mathbf{r}_o denotes the observation point. Due to our lack of suitable measurement equipment, the exact values of \mathbf{r} and \mathbf{R} are unknown so that we cannot obtain the ground truth values of the receiver trajectory and receiver orientation, which means we cannot compare performance in terms of absolute error. However, since the receiver trajectory is supposed to be parallel to the $x - y$ plane and square, we can compare the performance of the position estimation in terms of relative position error, i.e., ignoring the absolute value of the trajectory center. And, since the orientation of the receiver is fixed, i.e., the variance of the orientation should be zero, we can use the standard variance of the estimated orientations to compare the performance of the orientation estimation. Tab. 6.2 compares the performance of different algorithms for the four POs. It can be seen that the LS algorithm with calibrated intrinsic and distortion parameters (LS w/ ID) outperforms the LS algorithm with calibrated intrinsic parameters only (LS w/ I) and the LS algorithm without calibrated parameters nor distortion parameters (LS w/o ID), while the LS w/ ID algorithm achieves a similar performance as the baseline method with calibrated intrinsic and distortion parameters (BAS w/ ID) does. Fig. 6.13 shows the estimated trajectory in XY plane of different algorithms for z distance of 1.0 m and tilt angle of $\pi/6$ rad. The result confirms that the calibrated LS with intrinsic and distortion parameters gives the best performance in terms of shape of the estimated trajectory and variance of the estimated orientation. However, as the ground truth value is unknown, the cause of the estimation error is still under investigation.

6.4 Conclusion

In this chapter, we investigate the SPO estimation and calibration problem for the AQPDP receiver. To this end, the channel link is first modeled in terms of the receiver's PO and misalignment using the perspective projection model. Then, we show that the commonly applied strategy of differencing and normalization to the RSS, claimed by most works to improve the robustness against RSS variation, results in a complex PDF, which makes an effective and efficient estimation hard to achieve. Therefore, a simple closed-form approximate PDF is derived, based on which the calibration and the PO estimation algorithms using the least squares principle are proposed. The proposed calibration does not require any information about the PO of the receiver and is robust to the received power variation. In addition, the theoretical lower bound on calibration parameter estimates is also derived, which bounds the performance of the misalignment and can also be used as an indicator to determine the required SNR or the number of LEDs to obtain the desired accuracy. Both the synthesized data and the real experiment confirm the effectiveness of the proposed

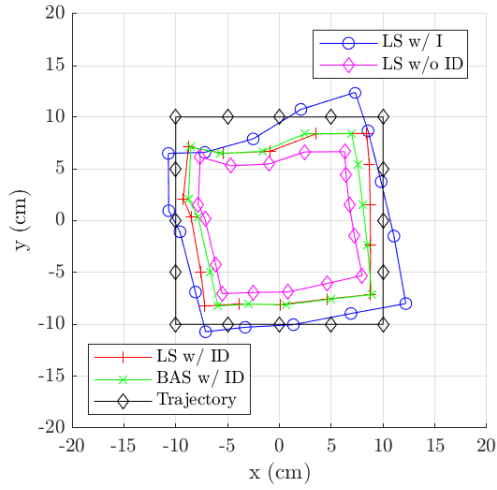


Figure 6.13: $x-y$ view of the estimated position for 1.0 m in z -direction and $\pi/6$ rad tilt angle.

algorithms. The research mentioned in this chapter was presented in [85].

7

Conclusions

7.1 Conclusions

High-efficiency and long-lasting white LEDs, which are gradually becoming the main source of lighting, can be modulated at frequencies up to several MHz. Consequently, white LEDs can be used for wireless communication and positioning, making it possible to achieve communication and positioning with low cost, low power consumption, and long lifetime. This provides an alternative solution to the demand for wireless transmission capacity and spectrum due to the rapid popularity of high throughput applications and the explosive growth of wireless connected devices. This thesis studies the position and orientation estimation problem for visible light systems with multiple LEDs and multiple PDs.

In order to achieve this goal, Chapter 2 introduces basic optical and electrical concepts of visible light channel. The system model as well as two receiver structures (i.e, the angular diversity receiver and the aperture-combined quadrant photodiode receiver) are modeled in this chapter. Chapter 3 reviews some techniques for estimation problems and optimization methods on the $SO(3)/SE(3)$. In Chapters 4-6, we investigate the simultaneous position and orientation estimation for the angular diversity receiver and the aperture-combined quadrant photodiode receiver.

The main contributions are summarized as follows:

- The structures of the angular diversity receiver and the aperture-combined receiver are modeled. The channel model for these receivers in multiple LEDs systems is derived.
- Based on the receiver model, the SPO estimation is first studied for the angular diversity receiver without an external orientation estimation device in Chapter 4. Two estimation algorithms are proposed and the theoretical lower bound is derived.
- Then the SPO estimation is further studied for the angular diversity receiver with an external orientation estimation device in Chapter 5. An

estimation algorithm is proposed and the associated theoretical lower bound is derived.

- For the aperture-combined quadrant photodiode receiver, we investigate both the calibration and SPO estimation problems. Efficient and effective algorithms for calibration and SPO estimation are, respectively, proposed and verified. The associated theoretical lower bound is also derived.

7.2 Future Research

In this thesis, we proposed several novel methods to solve the problems of position and orientation estimation. Although some important achievements have been made, there are still some challenges for future research.

- **Designing estimators that take into account the NLOS channel.** The current assumption in this thesis is that the NLOS channel is negligible, that is, the reflectivity of the environment is small and the receiver moves within a certain distance from the wall. It is of great interest to investigate other situations where NLOS channels need to be considered. One of the possible solutions is to establish a statistical model for the RSS in the presence of NLOS channel through simulation or experiment, and then update the estimators given in this thesis to incorporate this statistical information into the estimation as a prior information. Another possible solution is to design an optimal dynamic power allocation algorithm so that the system only focuses on LED-PD links with a strong LOS component.
- **Position and orientation estimation for hybrid RF/VLC system.** The hybrid RF/VLC system incorporates the better connectivity of RF techniques to enhance the VLC system to overcome its weaknesses, such as improving NLOS communication and achieving two-way communication. Therefore, the problem of position and orientation estimation for the hybrid RF/VLC system is a promising research topic. For example, when the light link does not exist or it is not good enough due to unsatisfactory position or orientation of the receiver, RF-based estimation can be a supplementary method. This system relies on an optimal position and orientation estimation scheme that combines RF and VLC techniques.
- **Position-orientation aided channel estimation for VLC.** The prior information about the position-orientation and trajectory of each user can be leveraged to estimate and track the channel. In the future, indoor communication applications will feature intelligent mobile IoT devices, so that timely position-orientation related information becomes instrumental in improving communication performance and facilitating efficient computation offloading.

Appendices



Evaluation of the NLOS Channel

Currently, simulation based methods, especially those based on ray tracing methods, are used by many works to investigate the channel taking into account the NLOS component. When a light ray hits a surface, the hit point will glow and behave like a light source, whose radiation pattern and power are determined by the surface's material and reflectivity. Many typical indoor materials, e.g. plaster walls, acoustic-tiled walls, carpets and unvarnished wood, have the first-order Lambertian pattern [86]. This mechanism forms the foundation for the ray-tracing algorithm. For the naive ray-tracing algorithm, a bunch of rays are first generated in accordance with the radiation pattern of the LED. Afterwards, the algorithm traces each ray to find the next reflection point, and then assigns new direction and power to the ray based on the hit point's radiation pattern and reflectivity. This tracing process is iterated until a maximum reflection number is reached or the ray's power is lower than a threshold. Since the ray-tracing simulates the behavior of light rays in reality, it can produce a high degree of realism when given a sufficient number of rays and reflections. However, the main drawback of this naive algorithm is its high variance when used to investigate the LED-PD channel, that is, since the amount of rays generated is limited and the active area of the PD is very small, most of the generated rays can not reach the PD, so that a small fraction of rays that successfully reach the PD will dramatically deviate the final result. Many improved practical algorithms have been proposed [87]. Because these improved algorithms achieve a similar accuracy, in this thesis, we adopt an algorithm called mixed ray-tracing-Monte Carlo algorithm [88] to evaluate the NLOS channel. The procedure for the mixed ray-tracing-Monte Carlo algorithm is given in Algorithm 1.2, where the difference from the naive ray tracing algorithm is the calculation of the contribution (and the corresponding travel time) from the hit point to the PD at each iteration. The contribution calculated in each iteration guarantees that the PD receives sufficient incident light to deal with the drawback of the naive ray-tracing algorithm.

Next, we compare the LOS and the NLOS channels using the mixed ray-

Algorithm 1.2 Algorithm for mixed ray-tracing-Monte Carlo algorithm

Initialization : Generate N rays complying with the LED's radiation pattern. Assign the i^{th} ray with a power of $P_i = P_t/N$.

LOOP Process

- 1: **for** $i = 1$ to N **do**
- 2: **for** $j = 1$ to maxiterations **do**
- 3: Trace the i^{th} ray to the next hit point.
- 4: Compute the ray's travel time
- 5: Update the ray with a new direction according to the hit point's radiation pattern
- 6: Update the ray with a new power according to the hit point's reflectivity ($P_i = \rho P_i$)
- 7: Compute the contribution and the travel time to the PD from the hit point with P_i
- 8: **if** $P_i \leq P_T$ **then**
- 9: break
- 10: **end if**
- 11: **end for**
- 12: **end for**

Table A.1: Simulation configuration for ray-tracing

Room		Source	Receiver
Size: [8, 6, 3] m		$\mathbf{n}_L = [0, 0, -1]$	$\mathbf{n}_P = [0, 0, 1]$
ρ	North: 0.3	South: 0.56	$P_t = 1$ W
	East: 0.3	West: 0.12	$\gamma = 1$
	Ceiling: 0.69	Floor: 0.09	$\theta_{FOV} = \frac{4\pi}{9}$ rad
Maximum Reflection: 12, Power Threshold: $P_T = 0$ W			

tracing-Monte Carlo algorithm. We consider an empty room with a single pair of LED - PD and evaluate the pair at three different positions, as illustrated in Fig. A.1. The room configuration is given in Tab. A.1, where the surface reflectivity refers to [86]. The curves shown in Fig. A.2 are the resulting impulse responses, where the LED generates a bunch of transient light rays at time 0 ns and the received power (or ray counts) response of the PD is plotted as a function of time. It can be seen that the results of all position settings have a lot in common. Specifically, the LOS and NLOS channels respectively result in two independent impulse response components, where the LOS component behaves like a weighted Dirac delta function with a time delay while the NLOS component behaves like a delayed exponential decay function in an overall sense. This observation agrees with the discussion in [89]. Further, let us take a closer look at the contributors of the NLOS component. It can be found that the contribution of the 1th reflection dominates the initial part of the NLOS component, and the higher order reflections in turn dominate. This is straightforward, because the higher order reflection takes more travel time.

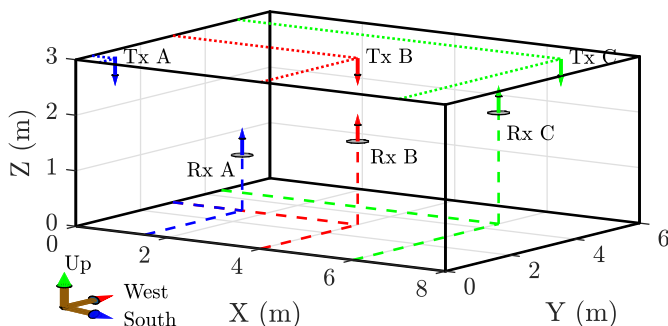
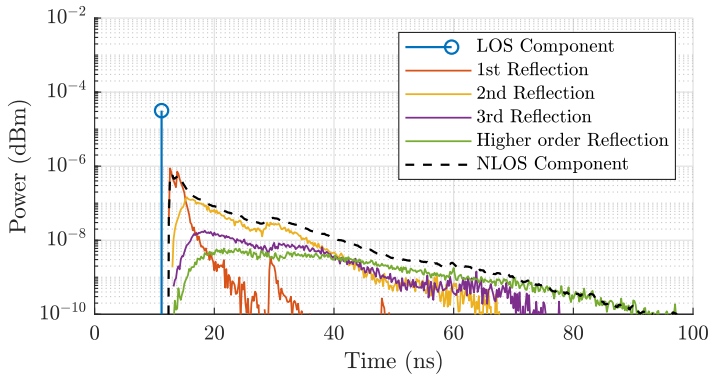


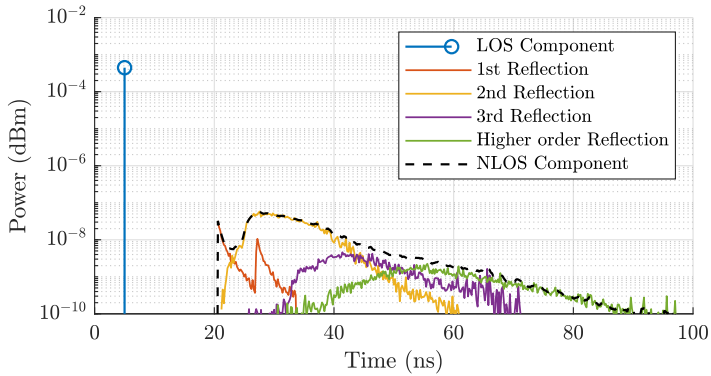
Figure A.1: Scenario for ray-tracing simulation.

However, the results also have lots of different aspects. First of all, since the time delay for the LOS component is determined by the LOS distance, the response of the setting A has the largest time delay in the LOS component due to its largest LOS distance. Contrarily, the time delay of the NLOS component is decided by the room size and the distances from PD to the room's walls. As a result, the response of the setting B has the largest time delay of the NLOS component. Second, it can be seen that the setting A has the largest peak magnitude of the NLOS component. This is because that the LED - PD pair of the setting A has the closest distance to the walls with the highest surface reflectivity, so that these walls contribute more reflected power to the PD.

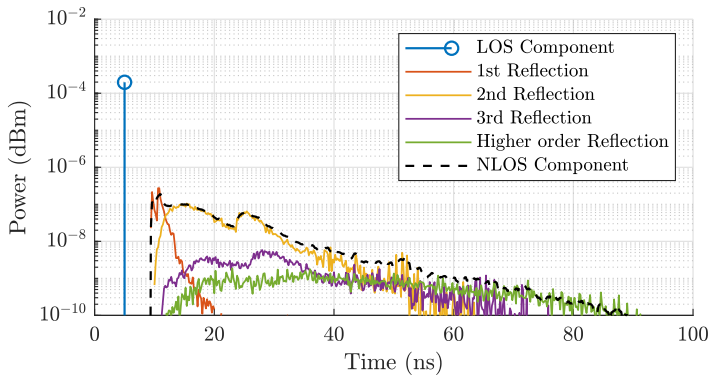
Next, we analyze the impact of the NLOS component from the frequency response. Since we only consider RSS-based estimation algorithms in this thesis, we will only evaluate the magnitude response. Fig. A.3 shows the magnitude responses obtained by performing FFT on the impulse responses. First, let us have a look at the NLOS component. It can be seen that the frequency response of the NLOS component is similar to that of a low pass filter in general because of its exponential decay shape in time domain. In addition, the magnitude of the NLOS frequency response varies with settings. Unsurprisingly, the NLOS component of setting A has the largest value due to its closest distance to the walls with high reflectivity, while that of setting B is the lowest since it has a large average distance to walls. Next, let us discuss the impact of NLOS channel on the LOS channel by comparing the respective LOS and composite channels for different settings. It is expected that when the NLOS component is small and the LOS components is large enough, the impact will be marginal. This anticipation is verified in Fig. A.3, where the frequency responses of LOS channel and corresponding composite channel almost coincide for setting B and C. Contrarily, it can be seen that the frequency response for setting A has a noticeable deviation at low frequency (≤ 40 MHz) than at high frequency. This



(a) Setting A



(b) Setting B



(c) Setting C

Figure A.2: Impulse response corresponding to different components.

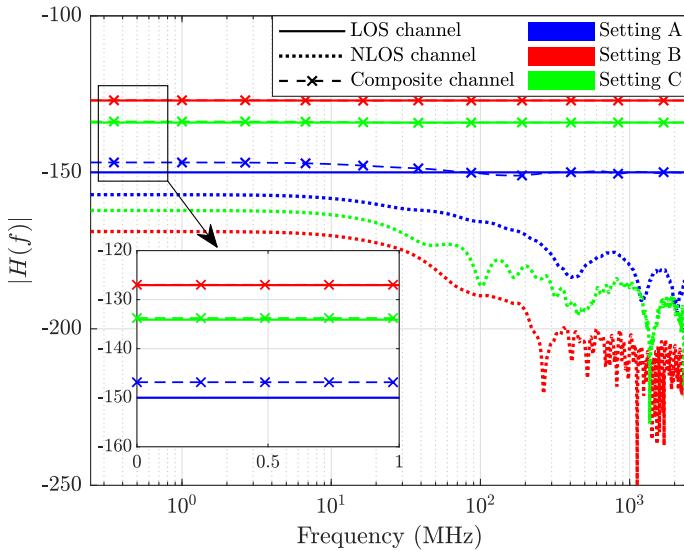


Figure A.3: Magnitude of the channel frequency response.

is due to the low-pass-filter-like behavior of the NLOS channel, so the impact on the LOS channel at high frequency is small.

According to the above analysis, the actual RSS deviates from the RSS inferred from the LOS channel formula due to the presence of the NLOS channel, but the deviation is highly dependent on the scenario. Different settings of the environment (such as the materials of walls and furniture, and the distribution of LEDs) and of the receiver will result in different deviations. When the reflectivity of the environment is low and the receiver moves in an area at a certain distance from the wall, the influence of the NLOS channel can be seen to be negligible.

B

Internal Reflection of the Aperture-Combined Receiver

The PD's active surface has a strong specular reflectance, and the house of the aperture-combined receiver usually cannot completely absorb the reflection, thereby incurring subsequent reflections. Thus, a striking light on the PD results in multiple internal reflections inside the receiver. However, as far as we know, there is still a lack of analysis of the internal reflection of the aperture-combined receiver. And, to what extent will the reflection affect the output signal is still unknown. Therefore, the internal reflection should be evaluated rather than simply ignored. Here, we use an optical engineering software – TracePro – to simulate the reflection inside the house and to evaluate the effect.

Table B.1: Simulation configuration for TracePro

Module	Size	Surface	Position
PD	Cylinder	Top: Photodiode	[0,0,0] mm
	Radius: 1 mm Hight: 0.5 mm	Rest: Black Paint	
Aperture	Circle	Black Paint	$[-\frac{\sqrt{2}}{2}, 1, \frac{\sqrt{2}}{2}]$ mm
	Radius: 1 mm		
Screen	Cuboid	Black Paint	[0, 1.005, 0] mm
	$5 \times 5 \times 0.01$ mm		
House	Inner surface: Cuboid	Black Paint	[0, 0.25, 0] mm
	$4 \times 4 \times 1.5$ mm		
LED	Cuboid	Emitter: Rebel ES	[-1.5, 1.5, 1.5] m
	$1 \times 1 \times 0.5$ mm	Rest: Black Paint	

The configuration for the simulation is given in Tab. B.1 and is illustrated in Fig. B.1. The result of ray-tracing is shown in Fig. B.2, which shows

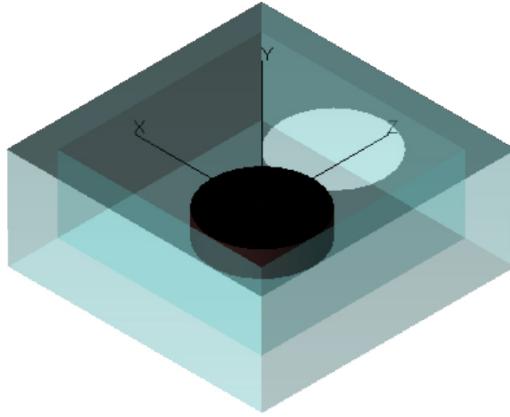


Figure B.1: Illustration of AQRD created in TracePro.

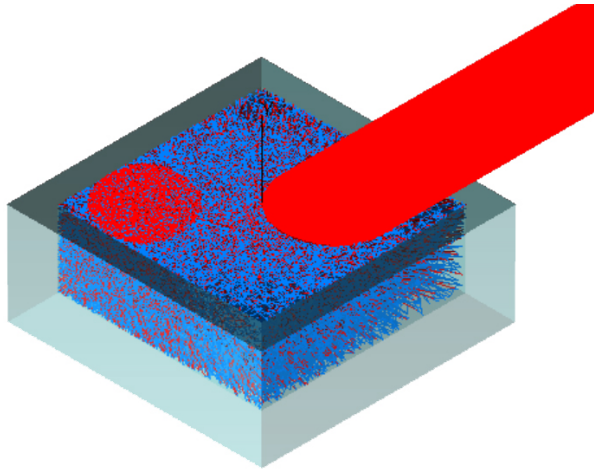


Figure B.2: Illustration of the simulated reflection inside the house.

only these rays that reach the PD's active area. It can be seen that the PD causes a specular reflection and creates a light spot on the inner surface of the screen, which consequently causes subsequent scattering reflections covering almost entire house. This observation indicates that the scattering inside the house will have an impact on the PD's output. To further evaluate the impact, let us have a look at the spatial distribution of irradiance and the temporal- and frequency- responses of irradiance, shown in Fig. B.3. Fig. B.3a shows the normalized heatmap of the irradiance distributed over the active area of

the PD, where the circled by the dotted line represents the active area, and the dashed line represents the projected light spot cast by the incident light, which is calculated from the relative position of the LED and the receiver. It can be seen that the only high-value region (the red region) of irradiance is the overlap area of dotted and dashed circles and that this region is evenly valued, which means that the incident light is a parallel light and the shape of light spot is only determined by that of the aperture. At the same time, the rest region of the active area has an evenly low value (the blue region), which means that the scattering has a uniform spatial effect on the active area but only with a limited intensity. Fig. B.3b shows the time dispersion of the normalized irradiance response. It can be seen that the direct hit of the incident light (denoted by LOS component) results in a short time impulse response, as we hope for. Contrarily, the response caused by the specular reflection of the PD (denoted by NLOS-PD) and the response caused by the reflection of the rest surfaces (denoted by NLOS-RS) disperse over time. However, the time dispersion is very small and the magnitudes of the NLOS components are also very small, implying that the impact is marginal. This anticipation is verified in the frequency response as shown in Fig. B.3c, where the composite and LOS responses coincide.

As a conclusion, the internal reflection of the aperture-combined receiver only has a marginal effect, and hence we can neglect it in the analysis.

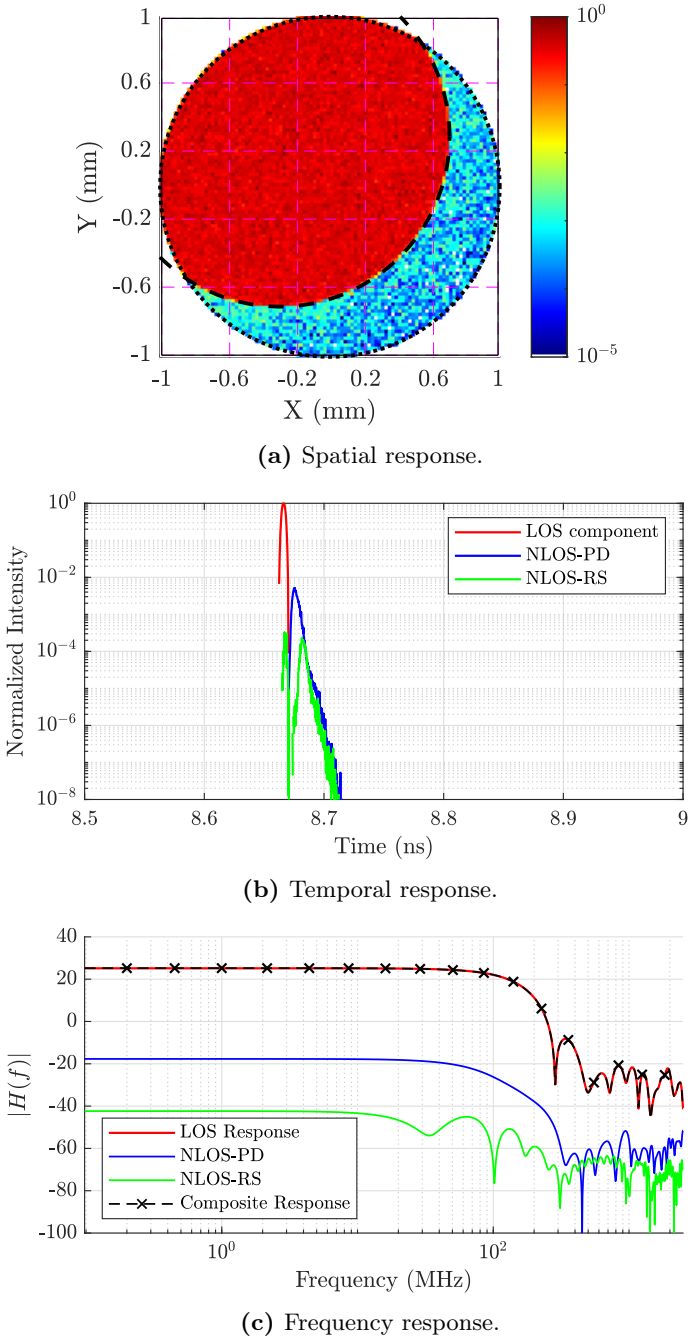


Figure B.3: Irradiance response of reflection inside the house.

C

Theoretical Lower Bound for the MML Estimator

In this appendix, we derive the theoretical lower bound for the MML estimator, which will be used in the numerical results in Section 5.4 for comparison. Taking into account that the MML algorithm considers the external orientation estimate $\tilde{\mathbf{R}}$ as the correct orientation, and ignores the orientation uncertainty, it considers a misspecified log-likelihood function to estimate the position. As a consequence, the RMSE for the resulting position estimate (for a given external orientation estimate $\tilde{\mathbf{R}}$) can be lower bounded by the misspecified CRB (MCRB), which is given by

$$\text{MCRB}(\mathbf{r}; \tilde{\mathbf{R}}) = (\mathbf{M}_1(\hat{\mathbf{r}}))^{-1} \mathbf{M}_2(\hat{\mathbf{r}}) (\mathbf{M}_1(\hat{\mathbf{r}}))^{-1} + \text{Bias}(\hat{\mathbf{r}}, \mathbf{r}), \quad (\text{C.1})$$

where the position estimate is defined as

$$\hat{\mathbf{r}} = \arg \min_{\mathbf{r}} \left(D \left(p(\mathbf{y}|\Theta) \parallel p_m(\mathbf{y}|\mathbf{r}; \tilde{\mathbf{R}}) \right) \right). \quad (\text{C.2})$$

In (C.2), $p(\mathbf{y}|\Theta)$ is the true PDF of \mathbf{y} where the conditioning is done on the correct position \mathbf{r} and orientation \mathbf{R} , $p_m(\mathbf{y}|\mathbf{r}; \tilde{\mathbf{R}})$ is the misspecified PDF of \mathbf{y} conditioned on the true position \mathbf{r} and parameterized by the (noisy) external orientation estimate $\tilde{\mathbf{R}}$, and $D \left(p(\mathbf{y}|\Theta) \parallel p_m(\mathbf{y}|\mathbf{r}; \tilde{\mathbf{R}}) \right)$ is the Kullback-Leibler divergence (KLD) between the true and the misspecified PDFs. The matrices \mathbf{M}_1 , \mathbf{M}_2 , and $\text{Bias}(\hat{\mathbf{r}}, \mathbf{r})$ are respectively given by

$$\mathbf{M}_1(\hat{\mathbf{r}}) = E_{\mathbf{y}|\Theta} \left\{ \Delta_{\mathbf{r}}^{\mathbf{r}} \ln p_m(\mathbf{y}|\hat{\mathbf{r}}; \tilde{\mathbf{R}}) \right\} \quad (\text{C.3})$$

$$\mathbf{M}_2(\hat{\mathbf{r}}) = E_{\mathbf{y}|\Theta} \left\{ \nabla_{\mathbf{r}} \ln p_m(\mathbf{y}|\hat{\mathbf{r}}; \tilde{\mathbf{R}}) \nabla_{\mathbf{r}}^{\text{T}} \ln p_m(\mathbf{y}|\hat{\mathbf{r}}; \tilde{\mathbf{R}}) \right\} \quad (\text{C.4})$$

$$\text{Bias}(\hat{\mathbf{r}}, \mathbf{r}) = (\mathbf{r} - \hat{\mathbf{r}}) (\mathbf{r} - \hat{\mathbf{r}})^{\text{T}}. \quad (\text{C.5})$$

As in general, $p(\mathbf{y}|\Theta) \neq p_m(\mathbf{y}|\mathbf{r}; \tilde{\mathbf{R}})$, the matrices \mathbf{M}_1 and \mathbf{M}_2 are in general not equal. The lower bound (C.1) still depends on the random variable $\tilde{\mathbf{R}}$. To

obtain the lower bound on the RMSE of the position estimate, we therefore need to average (C.1) over the distribution of $\tilde{\mathbf{R}}$:

$$E\{\mathbf{r}_e \mathbf{r}_e^T\} \succeq E_{\tilde{\mathbf{R}}|\mathbf{R}}\{\text{MCRB}(\mathbf{r}; \tilde{\mathbf{R}})\}. \quad (\text{C.6})$$

Note that the MML estimator does not estimate the orientation based on the optical signal. As a consequence, the mean squared error on the orientation is determined by the the statistics of the prior distribution, i.e. $E\{\mathbf{u}_e \mathbf{u}_e^T\} = \Sigma_e$.

Bibliography

- [1] N. U. Hassan, A. Naeem, M. A. Pasha, T. Jadoon, and C. Yuen, "Indoor positioning using visible LED lights: A survey," *ACM Comput. Surv.*, vol. 48, pp. 20:1–20:32, Nov. 2015.
- [2] F. Zafari, A. Gkelias, and K. K. Leung, "A survey of indoor localization systems and technologies," *IEEE Communications Surveys Tutorials*, vol. 21, no. 3, pp. 2568–2599, 2019.
- [3] G. Pons-Moll, A. Baak, J. Gall, L. Leal-Taixé, M. Müller, H. P. Seidel, and B. Rosenhahn, "Outdoor human motion capture using inverse kinematics and von Mises-Fisher sampling," in *2011 International Conference on Computer Vision*, pp. 1243–1250, Nov 2011.
- [4] B. Zhou and R. Wichman, "Visible light-based robust positioning under detector orientation uncertainty: A gabor convolutional network-based approach extracting stable texture features," in *2020 IEEE 30th International Workshop on Machine Learning for Signal Processing (MLSP)*, pp. 1–6, 2020.
- [5] K. Kalliola, "Bringing navigation indoors-the way we live next 2008," 2008.
- [6] R. Mautz, *Indoor positioning technologies*. PhD thesis, ETH Zurich, Zurich, 2012.
- [7] Y. Zhuang, Z. Syed, Y. Li, and N. El-Sheimy, "Evaluation of two WiFi positioning systems based on autonomous crowdsourcing of handheld devices for indoor navigation," *IEEE Transactions on Mobile Computing*, vol. 15, no. 8, pp. 1982–1995, 2016.
- [8] A. K. M. M. Hossain and W. Soh, "A comprehensive study of bluetooth signal parameters for localization," in *2007 IEEE 18th International Symposium on Personal, Indoor and Mobile Radio Communications*, pp. 1–5, 2007.
- [9] A. R. Jimenez Ruiz, F. Seco Granja, J. C. Prieto Honorato, and J. I. Guevara Rosas, "Accurate pedestrian indoor navigation by tightly coupling foot-mounted IMU and RFID measurements," *IEEE Transactions on Instrumentation and Measurement*, vol. 61, no. 1, pp. 178–189, 2012.

- [10] M. R. Mahfouz, C. Zhang, B. C. Merkl, M. J. Kuhn, and A. E. Fathy, "Investigation of high-accuracy indoor 3-D positioning using UWB technology," *IEEE Transactions on Microwave Theory and Techniques*, vol. 56, no. 6, pp. 1316–1330, 2008.
- [11] H. Kim, D. Kim, S. Yang, Y. Son, and S. Han, "An indoor visible light communication positioning system using a rf carrier allocation technique," *Journal of Lightwave Technology*, vol. 31, no. 1, pp. 134–144, 2013.
- [12] B. Xie, K. Chen, G. Tan, M. Lu, Y. Liu, J. Wu, and T. He, "LIPS: A light intensity-based positioning system for indoor environments," *ACM Trans. Sen. Netw.*, vol. 12, Sept. 2016.
- [13] W. Xu, J. Wang, H. Shen, H. Zhang, and X. You, "Indoor positioning for multiphotodiode device using visible-light communications," *IEEE Photonics Journal*, vol. 8, pp. 1–11, Feb 2016.
- [14] H. Steendam, "A 3-D positioning algorithm for AOA-based VLP with an aperture-based receiver," *IEEE Journal on Selected Areas in Communications*, vol. 36, pp. 23–33, Jan 2018.
- [15] H. Steendam, T. Q. Wang, and J. Armstrong, "Theoretical lower bound for indoor visible light positioning using received signal strength measurements and an aperture-based receiver," *Journal of Lightwave Technology*, vol. 35, pp. 309–319, Jan 2017.
- [16] Y. Zhuang, L. Hua, L. Qi, J. Yang, P. Cao, Y. Cao, Y. Wu, J. Thompson, and H. Haas, "A survey of positioning systems using visible LED lights," *IEEE Communications Surveys Tutorials*, vol. 20, pp. 1963–1988, thirdquarter 2018.
- [17] C. L. Bas, S. Sahuguede, A. Julien-Vergonjanne, A. Behlouli, P. Combeau, and L. Aveneau, "Impact of receiver orientation and position on visible light communication link performance," in *2015 4th International Workshop on Optical Wireless Communications (IWOW)*, pp. 1–5, Sept 2015.
- [18] N. Stevens and H. Steendam, "Influence of transmitter and receiver orientation on the channel gain for RSS ranging-based VLP," in *2018 11th International Symposium on Communication Systems, Networks Digital Signal Processing (CSNDSP)*, pp. 1–5, July 2018.
- [19] E. M. Jeong, S. H. Yang, H. S. Kim, and S. K. Han, "Tilted receiver angle error compensated indoor positioning system based on visible light communication," *Electronics Letters*, vol. 49, pp. 890–892, July 2013.
- [20] T. Yuan, Y. Xu, Y. Wang, P. Han, and J. Chen, "A tilt receiver correction method for visible light positioning using machine learning method," *IEEE Photonics Journal*, vol. 10, pp. 1–12, Dec 2018.

- [21] Q.-L. Li, J.-Y. Wang, T. Huang, and Y. Wang, "Three-dimensional indoor visible light positioning system with a single transmitter and a single tilted receiver," *Optical Engineering*, vol. 55, pp. 1–7, 2016.
- [22] M. F. Keskin, S. Gezici, and O. Arikan, "Direct and two-step positioning in visible light systems," *IEEE Transactions on Communications*, vol. 66, pp. 239–254, Jan 2018.
- [23] B. Zhou, V. Lau, Q. Chen, and Y. Cao, "Simultaneous positioning and orientating for visible light communications: Algorithm design and performance analysis," *IEEE Transactions on Vehicular Technology*, vol. 67, pp. 11790–11804, Dec 2018.
- [24] B. Zhou, A. Liu, and V. Lau, "Joint user location and orientation estimation for visible light communication systems with unknown power emission," *IEEE Transactions on Wireless Communications*, vol. 18, pp. 5181–5195, Nov 2019.
- [25] B. Zhou, A. Liu, and V. Lau, "Performance limits of visible light-based user position and orientation estimation using received signal strength under NLOS propagation," *IEEE Transactions on Wireless Communications*, vol. 18, pp. 5227–5241, Nov 2019.
- [26] S. Li, S. Shen, and H. Steendam, "A positioning algorithm for VLP in the presence of orientation uncertainty," *Signal Processing*, vol. 160, pp. 13 – 20, 2019.
- [27] A. Kitai, *Principles of Solar Cells, LEDs and Related Devices: The Role of the PN Junction*. John Wiley & Sons, 2018.
- [28] J. M. Kahn and J. R. Barry, "Wireless infrared communications," *Proceedings of the IEEE*, vol. 85, pp. 265–298, Feb 1997.
- [29] P. M. Pattison, M. Hansen, and J. Y. Tsao, "LED lighting efficacy: Status and directions," *Comptes Rendus Physique*, vol. 19, no. 3, pp. 134 – 145, 2018.
- [30] T. Komine and M. Nakagawa, "Fundamental analysis for visible-light communication system using LED lights," *IEEE Transactions on Consumer Electronics*, vol. 50, pp. 100–107, Feb 2004.
- [31] E. A. Lee and D. G. Messerschmitt, *Digital communication*. Springer Science & Business Media, 2012.
- [32] X. Yu, J. Wang, and H. Lu, "Single LED-based indoor positioning system using multiple photodetectors," *IEEE Photonics Journal*, vol. 10, pp. 1–8, Dec 2018.

- [33] L. Zeng, D. C. O'Brien, H. L. Minh, G. E. Faulkner, K. Lee, D. Jung, Y. Oh, and E. T. Won, "High data rate multiple input multiple output (MIMO) optical wireless communications using white LED lighting," *IEEE Journal on Selected Areas in Communications*, vol. 27, no. 9, pp. 1654–1662, 2009.
- [34] S. Cincotta, C. He, A. Neild, and J. Armstrong, "High angular resolution visible light positioning using a quadrant photodiode angular diversity aperture receiver (QADA)," *Optics Express*, vol. 26, pp. 9230–9242, Apr 2018.
- [35] Z. Chen, N. Serafimovski, and H. Haas, "Angle diversity for an indoor cellular visible light communication system," in *2014 IEEE 79th Vehicular Technology Conference (VTC Spring)*, pp. 1–5, May 2014.
- [36] A. Nuwanpriya, S. Ho, and C. S. Chen, "Indoor MIMO visible light communications: Novel angle diversity receivers for mobile users," *IEEE Journal on Selected Areas in Communications*, vol. 33, pp. 1780–1792, Sep. 2015.
- [37] C. Chen, W. Zhong, H. Yang, S. Zhang, and P. Du, "Reduction of SINR fluctuation in indoor multi-cell VLC systems using optimized angle diversity receiver," *Journal of Lightwave Technology*, vol. 36, pp. 3603–3610, Sep. 2018.
- [38] A. T. Hussein, M. T. Alresheedi, and J. M. H. Elmighani, "Fast and efficient adaptation techniques for visible light communication systems," *IEEE/OSA Journal of Optical Communications and Networking*, vol. 8, pp. 382–397, June 2016.
- [39] T. Q. Wang, C. He, and J. Armstrong, "Angular diversity for indoor MIMO optical wireless communications," in *2015 IEEE International Conference on Communications (ICC)*, pp. 5066–5071, 2015.
- [40] H. Steendam, T. Q. Wang, and J. Armstrong, "Cramer-Rao bound for indoor visible light positioning using an aperture-based angular-diversity receiver," in *2016 IEEE International Conference on Communications (ICC)*, pp. 1–6, 2016.
- [41] L. G. Kazovsky, "Theory of tracking accuracy of laser systems," *Optical Engineering*, vol. 22, pp. 22 – 22 – 9, 1983.
- [42] C.-Y. Lee, P.-C. Chou, C.-M. Chiang, and C.-F. Lin, "Sun tracking systems: A review," *Sensors*, vol. 9, no. 5, pp. 3875–3890, 2009.
- [43] S. Fortunati, F. Gini, M. S. Greco, and C. D. Richmond, "Performance bounds for parameter estimation under misspecified models: Fundamental findings and applications," *IEEE Signal Processing Magazine*, vol. 34, pp. 142–157, Nov 2017.

- [44] P.-A. Absil, R. Mahony, and R. Sepulchre, *Optimization algorithms on matrix manifolds*. Princeton University Press, 2009.
- [45] N. Boumal, “An introduction to optimization on smooth manifolds,” *Available online*, May, 2020.
- [46] T. D. Barfoot, *State Estimation for Robotics*. Cambridge University Press, 2017.
- [47] V. Joukov, J. Česić, K. Westermann, I. Marković, I. Petrović, and D. Kulić, “Estimation and observability analysis of human motion on Lie groups,” *IEEE Transactions on Cybernetics*, vol. 50, no. 3, pp. 1321–1332, 2020.
- [48] L. Li and M. Yang, “Joint localization based on split covariance intersection on the Lie group,” *IEEE Transactions on Robotics*, pp. 1–17, 2021.
- [49] H. A. Hashim and A. E. E. Eltoukhy, “Nonlinear filter for simultaneous localization and mapping on a matrix Lie group using imu and feature measurements,” *IEEE Transactions on Systems, Man, and Cybernetics: Systems*, pp. 1–12, 2021.
- [50] J. J. Craig, *Introduction to robotics: mechanics and control, 3/E*. Pearson Education India, 2009.
- [51] L. Falorsi, P. de Haan, T. R. Davidson, and P. Forré, “Reparameterizing distributions on Lie groups,” in *The 22nd International Conference on Artificial Intelligence and Statistics*, pp. 3244–3253, PMLR, 2019.
- [52] V. Peretroukhin, B. Wagstaff, M. Giamou, and J. Kelly, “Probabilistic regression of rotations using quaternion averaging and a deep multi-headed network,” *arXiv preprint arXiv:1904.03182*, 2019.
- [53] K. Hornik and B. Grün, “movMF: an R package for fitting mixtures of von Mises-Fisher distributions,” *Journal of Statistical Software*, vol. 58, no. 10, pp. 1–31, 2014.
- [54] T. D. Barfoot and P. T. Furgale, “Associating uncertainty with three-dimensional poses for use in estimation problems,” *IEEE Transactions on Robotics*, vol. 30, pp. 679–693, June 2014.
- [55] C. Forster, L. Carlone, F. Dellaert, and D. Scaramuzza, “IMU preintegration on manifold for efficient visual-inertial maximum-a-posteriori estimation,” Georgia Institute of Technology, 2015.
- [56] N. Boumal, “On intrinsic Cramér-rao bounds for riemannian submanifolds and quotient manifolds,” *IEEE transactions on signal processing*, vol. 61, no. 7, pp. 1809–1821, 2013.
- [57] V. Solo and G. S. Chirikjian, “On the Cramer-Rao bound in Riemannian manifolds with application to $SO(3)$,” in *2020 59th IEEE Conference on Decision and Control (CDC)*, pp. 4117–4122, IEEE, 2020.

- [58] S. Bonnabel and A. Barrau, “An intrinsic Cramér-Rao bound on $SO(3)$ for (dynamic) attitude filtering,” in *2015 54th IEEE Conference on Decision and Control (CDC)*, pp. 2158–2163, Dec 2015.
- [59] S. Bonnabel and A. Barrau, “An intrinsic Cramér-rao bound on Lie groups,” in *International Conference on Geometric Science of Information*, pp. 664–672, Springer, 2015.
- [60] C. J. Taylor and D. J. Kriegman, “Minimization on the Lie group $SO(3)$ and related manifolds,” tech. rep., Yale University, 1994.
- [61] J. Nocedal and S. Wright, *Numerical optimization*. Springer Science & Business Media, 2006.
- [62] R. H. Byrd, G. Liu, and J. Nocedal, “On the local behavior of an interior point method for nonlinear programming,” *Numerical analysis*, vol. 1997, pp. 37–56, 1997.
- [63] C. F. Van Loan and G. H. Golub, *Matrix computations*. Johns Hopkins University Press, 1983.
- [64] P. Sturm, “Algorithms for plane-based pose estimation,” in *Proceedings IEEE Conference on Computer Vision and Pattern Recognition. CVPR 2000 (Cat. No.PR00662)*, vol. 1, pp. 706–711 vol.1, June 2000.
- [65] R. Hartley and A. Zisserman, *Multiple view geometry in computer vision*. Cambridge university press, 2003.
- [66] S. M. Kay, *Fundamentals of Statistical Signal Processing: Estimation Theory*. Upper Saddle River, NJ, USA: Prentice-Hall, Inc., 1993.
- [67] Z. Ghassemlooy, W. Popoola, and S. Rajbhandari, *Optical wireless communications: system and channel modelling with Matlab®*. CRC press, 2019.
- [68] A. Şahin, Y. S. Eroğlu, I. Güvenç, N. Pala, and M. Yüksel, “Hybrid 3-D localization for visible light communication systems,” *Journal of Lightwave Technology*, vol. 33, pp. 4589–4599, Nov 2015.
- [69] J. Arvo, “Fast random rotation matrices,” in *Graphics Gems III (IBM Version)*, pp. 117–120, Elsevier, 1992.
- [70] S. Shen, S. Li, and H. Steendam, “Simultaneous position and orientation estimation for visible light systems with multiple LEDs and multiple PDs,” *IEEE Journal on Selected Areas in Communications*, vol. 38, no. 8, pp. 1866–1879, 2020.
- [71] H. Van Trees, K. Bell, and Z. Tian, *Detection Estimation and Modulation Theory, Part I: Detection, Estimation, and Filtering Theory*. Detection Estimation and Modulation Theory, Wiley, 2013.

- [72] P. R. Christian and G. Casella, “Monte Carlo statistical methods,” 1999.
- [73] S. Shen, S. Li, and H. Steendam, “Hybrid position and orientation estimation for visible light systems in the presence of prior information on the orientation,” (*article submitted for*) *IEEE Transactions on Wireless Communications*, 2020.
- [74] W. L. Wolfe and G. J. Zissis, *The infrared handbook*. Arlington: Office of Naval Research, Department of the Navy, 1978.
- [75] G. Marsaglia, “Ratios of normal variables,” *Journal of Statistical Software*, vol. 16, no. 4, pp. 1–10, 2006.
- [76] J. H. Curtiss, “On the distribution of the quotient of two chance variables,” *Annals of Mathematical Statistics*, vol. 12, pp. 409–421, 12 1941.
- [77] J. Hayya, D. Armstrong, and N. Gressis, “A note on the ratio of two normally distributed variables,” *Management Science*, vol. 21, no. 11, pp. 1338–1341, 1975.
- [78] Z. Zhang, “A flexible new technique for camera calibration,” *IEEE Transactions on Pattern Analysis and Machine Intelligence*, vol. 22, pp. 1330–1334, Nov 2000.
- [79] C. E. Rasmussen, “Gaussian processes in machine learning,” in *Summer school on machine learning*, pp. 63–71, Springer, 2003.
- [80] J.-Y. Bouguet, “Camera calibration toolbox for matlab (2008),” 2008.
- [81] S. Datta, A. Joshi, and J. Rue, “Crosstalk analysis in large-area low-capacitance InGaAs quad photodiodes,” in *Infrared Technology and Applications XXXIX* (B. F. Andresen, G. F. Fulop, C. M. Hanson, P. R. Norton, and P. Robert, eds.), vol. 8704, pp. 46 – 56, International Society for Optics and Photonics, SPIE, 2013.
- [82] G. F. Barranco, M. Tröbs, V. Müller, O. Gerberding, F. Seifert, and G. Heinzel, “Spatially resolved photodiode response for simulating precise interferometers,” *Appl. Opt.*, vol. 55, pp. 6688–6693, Aug 2016.
- [83] J. I. Ronda and A. Valdés, “Geometrical analysis of polynomial lens distortion models,” *Journal of Mathematical Imaging and Vision*, vol. 61, no. 3, pp. 252–268, 2019.
- [84] C. Ricolfe-Viala and A.-J. Sanchez-Salmeron, “Lens distortion models evaluation,” *Appl. Opt.*, vol. 49, pp. 5914–5928, Oct 2010.
- [85] S. Shen, J. M. Menéndez Sánchez, S. Li, and H. Steendam, “Simultaneous position and orientation estimation for visible light systems using aperture-combined quadrant photodiode,” (*article submitted for*) *IEEE Transactions on Wireless Communications*, 2021.

-
- [86] J. R. Barry, J. M. Kahn, W. J. Krause, E. A. Lee, and D. G. Messerschmitt, "Simulation of multipath impulse response for indoor wireless optical channels," *IEEE Journal on Selected Areas in Communications*, vol. 11, no. 3, pp. 367–379, 1993.
- [87] A. Al-Kinani, C. Wang, L. Zhou, and W. Zhang, "Optical wireless communication channel measurements and models," *IEEE Communications Surveys Tutorials*, vol. 20, no. 3, pp. 1939–1962, 2018.
- [88] F. J. López-Hernández, R. Pérez-Jiménez, and A. Santamaría, "Ray-tracing algorithms for fast calculation of the channel impulse response on diffuse IR wireless indoor channels," *Optical Engineering*, vol. 39, no. 10, pp. 2775 – 2780, 2000.
- [89] V. Jungnickel, V. Pohl, S. Nonnig, and C. von Helmolt, "A physical model of the wireless infrared communication channel," *IEEE Journal on Selected Areas in Communications*, vol. 20, no. 3, pp. 631–640, 2002.



Position and orientation estimation of objects using the light signal from the LED array.